EPFL

Thèse n° 9453

Tungsten oxide-based photoanodes: biomass valorization and the effects of oxygen vacancies

Présentée le 23 janvier 2023

Faculté des sciences de base
Laboratoire d'ingénierie moléculaire des nanomatériaux optoélectroniques
Programme doctoral en chimie et génie chimique

pour l'obtention du grade de Docteur ès Sciences

par

Nukorn PLAINPAN

Acceptée sur proposition du jury

Prof. J.-E. Moser, président du jury
Prof. K. Sivula, directeur de thèse
Prof. B. Bartlett, rapporteur
Prof. P. Broekmann, rapporteur
Prof. A. Boghossian, rapporteuse

École polytechnique fédérale de Lausanne

2023

The scientist does not study nature because it is useful to do so. He studies it because he takes pleasure in it, and he takes pleasure in it because it is beautiful. If nature were not beautiful it would not be worth knowing, and life would not be worth living

- Henri Poincaré

Acknowledgements

The research conducted during my PhD would not be possible without the funding. For this, I thank The Swiss Competence Center for Energy Research (SCCER) "Heat and Electricity Storage" (HaE), The National Centre of Competence "Sustainable chemical processes through catalyst design" (NCCR Catalysis), and the Development and Promotion of Science and Technology Talents Project (DPST) for the funding. The five years of my PhD have been undoubtedly a unique time of my life. It has been a very long roller coaster ride of mixed emotions and countless unique experiences. One thing is for sure, the time here is more pleasant and more memorable because of the people around me.

First, I would like to extend my gratitude to Prof. Bart Bartlett, Prof. Peter Brokemann, Prof. Ardemis Boghassian, Prof. Jaque-E Moser, and Prof. Kevin Sivula for serving as the Jury members for my PhD thesis defense and provide suggestions for my thesis. To Prof. Kevin Sivula, thank you for the opportunity to do my PhD in your lab. Countless hours of discussions with you have shaped me to be a better scientist. One thing I find very touching, during my candidacy you said: defend your work, but during my PhD defense, it was 'defend our work' that you said. It's a small thing, but this means a lot to me. There are times when I felt lost with my research, but you always help guide me in the correct direction. For this, I am truly grateful.

To the LIMNO members, you have made this lab a home away from home for me. There were times when I could have just worked from home at my place, but I chose to come to the lab just to be around you guys. A lot of memories have been made here. Charles, I am so delighted that our interests in the project aligned. I was so excited when you first proposed the biomass valorization ideas. It was great fun working with you. I am also grateful for all of the electrochemical and photoelectrochemical techniques that you showed me. You have provided me with enough foundation that I can take the biomass project and finally developed it into my PhD thesis. Florent, it has been a pleasure to have you as an office mate for three years. We didn't talk much in the beginning as you are quite a quiet person. But after we started to know each other, we just 'discussed' a lot. You truly made my first few years at LIMNO to be memorable. It was always fun to have a conversation with you, both trivial and scientific stuff. A credit has to be given to you for pointing out the idea on $\partial J/\partial E$ analysis, a concept later developed to become my second first-author publication. But perhaps the thing that I am most grateful to you is your introduction to Python for me. I have found my interest in programming because of this. This skill also later proved crucial for my PhD as it later involves a lot of fitting and loads of data analysis. Florian, thank you for taking care of me in my first year and showing me many electrochemical techniques. It helps me throughout my PhD. Junho, thank you for helping me with some measurements such as PL, contact angle measurement, and for a lot of fruitful scientific discussion. Lisa, although our project did not really have a lot in common, it has been great to have your company around. I did enjoy cycling with you and Mounir. I wish I have cycled with you more. Also, thank you for

introducing me to cross-country skiing, the only type of ski I enjoyed so far. Emeline, the lord mother of GC, the seeker of hydrogen, and the defender of the vales! It has been a pleasure to have you around from just chit-chat to the more serious scientific stuff. Your presence has truly made LIMNO a more organized place for sure! I also learned a lot about how the lamp calibration is done from helping you with essentially re-calibrating every lamp set up in the lab. Also, a lot of thanks for proofreading and commenting on chapters in this thesis. Marina, the lady boss! Again, this means you are such an organized and hard-working person. Thanks for the fun conversations in the lab over the years and also for documenting many fun moments on your Instagram story. And who can forget cycling with you. It was such a memorable time. I wish we could cycle together more! Bex, without you, the lab would have been a more dangerous and unorganized place. Thanks for giving zero tolerance to many safety-breaching activities in the lab over the years. Also, having a conversation with you has always been fun and who can forget your help in proofreading this thesis. You are also my go-to person when I have questions on the paper works and during the defense of my thesis. Thanks also for this. Simon, legend has it, it is hard to become friends with the Swiss, as they tend to cling onto their friends from their childhood. The outsider will have a difficult time trying to win their trust. Well, I find a hack for this, find a Swiss who has just moved from his hometown for the first time. Then it gets much easier from that. I will never forget countless times of our hikes (both in summer and snowshoeing in the winter) together. And of course, the tour du Mont Blanc. That was actually one of my bucket list. You have been such a great friend. But at the same time, I think I also learn a lot from you. My life here in Switzerland would have been much duller without you. Connor, casually talking to you in the comfort of the couch in your office has always been a joy. Whether it's serious scientific stuff or just casual talks, you have been such great company. Also, thanks for proofreading a chapter of my thesis. Colin (or more recently Cocolino!), my ex-office mate. Whenever I have questions related to life in Switzerland, you are my go-to person. Thanks for that. Also, thanks for making the office to be more lively for some time (before you chose the lake view over me. No harsh feeling, I get it, everybody loves the lake view!). Nicolas D. I wish you had joined the group earlier. The time in the lab just felt so enjoyed having you around. So does the time on the tennis court. Although I wish we could play more together. Thank you for suggesting and organizing countless activities this past year. This brings the members of the lab together. Don't get too stressed about your work. You are a talented individual. It will be just fine. YeonJu, if Anders didn't move to Sweden, we probably wouldn't have met. So, in the hindsight, I would consider it a good thing he decided to do so. Thanks for going cross-country skiing and snowshoeing with me. Chit-chatting is always fun. Ben, was once a student in my practical chemical engineering class and now my office mate. Thanks for organizing many activities for the lab and also for all the cakes! Wish you all the best for your PhD. Melanie, I also wish you have joined the lab sooner! Thanks for all those cycling trips. I wish we can do more of these cycling trips in the future. Annalisa, I enjoyed our collaboration, especially in the

last year of my PhD. I think I have learned a lot more about EIS and IMPS from our collaboration.

A special thanks have to be given to my dedicated Master students: Pamela and Nicolas F., I learned a lot from supervising them. Pamela, you are such a talented and hard-working individual. You have pushed the project forward and improved our understanding of the project. Nicolas F., you are the first Master student whom I can say I am the sole supervisor. It's also not easy for you to do the master project during the height of the pandemic! It was such a challenging time, but you finally finished it nicely. I learned a lot from having you as my student, both in terms of supervising and scientific findings. In fact, a small part of this thesis is the result of your hard work!

My Thai friends in Switzerland. Thailand is obviously very far from Switzerland. Luckily, I have a community of Thai students, here in Switzerland. As much as I love Switzerland, it is always nice to have a connection with the people where you are from. P'Noom, I know that we are actually only a few years apart in terms of age, but I called you my mom in Switzerland for a reason. Thanks for helping me settle down when I first arrived here. You are also a great listener. Listen without judging. PhD can be hard at times. Knowing that there are somebody who will listen to you is just precious. For this, I am really grateful. P'Wan, thanks for being such a great company whenever I visit Geneva and, for recommending me great restaurants around there. Going to Geneva is for sure a bit more lonely for sure without your presence. P'Gun, the queen of activity! Thank you for inviting me to many get-together activities. I will surely miss our countless hiking trips. P'P, you spent an exchange year in Geneva. I knew you since my undergrad time, but we didn't interact much back then. Our time here in Switzerland was different. I enjoyed countless trips with you, both in Switzerland and abroad. You are also a great listener. Talking to you always calms my nerves. I wish you could stay longer, and I was expecting for your return as a postdoc. Too bad that didn't materialize. I hope we cross paths again in the future. P'Top, thanks for taking me on my first hiking trip in Switzerland. Who would have forgotten the first hike that was supposed to be an easy and relatively short hike which turned into an epic 27 km. one! Our other hikes were also filled with many last-minute route changing and often turned into small adventures. Looking back, it was fun! Also, thank you for the many perspectives on doing a PhD and life in general. The conversation with you allows me to pause and think of the priority of things in life. Arm, when I first learned that I got a PhD position here in Switzerland, I immediately ask a friend of mine if he knows anyone at EPFL. He introduced you to me and you were officially my first friend in Lausanne! Thanks for helping me move in. Thanks for countless hiking days and trips abroad together. Most often our trips ended up with unexpected twists, but these make the experience more memorable. There have been so many occasions like this, that I think if I compile them together, I could have written a book about it! And now that my and your PhD comes to an end, we both also now got a job in Zürich. Now, I can't wait for our next adventure! Ice (Basel then Bellinzona and god knows where next!), Switzerland is a small country, but there are three persons whose nickname is Ice. How crazy is that! That's why we have to put the city where the person

lives after the name just to avoid confusion. Apart from the countless hiking and sledding trips we had together, you are probably the Thai friend whom I talked to the most during my PhD here. I recalled that we agreed that we can't stop being friends as we know too many secrets of each other! But really, I think of you as a friend that I can talk to about anything and perhaps you think the same of me. Over time I learn to appreciate the fortune of having someone whom you can always talk about anything. It becomes more precious, especially during hard times. You probably don't realize how happy I am when you said that if you can pick one Thai friend to come to your wedding, that person would be me. This really means a lot to me, and I hope that we will cherish our friendship for the years to come! NamKhang, thanks to your parents that did not name you Ice but rather, Namkhang (the Thai translation to Ice). There have been too many people whose nickname is Ice already. You are such a great company, especially in the last two years of my PhD. A big thanks for dragging me into the world of tennis. I wouldn't have discovered how much I enjoyed this sport. I still wish to play many more matches of tennis with you. So, hurry up and join me in Zürich!

My Thai friends abroad. These two individuals are friends from my undergraduate years. The two continued their study abroad as well. So, They know too well the highs and lows of a PhD life. Sup, we were already quite close during our undergrad time. You are very good at what you are doing and landed yourself a PhD position at MIT. Although the Atlantic Ocean and the six-hour time difference set us apart physically, modern communication technology still kept us connected. It has always been nice to talk about random stuff with you when I do the laundry. But I also cherish the serious stuff we talked about over the years. And who would have forgotten when we played Ragnarok (my teenager game) during the covid lockdown. I always wanted to just take a month off and play games with friends, but this is getting harder and harder as I grow older. So, thanks also for making my covid lockdown time entertaining and memorable. Aoey, when times are hard, you are probably one of the first person whom I talked to. In the end, I realized that the mental challenges the PhD pose upon us is probably more difficult to cope with than the academic struggle itself. So, just to have another person who not only understand but also struggles through pretty much the same experience as you is just priceless. Without you, this PhD would have been much much harder if not impossible. Now that my PhD has come to an end. I can't wait to celebrate the success of your PhD. Don't get stressed too much. Throw the imposter syndrome of yours out of the window! You are more talented and stronger than you think. Thanks for a space to sleep last Christmas in Hamburg. But more importantly, thanks for welcoming me in the darkest time of my PhD.

Last but not least (probably the most actually), my family. It's probably quite a cliche just to say thank you for the unconditional love they have given to me. But this is really what I truly felt my family has given to me. Thanks to my parents who always support me, both mentally and financially. But more importantly, thank you for always believing in me and being proud of me.

Although I don't say it often, but this really means the world to me. To my sister, thanks for being a person whom I can talk to and mediate many things between me and our parents, especially when I am away. To my maternal grandmother, my first chemistry teacher. Thank you for your support and understanding over the years. Lastly, to my maternal grandfather. I recalled you always said that you wish your grandchildren to have a PhD when I was young. I hope you can still remember that. Although the decision to do the PhD has been solely based on my love for science, I hope that my success in obtaining a PhD makes you proud.

Abstract

Tungsten oxide-based materials have unique and intriguing properties as photoanode materials for solar energy conversion. The first part of the thesis focuses on the use of WO_3 photoanodes for the oxidation of 5-(hydroxymethyl)furfural (HMF). Chapter one lays down the general introduction to HMF oxidation and the unique properties of WO_3 photoanodes. The direct oxidation (without any catalyst or a redox mediator) of HMF on WO_3 photoanode is presented in chapter two. WO_3 indeed shows activity toward the oxidation of HMF, but the product yield is very subtle. A kinetic model is developed and applied to the system to gain insight into the selectivity of HMF oxidation on the surface of WO_3. Faster kinetics of the competing reactions have been found to be the main culprit for the low yield. In chapter three, the development of an analysis technique to predict the selectivity between the competing reactions in the photoelectrochemical cells as the function of applied potential is discussed. The analysis is based on derivative voltammetry and can predict the selectivity using only the information from the linear sweep voltammogram. For the oxidation of HMF on WO_3, the analysis predicts the selectivity between the HMF oxidation and the competing water oxidation reaction, but the yield for the product yield remains unchanged regardless of the applied potential. To address this challenge, electrocatalysts are introduced to the surface of WO_3. The effects of electrocatalysts are laid down in chapter four. Finally, in chapter five, the work is expanded to $CuWO_4$. This ternary metal oxide retains many properties of WO_3 but with a smaller band gap, allowing this material to harvest a larger proportion of the solar radiation. The investigation is be based on the effects of oxygen vacancy (OV), a common dopant for metal oxides. Many studies have shown that a small number of this dopant help improve the photocurrent while the excess poses detrimental effects. Nevertheless, the effort to understand the effect of OV on the photocurrent has been unequally given to the benefits side. The reason for the adverse effect posts by the excess OV is rarely discussed. In this chapter, the effect of the number of OVs on the parameters that affect the photocurrent in $CuWO_4$ are discussed. To conclude this thesis presents the case for the use of tungsten oxide-based materials for solar energy conversion and gives a future outlook.

Keywords

photoanode, photoelectrochemistry, metal-oxide semiconductors, solar energy conversion, HMF oxidation, tungsten trioxide, biomass valorization, alternative oxidation, copper tungstate, oxygen vacancy

Résumé

Les matériaux à base d'oxyde de tungstène (WO_3) ont des propriétés uniques et intrigantes en tant que photoanodes pour la conversion de l'énergie solaire. La première partie de la thèse se concentre sur l'utilisation de photoanodes de WO_3 pour l'oxydation du 5-(hydroxyméthyl)furfural (HMF). Le premier chapitre présente une introduction générale sur l'oxydation du HMF et les propriétés des photoanodes de WO_3. L'oxydation directe (sans catalyseur ni médiateur redox) du HMF sur une photoanode de WO_3 est présentée dans le chapitre deux. Le WO_3 montre en effet une activité vers l'oxydation du HMF, mais le rendement du produit est bas. Un modèle cinétique a été développé et appliqué au système afin de mieux comprendre la sélectivité de l'oxydation du HMF sur la surface du WO_3. La cinétique plus rapide des réactions concurrentes s'est avérée être le principal responsable du faible rendement. Dans le chapitre trois, une technique d'analyse pour prédire la sélectivité entre les réactions concurrentes dans les cellules photoélectrochimiques en fonction du potentiel appliqué a été développée. L'analyse est basée sur la voltammétrie dérivée et peut prédire la sélectivité en utilisant uniquement les informations du voltammogramme de balayage linéaire. Pour l'oxydation du HMF sur WO_3, l'analyse prédit la sélectivité entre l'oxydation du HMF et la réaction concurrente d'oxydation de l'eau, mais le rendement du produit reste inchangé quel que soit le potentiel appliqué. Pour relever ce défi, des électrocatalyseurs sont introduits à la surface de WO_3. Les effets des électrocatalyseurs sont exposés dans le chapitre quatre. Enfin, dans le chapitre cinq, le travail est étendu à $CuWO_4$. Cet oxyde métallique ternaire conserve de nombreuses propriétés du WO_3 mais avec une bande interdite plus petite, ce qui permet à ce matériau de récolter une plus grande partie du rayonnement solaire. L'étude est basée sur les effets d'oxygènes vacants (OV), un dopant commun pour les oxydes métalliques. De nombreuses études ont montré qu'un petit nombre de ce dopant contribue à améliorer le photocourant tandis que l'excès a des effets néfastes. Néanmoins, la raison de l'effet négatif de l'excès de OV est rarement étudié. Dans ce chapitre, les effets du nombre des OV sur les paramètres qui affectent le photocourant dans $CuWO_4$ sont discutés. Pour conclure, cette thèse présente les arguments en faveur de l'utilisation de matériaux à base d'oxyde de tungstène pour la conversion de l'énergie solaire et donne des perspectives d'avenir.

Mots clés

Photoanode, photoélectrochimie, semi-conducteurs métal-oxyde, conversion de l'énergie solaire, oxydation du HMF, trioxyde de tungstène, valorisation de la biomasse, oxydation alternative, tungstate de cuivre, oxygènes vacants.

Contents

Acknowledgements **ii**

Abstract **vii**

Résumé **viii**

1 General Introduction **1**
1.1 Climates change and solar energy . . . 1
1.1.1 Achieving net-zero . . . 1
1.1.2 Hydrogen as an energy vector . . . 3
1.1.3 Water splitting reaction . . . 4
1.2 Photoelectrochemical water splitting . . . 5
1.2.1 Photoelectrochemical water splitting on semiconductors . . . 5
1.2.2 PEC cells configuration . . . 6
1.2.3 WO_3 and $CuWO_4$ as photoanode materials . . . 8
1.3 HMF oxidation . . . 9
1.3.1 Alternative reactions to the OER . . . 9
1.3.2 Performing HMF oxidation . . . 12
1.3.3 HMF oxidation to FDCA on PECs . . . 15
1.4 Objectives . . . 17

2 Photoelectrolysis of HMF on WO_3 Photoanode **27**
2.1 Introduction . . . 27
2.2 Results and discussions . . . 28
2.3 Conclusions . . . 32

3 Probing Reaction Selectivity Using Derivative Voltammetry **35**
3.1 Introduction . . . 35
3.2 Results and discussion . . . 36
3.3 Conclusions . . . 42

4 Strategies to Improve FDCA Yield **45**
4.1 Introduction . . . 45
4.2 Results and discussion . . . 45
4.2.1 MnO_x . . . 45
4.2.2 TEMPO . . . 47
4.2.3 NHPI . . . 57
4.3 Conclusions . . . 64

5 Effects of Oxygen Vacancies on the Physical and Photoelectrochemical Properties of Copper Tungstate Photoanodes **69**
5.1 Introduction . . . 69
5.2 Results and discussion . . . 73
5.3 Conclusions . . . 84

6 Conclusions and Outlook **88**
6.1 Biomass valorization using WO_3 photoanode . . . 88
6.2 Effects of oxygen vacancies to the photoelectrochemical properties of copper tungstate photoanode . . . 89

A Supporting Information to Chapter 2 **91**
A.1 Experimental details . . . 91
A.1.1 Synthesis of WO_3 electrodes on FTO coated glass . . . 91
A.1.2 Synthesis of $BiVO_4$ electrodes on FTO glass . . . 92
A.1.3 Synthesis of Fe_2O_3 . . . 92
A.1.4 Preparation of Electrolyte solutions . . . 93
A.1.5 Standard Electrochemical Measurements . . . 93
A.1.6 Extended-duration photo-oxidation experiments . . . 93
A.1.7 Oxidation products quantification . . . 93
A.1.8 Microscopy, XRD and Raman Spectroscopy . . . 94
A.1.9 Materials . . . 94
A.2 Characterization of WO_3 . . . 95
A.3 Chemical kinetics model and rate constant fit . . . 96
A.4 Supplementary figures and tables . . . 99

B Supporting Information to Chapter 3 **105**
B.1 Experimental details . . . 105
B.2 Mathematical foundation of the fit $\partial J/\partial E$ . . . 105
B.3 Supplementary Figures and Tables . . . 109
B.3.1 Fitted parameters . . . 109
B.3.2 Fitting $\partial J/\partial E$ of HMF/NaP_i with only one fitting curve . . . 109
B.3.3 EIS fitting . . . 110
B.3.4 The fitted $\partial J/\partial E$ and the DOS(E) as probed from EIS . . . 114

C Supporting Information to Chapter 4 **116**
C.1 Calculation for HMF consumption from photoelectrolysis of HMF using TemBen/Nafion® modified electrode . . . 117
C.2 Experimental details . . . 117
C.2.1 Electrode fabrication . . . 117
C.2.2 Standard electrochemical measurements . . . 119
C.2.3 Standard photoelectrolysis and electrolysis . . . 119
C.3 Supplementary figures and tables . . . 120
C.3.1 Cyclic voltammograms of the stability test of TEMPO/Nafion® with various fabrication methods . . . 120
C.3.2 Cyclic voltammograms of various TEMPO/Nafion® modified electrodes right after the stability test and with the fresh electrolyte . . . 124
C.3.3 Cyclic voltammograms of the stability test of TemBen/Nafion® modified electrode . . . 129

D Supporting Information to Chapter 5 **133**
D.1 Experimental details . . . 134
D.1.1 $CuWO_4$ electrode fabrication (condition A) . . . 134
D.1.2 Modifying number of oxygen vacancies in $CuWO_4$ electrode . . . 134
D.1.3 Electrochemical measurements . . . 135
D.1.4 Microscopy, XRD, Raman Spectroscopy, UV-Vis spectroscopy and XPS . . . 136
D.1.5 Materials . . . 136
D.2 Supplementary figures and tables . . . 137

List of Tables

1.1 Various heterogeneous electrocatalysts for HMF oxidation. a: BDC= terephthalic acid, MOF=metal–organic frameworks. b: Tp=triformylphloroglucinol, Bpy=5,5-diamino-2,2-bipyridine, COF=covalent organic frameworks, The pH of the electrolyte is 13. c: LDH=layered double hydroxide. 13

2.1 Pseudo-first order rate constants for oxidation by WO_3 photoanode at 0.68 V vs. RHE (pH 4, 3 Sun illumination), as extracted from model fitting (see reactions Figure 2.2). Standard error from fitting the averaged experimental data in parentheses. . 30

3.1 Predicted and the experimental-determined selectivity for HMF oxidation 41

4.1 Concentration of HMF, DFF, HMFCA, FFCA and FDCA before and after electrolysis of HMF solution using TemBen/Nafion®/FTO electrode as a working electrode. . 56

4.2 Concentration of HMF, DFF, HMFCA, FFCA, FDCA and the peak area of the rt-33 and the rt-77 peaks immediately after mixing the electrolyte from the electrolysis of NHPI using FTO as a working electrode with HMF solution and after 2 hours of stirring in the dark 64

5.1 Percentage between Cu(I)/Cu(0) to the total copper of the electrode in condition A, B, C and D as determined from XPS. 75

A.1 Concentration of HMF, DFF, FFCA, HMFCA, and FDCA over time of the control experiment (Figure A.4) 100

B.1 Fitted parameters from the fit $\partial J/\partial E$ of NaP_i and HMF/NaP_i solution 108

D.1 Conditions for the secondary annealing for producing the condition B, C, and D $CuWO_4$ electrodes. 135

List of Figures

1.1 A) Global primary energy consumption by source. Adapted from Our World in Data: Energy[7] B) Global CO_2 emission from fossil fuel and the median global temperature compared to the pre-industrial era. Adapted from Our World in Data: CO_2 and greenhouse gas emissions.[8] 2
1.2 Scheme for the photoelectrochemical cells A) photoanode / counter counter electrode (CE) with external bias B) photocathode / counter electrode (CE) with external bias C) bias-free, dual photoelectrode configuration. Adapted from ref.[20] 8
1.3 A) Component in lignocellulose biomass. B) HMF synthesis from hydrolysis of cellulose and subsequently followed by dehydration. Figure A is adapted from ref.[52] with the permission of ©2013 Royal Society of Chemistry Publishing 10
1.4 HMF oxidation to FDCA scheme 11
1.5 Structure of A) Polyethylene furanoate (PEF) and B) polyethylene terephthalate (PET) 11
1.6 Photographs of the anodic compartment after the electrolysis of the solution containing 20 mM HMF using MnO_x as an anode at the elevated temperature and after being cooled to room temperature. The produced FDCA precipitates out after the solution is cooled down to room temperature. Adapted from ref.[75] 15
1.7 Schematic of TEMPO-mediated HMF oxidation on a) photoanode and b) metal anode. Here CB, VB and E_F are conduction band, valence band and Fermi energy respectively. Adapted from ref.[89] with the permission of ©2015 Springer Nature . 16

2.1 Linear sweep voltammogram of (A) $BiVO_4$ photoanode in pH 9.2 NaB_i buffer (+5 mM HMF), (B) α-Fe_2O_3 photoelectrode in pH 14 NaOH electrolyte (+5 mM HMF), and (C) WO_3 photoanode in pH 4 NaP_i buffer (+5 mM HMF). The solid lines and dotted lines are LSVs under simulated 1 Sun illumination, and in the dark, respectively. The light illumination was from the back (glass) side. 29
2.2 Continuous photo-oxidation of HMF with WO_3 is shown by the evolution over time of: (A) the concentration of HMF and the photocurrent; (B) the concentration of DFF, HMFCA, FFCA and FDCA; the dashed lines are the result of the chemical kinetics fitting. Data is averaged over three independent runs and the error bars represent the standard deviation. (C) Reactions pathways for the formation of FDCA from HMF and by-product reactions leading to oxidized products B and B*. 30

3.1 LSV of WO_3 in NaP_i and HMF/NaP_i solution with and without illumination. . . 36
3.2 The $\partial J/\partial E$ analysis of WO_3 in (A) NaP_i electrolyte and (B) HMF/NaP_i solution. 38
3.3 Experimental and simulated photocurrent in (A) NaP_i electrolyte and in (B) HMF/NaP_i solution. (C) The concentration of HMF as a function of passed charge at 0.65 V, 0.85 V and 1.20 V vs. RHE with the fitted selectivity for HMF oxidation. (D) Predicted and the experimental-determined selectivity for HMF oxidation at different applied potential 40
3.4 DOS(E) as probed by EIS analysis of WO_3 in NaP_i electrolyte and HMF/NaP_i solution 42

4.1 Chopped-light linear sweep voltammogram of the MnO_x/WO_3 electrode with different amount of passed charge for photoelectrodepositted MnO_x.The voltammogram was recorded in 5 mM HMF solution under 1 sun illumination. 46
4.2 The evolution of of A) HMF and B) the intermediates (HMFCA, DFF and FFCA) and the product (FDCA) as a function of reaction time from the photoelectrolysis of HMF using the MnO_x/WO_3 as a working electrode. The photoelectrolysis was performed at 1 sun illumination and at the constant applied potential of 1.50 V vs. RHE. The supporting electrolyte was 0.1 M H_2SO_4 at pH 1. 47
4.3 Photographs of TEMPO/Nafion® modified electrodes fabricated by drop casting, spray coating, doctor blading and spin coating using the precursor solution concentration of 25 and 500 mg/mL. The modified electrode fabricated from spin coating method with the precursor concentration of 25 and 500 mg/mL have similar appearance. Only the film fabricated with the precursor concentration of 25 mg/ml is shown here. 49
4.4 Electron transfer reaction of TEMPO[26] 49
4.5 i_{pa}-CN plot of the TEMPO/Nafion® modified electrode prepared with various fabrication techniques and precursor concentrations. 51
4.6 i_{pa}-CN plot of the extended stability test of the drop casting-500 electrode 52
4.7 Structure of 4-Hydroxy-TEMPO benzoate (TemBen) 53
4.8 i_{pa}-CN plot from A) stability test of TemBen/Nafion® modified electrodes of various fabrication conditions and B) the extended stability test of the 500 rpm electrode. 54
4.9 UV-Vis absorption spectra of the solution after stability test of various TemBen/Nafion® modified electrodes and the UV-Vis absorption spectrum of the saturated TemBen solution. 55
4.10 A) Chronoameperogram with passed charge and B) linear sweep voltammograms before and after the electrolysis of HMF solution using the 500 rpm electrode as a working electrode. The electrolysis was performed at the applied potential of 1.5 V vs. RHE in NaB_i solution at pH 9 56
4.11 Electron transfer reaction of NHPI[26] 57
4.12 Cyclic voltammograms of the blank electrolyte (NaP_i) , 7.5 mM NHPI in NaP_i solution and 7.5 mM NHPI + 5 mM HMF in NaP_i solution. Graphite rode was used as a working electrode. 58
4.13 Cyclic voltammograms of WO_3 under illumination and in the dark in the blank solution (NaP_i solution) and 7.5 mM NHPI in NaP_i solution 59
4.14 Photocurrent and the passed charge as a function of reaction time of the photoelectrolysis of the solution containing 1.5 mM NHPI, 1 mM HMF and both 1.5 mM NHPI and 1 mM HMF over WO_3. The photoelectrolyses were performed under 1 sun illumination and at the applied potential of 1.43 V vs. RHE 60
4.15 Concentration of HMF, DFF, HMFCA, FFCA and FDCA as a function of a passed charge from the photoelectrolysis of the solution containing HMF (denoted as control) and both HMF and NHPI (denoted as with NHPI). 61
4.16 A) HPLC chromatogram of NHPI solution (1 mM) in NaP_i buffer. The inset shows the tailing between the rt-33 and rt-77 peaks. B) Peak area of the rt-33 and rt-77 as a function of reaction time from photoelectrolysis of NHPI over WO_3 electrode . . 61
4.17 HPLC chromatogram of NHPI solution before and after photoelectrolysis over WO_3 62
4.18 HPLC chromatogram of the HMF+NHPI and NHPI solution after the photoelectrolysis over WO_3 63

5.1 Band diagrams for $CuWO_4$ and WO_3. Adapted from ref.[8] with the permission of ©2011 Royal Society of Chemistry Publishing 70

5.2 A) Theoretical maximum photocurrent (J_{max} as a function of the band gap of a semiconductor. B) LSV showing J_{max} and J_{PEC}. Scheme of charge separation and recombination C) in the bulk and D) at the surface of a photoanode. Figure A) is adapted from ref.[13] with the permission of ©2019 Royal Society of Chemistry Publishing. Figures C) and D) are adapted from ref.[14] with the permission of ©2021 Springer Nature publishing 71
5.3 Photograph of $CuWO_4$ films for conditions A, B, C and D on FTO substrates ($\sim$ 1.25 $\times$ 2.5 cm) 73
5.4 XPS spectra of $CuWO_4$ films for conditions A, B, C and D. A) A Zoom in of Cu $2p_{3/2}$ region and B) A zoom in of W 4f region. 74
5.5 UV-Vis spectra of the $CuWO_4$ film condition A, B, C and D 75
5.6 Top-down SEM micrographs of $CuWO_4$ films of A) condition A, B) condition B, C) condition C and D) condition D. 76
5.7 A) Raman spectra and B) XRD spectra of the $CuWO_4$ films for conditions A, B, C and D. C) Comparison of the XRD spectrum of condition D film with various reference spectra. 77
5.8 A) Chopped-light illumination linear sweep voltammograms of $CuWO_4$ films condition A, B, C and D (in 0.1 M KP_i buffer pH 7). Average photocurrent density at B) 1.23 V vs. RHE and at D) 1.75 V vs. RHE of $CuWO_4$ films condition A, B, C and D. The average photocurrent was calculated from three samples per condition. 79
5.9 A) Photographs of $CuWO_4$ electrode conditions for A, B, C and D after undergoing LSV. B) A top-down SEM micrograph of the $CuWO_4$ film condition D after LSV. Raman spectra of the $CuWO_4$ film condition C) C and D) D before and after undergoing LSV. 80
5.10 Average IPCE at 1.23 and 1.75 V vs. RHE of $CuWO_4$ condition A) A, B) B, C) C and D) D. The value shown here is the average value from three samples per condition. The solid line represents the average value. The shaded area represents the standard deviation of the measurement. 82
5.11 A) Chopped-light linear sweep voltammograms of $CuWO_4$ condition A and B and linear sweep voltammogram (in the dark) of an FTO substrate in a sacrificial conditions (1.5 Na_2SO_3 pH 7). Average B) charge separation efficiency (η_{sep}) and C) charge injection efficiency (η_{inj}) of $CuWO_4$ condition A and B at 0.8, 0.9, 1.0 and 1.23 V vs. RHE. The average value comes from three samples. 84

A.1 SEM images of WO_3 on FTO in A) top view and B) cross-section view illustrating the film thickness of 1.875 μm 95
A.2 XRD spectrum of WO_3 film (black trace) with the reference spectrum (red line) . 96
A.3 Raman spectrum of WO_3 film 96
A.4 Concentration of HMF, DFF, FFCA, HMFCA, and FDCA over time. For this experiment a 5 mM solution of HMF in 0.1 M pH 4 NaP_i was irradiated with simulated 3 Suns. 99
A.5 SEM images of a WO_3 electrode (A) before, and (B) after a 16 hrs bulk electrolysis experiment. This time frame was selected since it was after the largest observed photocurrent decrease. The bulk electrolysis experiment was performed at 0.683 V vs. RHE under simulated 3 suns illumination in a pH 4 0.1 M NaP_i solution which contained 5 mM HMF. 101
A.6 Difference between the LSV with and without HMF under 3 suns in pH 4 NaP_i solution. The vertical line depicts the photocurrent density at the applied bias used in the bulk electrolysis experiments. 102
A.7 Chronoamperometry of HMF oxidation on WO_3 under simulated 3 suns in pH 4 NaP_i solution showing the impact of stirring the solution on the photocurrent. . . 102
A.8 LSVs of WO_3 electrodes under simulated 1 sun illumination in solutions containing 5 mM HMF, 5 mM DFF, 5 mM BHMF, and a blank control solution. All solutions were prepared using 0.1 M NaP_i buffered to pH 4. 103

A.9 LSVs of WO_3 electrodes under simulated 1 sun illumination in solutions containing 5 mM HMF, 5 mM FDCA, and a blank control solution. All solutions were prepared using 0.1 M NaP_i buffered to pH 4. 103

B.1 A) $\partial J/\partial E$ analysis and B) Simulated photocurrent of HMF/NaP_i solution with only 1 fitting curve 109
B.2 HMF consumption as the function of passed charge at 0.65 V and 1.20 V vs. RHE and at the initial HMF concentration of 5 mM and 100 mM. The dotted line represent the Faradaic efficiency of 10%, 25%, 50% and 100% as calculated from two-electron oxidation of HMF 110
B.3 Bode plot (left) and Nyquist plot (right) in NaP_i electrolyte. 110
B.4 Bode plot (left) and Nyquist plot (right) in HMF/NaP_i solution 111
B.5 The fitted value (C_B, C_{SS}, R_{CTSS} and R_{SS}) in NaP_i and HMF/NaP_i solution. The R_B value was kept constant at 0.79 $k\Omega.cm^{-2}$ for both solutions. 113
B.6 Overlaid graph of the experimental derivative voltammogram, the fit $\partial J/\partial E$ and the DOS(E) as found from EIS in A) NaP_i electrolyte and B) 5 mM HMF in NaP_i solution 114

C.1 Raman spectra of MnO_x, WO_3 and MnO_x/WO_3 films on FTO 118
C.2 Cyclic voltammograms of the drop casting-25 electrode 120
C.3 Cyclic voltammograms of the drop casting-500 electrode 121
C.4 Cyclic voltammograms of the spray coating-25 electrode 121
C.5 Cyclic voltammograms of the spray coating-500 electrode 122
C.6 Cyclic voltammograms of the doctor blading-25 electrode 122
C.7 Cyclic voltammograms of the doctor blading-500 electrode 123
C.8 Cyclic voltammograms of the spray coating electrode 123
C.9 Cyclic voltammograms of the cycling electrolyte and the fresh electrolyte of the drop casting -25 electrode 124
C.10 Cyclic voltammograms of the cycling electrolyte and the fresh electrolyte of the drop casting -500 electrode 124
C.11 Cyclic voltammograms of the cycling electrolyte and the fresh electrolyte of the spin coating -25 electrode 125
C.12 Cyclic voltammograms of the cycling electrolyte and the fresh electrolyte of the spin coating -500 electrode 125
C.13 Cyclic voltammograms of the cycling electrolyte and the fresh electrolyte of the doctor blading -25 electrode 126
C.14 Cyclic voltammograms of the cycling electrolyte and the fresh electrolyte of the doctor blading -500 electrode 126
C.15 Cyclic voltammograms of the cycling electrolyte and the fresh electrolyte of the spray coating electrode 127
C.16 Combined cyclic voltammograms of TEMPO/Nafion® modified electrodes in the fresh electrolyte after the stability tests 127
C.17 Cyclic voltammograms from the extended stability test of the drop casting-500 electrode 128
C.18 Cyclic voltammograms of the stability test of the 500 rpm electrode 129
C.19 Cyclic voltammograms of the stability test of the 1000 rpm electrode 130
C.20 Cyclic voltammograms of the stability test of the 2000 rpm electrode 130
C.21 Cyclic voltammograms of the stability test of the 3000 rpm electrode 131
C.22 Cyclic voltammograms of the extended stability test of the 500 rpm electrode . . . 131
C.23 Chromatogram before and after the electrolysis of NHPI using FTO as a working electrode 132

D.1 Tauc plot of the $CuWO_4$ films condition A, B, C and D 137
D.2 Cross section SEM micrograph of $CuWO_4$ film condition A. The film thickness is found to be approximately 400 nm. 137

D.3 Average photocurrent at A) 1.23 V vs. RHE and B) 1.75 V vs. RHE of the $CuWO_4$ film condition A and the $CuWO_4$ films which have been subjected to the secondary annealing under 13 % H_2/Ar flow at 300 °C for 5, 10 and 20 minutes (condition B). The average photocurrent was obtained by performing chopped-light illumination LSV. 138
D.4 Average IPCE of the $CuWO_4$ condition A, B, C and D from 300 - 800 nm at A) 1.23 V vs. RHE and B) 1.75 V vs. RHE. 138
D.5 Normalized average IPCE at 1.23 V vs. RHE and at 1.75 V vs. RHE of the $CuWO_4$ condition A) A, B) B, C) C and D). 139

Chapter 1

General Introduction

Parts of this chapter is adapted from following mini-review: Enabling direct photoelectrochemical H_2 production using alternative oxidation reactions on WO_3. This mini-review is under preparation.

1.1 Climates change and solar energy

1.1.1 Achieving net-zero

The industrial revolution has improved the productivity of many economic sectors dramatically. This increase in productivity has significantly improved the living standard of humankind. The growth in industrial activities commands a great demand for energy consumption. Global energy consumption has increased exponentially since the industrial revolution (Figure 1.1A). The main sources of energy are fossil fuels (coal, oil, and gas), due to the high energy density and ease of storage and transport. The burning of these fossil fuels has contributed to the increase in global CO_2 emissions, subsequently resulting in the increase in the average global temperature (Figure 1.1B). The rising global temperature has resulted in more extreme weather events such as heat waves, drought, and floods in recent years. The term climate change is used to describe these extreme weather events due to the rising in global temperature with devastating consequences.

In order to prevent a catastrophic outcome, many countries have pledged to achieve net zero emissions by 2050.[1] To realize this, the reliance on fossil fuels must come to an end, and renewable energy has to step up as the main energy source for the world. Despite the global annual energy consumption of around 6×10^{20} J.year^{-1} ,[2] the amount of renewable energy that can be used per year far exceeds this value. In fact, solar energy alone is more than enough to supply the

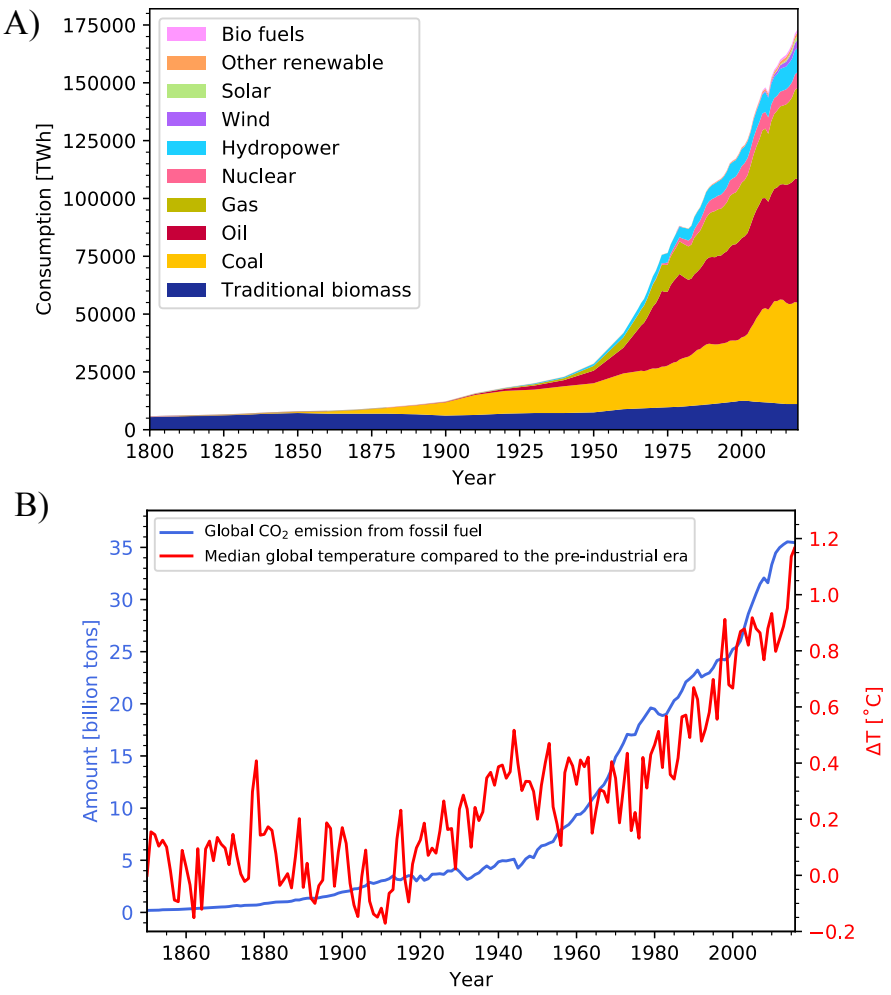

Figure 1.1: A) Global primary energy consumption by source. Adapted from Our World in Data: Energy [7] B) Global CO_2 emission from fossil fuel and the median global temperature compared to the pre-industrial era. Adapted from Our World in Data: CO_2 and greenhouse gas emissions. [8]

world's energy demand. At 1.25×10^{24} J.year^{-1} harvestable solar energy,[i] it would take only 0.48% of the total land mass of the earth for the 10% efficiency solar cell to produce enough energy to meet the global energy demand. Nevertheless, many renewable sources, such as wind and solar, are intermittent. The supplies of these energy sources fluctuate greatly with day and night cycles and seasons, leading to a time disparity in the energy supply and the energy demand on many occasions. Because of the intermittency, integrating electricity generated from wind and solar into the grid poses a challenge in many places around the globe. Electricity generation needs to match the demand at a particular time. Integrating wind and solar energy into the grid can increase the disparity gap between the demand and the supply of electricity, especially at night when solar farms cannot produce any electricity. [6]

[i]The calculation is based on the following assumptions: (1) The solar irradiance is AM 1.5 G, thus 1000 W.m^{-2}.[3] (2) The total land area of the earth is 1.49×10^{14} m^2.[4] (3) The earth average annual sunny hours is 2334 h.year^{-1}.[5]

1.1.2 Hydrogen as an energy vector

To solve the challenge of intermittency, energy storage is needed. Many strategies to store renewable energy have been developed such as batteries, pumped-storage hydroelectricity, flywheel energy storage, and supercapacitors.[9,10] Each method has advantages and disadvantages and suits different applications. Hydrogen has emerged as an interesting choice of energy storage. It has a very high energy density of 120 MJ/kg, 2.5 times higher than that of gasoline (47.5 MJ/kg).[11] In addition to this, gasoline is used in an internal combustion engine (ICE) which relies on a combustion and gas expansion to extract energy from fuel and translate it into mechanical work. Typical ICEs have an efficiency of around 20-30 %. Hydrogen, on the other hand, can be utilized by a fuel cell that first extracts energy stored in hydrogen into electrical energy. The electricity generated by the fuel cell is then used by an electric motor to perform mechanical works. Since an electric motor has higher efficiency than ICEs, the energy stored in hydrogen can be utilized more efficiently than the energy stored in gasoline. In addition to this, when hydrogen is used in a fuel cell, the exhaust is simply water. For the ICEs, the exhaust not only contains CO_2 from the combustion but also includes much harmful gas such as NO_x and SO_x. Soot can also be found in the exhaust if the combustion is incomplete. Hence, not only can the energy stored in hydrogen be utilized more efficiently, but the exhaust from its oxidation is much cleaner. Hydrogen can also be transported using the existing infrastructure for transporting fossil fuels, the pipeline network. So, the distribution of hydrogen is not an issue of concern.

However, Hydrogen also has certain disadvantages, preventing its widespread adoption. Despite its high energy density, hydrogen is a gas at room temperature and at 1 bar. Without any compression, its power density (energy per unit volume) is very low. Therefore, hydrogen is stored in a compressed form: either in a liquid form or in a compressed gas form. The compression of hydrogen requires additional energy and its storage in the compressed form requires vessels that can withstand high pressure. Numbers of hydrogen storage strategies have been demonstrated[12,13], but many of these methods are still in the research stage or are still too expensive to be economically viable. In addition to this, the technological maturity of fuel cell technology is still in its early stages in comparison to the ICEs. With many hurdles still needed to tackle to use hydrogen as an energy storage, the use of a battery as an energy storage has been more widely adopted for electric vehicles (EVs), at least, for personal cars. Nevertheless, the typical Li-ion battery used in Battery electric vehicles (BEVs) has a low energy density. Certain applications which demand high energy density, such as long-distance lorries and cargo ships cannot use a battery as a source of energy and still have to rely on fossil fuels. Airplanes are also a good example of this. Air travels have a bad

reputation of being one of the main contributors to the surge in CO_2 in the past years. Current passenger planes rely solely on fossil fuels to keep them in the sky. Replacing jet fuel with battery is not a viable option as the energy density of the current battery technology is simply not high enough. Battery-powered planes have been shown to be a possible invention, but the concept was only proven on small planes.[14] For an airliner, swapping jet fuel with a battery will make them too heavy to fly. However, replacing jet fuel with hydrogen is a viable option because of the superior energy density of hydrogen,. In addition to this, charging batteries take time. The time required to fully charge the battery in a typical BEV can take several hours. Direct current fast charging technology can help reduce the time required for full charging to less than an hour, but it is still far longer than the time required to fill up a hydrogen tank. All in all, despite some disadvantages, hydrogen remains an interesting option for energy storage.

1.1.3 Water splitting reaction

The most common way to produce hydrogen from renewable energy (electricity) is by water electrolysis (Equation 1.1). In this reaction, water is cleaved into its constituent elements, hydrogen and oxygen, using electricity. The water splitting reaction can be broken down into two half-reactions: the hydrogen evolution reaction (HER, Equation 1.2) and the oxygen evolution reaction (OER, Equation 1.3). The HER and OER take place at the cathode and the anode respectively. Thermodynamically, an applied potential of 1.23 V is required to drive the water splitting reaction. In practice, the energy required to drive the reaction at a reasonable rate is higher than this thermodynamic barrier. This additional energy required is called the overpotential and results from a kinetics barrier to perform the reaction. The higher the overpotential, the higher the energy required to drive the reaction. An overpotential is, therefore, non-desirable and needs to be minimized as much as possible. Many factors contribute to the overpotential such as mass transport limitation, poor electrolyte conductivity, and bubble formation. Slow reaction kinetic is one of the factors that affect the overpotential. For the HER and the OER, the latter has a higher overpotential due to the sluggish reaction kinetics of the four-electron transfer reaction associated with the OER.[15]

$$H_2O \longrightarrow H_2 + \frac{1}{2}O_2 \tag{1.1}$$

$$2H^+ + 2e^- \longrightarrow H_2 \tag{1.2}$$

$$H_2O \longrightarrow \frac{1}{2}O_2 + 2H^+ + 2e^- \tag{1.3}$$

1.2 Photoelectrochemical water splitting

Due to the great abundance but intermittent nature of solar energy, many have sought to store this renewable energy in the form of hydrogen. A straightforward way of achieving this is to first convert solar energy into electricity. Then, subsequently, use the generated electricity for water splitting (Equation 1.1). In practice, this can be performed by pairing a solar cell with an electrolyzer. This method is called PV-electrolysis and is currently being used to produce green hydrogen (hydrogen produced from renewable energy) from solar energy. Nevertheless, PV-electrolysis requires two components, a photovoltaic device and an electrolyzer, to work together. Many techno-economic analyses have shown that the hydrogen generated using this method is too expensive to be economically competitive.[16,17] Photoelectrochemical (PEC) water splitting offers an alternative approach for solar to hydrogen conversion. This method utilizes a photoelectrode to harvest solar energy and directly perform the water splitting reaction.[18] Similar to an electrolyzer, PEC cells consist of an anode and a cathode where the oxidation reaction and the reduction reaction take place respectively. The main difference in the PEC cells is that at least one of the electrodes is a photoelectrode. A photoelectrode is an electrode made with semiconductor materials. The ability of semiconductor materials to perform direct solar to hydrogen conversion stems from the unique optoelectronic property of this class of materials.

1.2.1 Photoelectrochemical water splitting on semiconductors

Individual atom possess a set of atomic orbitals which are discrete electronic energy levels. As a larger number of atoms are brought together to form a material, the atomic orbitals combined and form bands of electronic states. The highest (in energy) filled band and the lowest unfilled band at 0 K are defined as the valence band (VB) and the conduction band (CB) respectively. The electrons in the valence band are localized on the atoms while the electrons in the conduction band are delocalized and can move freely within the crystal of the material. The energy gap between these two bands is referred to as the band gap (E_g). The electrons in the valence band can be excited to the conduction band if an energy greater than the band gap is supplied. At temperatures above absolute zero ($T > 0$ K), a fraction of the electrons in the valence band can be excited to the conduction band by thermal energy. At a given temperature, the larger the band gap, the smaller the number of electrons that can be promoted to the conduction band. Therefore, the

size of the band gap can determine the electrical conductivity of the material. In conductors, no band gap is present, the valence and the conduction bands overlap. The electrons can move freely between the two bands allowing great electrical conductivity. An insulator, on the other hand, has a prohibitively large band gap. The number of promoted electrons in the conduction band is extremely small, resulting in poor electrical conductivity. A semiconductor is a material with a low band gap energy. A small number of electrons can be promoted to the conduction band and resulting in certain electrical conductivity.

Apart from excitation from thermal energy, photons with energy greater than the band gap can also excite the valence band electrons into the conduction band. Once the electron is excited to the conduction band, either by photoexcitation or thermal excitation, an electron hole is left in the valence band (h^+). In addition to the contribution to the electrical conductivity of the material, the excited electrons and the holes can also undergo redox reactions, provided that the redox pairs have an appropriate E_{cell}. The excited electrons in the conduction band can undergo a reduction reaction provided the redox-active species has a reaction potential more positive than the conduction band edge energy. Conversely, the holes can undergo an oxidation reaction with the redox-active couple with a reaction potential less positive than the valence band edge energy.

1.2.2 PEC cells configuration

Multiple configurations of PEC cells have been proposed.[19] The simplest configuration utilize only one photoelectrode where either a photoanode (Figure 1.2A) or a photocathode (Figure 1.2B) is used in combination with a conventional counter electrode (typically Pt wire or graphite rod). Once illuminated with photons with energies greater than the semiconductor band gap, electrons are excited from the valence band to the conduction band. This creates photogenerated electron-hole pairs. During the operation, both electrodes are submerged in the electrolyte solution. Once submerged, the Fermi level (hypothetical energy state where the probability of finding an electron is equal to 50 %) of the photoelectrode equilibrates with the Fermi level of the solution, creating an electric field at the semiconductor–liquid junction (SCLJ). Depending on the type of the semiconductor, the built-in electric field will force either the photogenerated holes or electrons to the SCLJ to perform the redox reaction. The opposite photogenerated charge carrier is repelled from the surface of the semiconductor and is collected at the Ohmic contact at the back of the photoelectrode. The collected charge at the Ohmic contact can eventually travels, through an external circuit in certain device designs, to the counter electrode where the other half reaction takes place. In a photoanode, the built-in electric field drives the photogenerated holes to perform

the oxidation reaction at the surface of the electrode. The photogenerated electrons are pushed toward the Ohmic back contact and subsequently transferred to the counter electrode to perform the reduction reaction. Conversely, in a photocathode, the photogenerated electrons are pushed to the electrode surface while the photogenerated holes are collected at the Ohmic contact before flowing to the counter electrode.

To realize this device architecture, the photoelectrode has to generate enough photopotential to drive the water splitting reaction (1.23 V from the thermodynamic barrier plus the overpotential). In addition, the position of the conduction and the valence bands have to be appropriate to drive the HER and the OER respectively. Semiconductor materials that suit these requirements, for example, TiO_2, tend to have large band gaps and therefore can only harvest only a small portion of the solar radiation. Hence, devices made of large band gap semiconductors tend to suffer low solar-to-hydrogen conversion efficiency.

Many semiconductors require an external bias to supplement the photogenerated potential to drive the water splitting reaction. Despite the requirement of external bias in many cases, this configuration allows one to investigate the properties of the particular photoelectrode. Hence, this configuration is widely adopted and will also be employed in this thesis. It is worth noting that, when employing this one photoelectrode configuration for the purpose of studying the photoelectrode, the reference electrode is normally used to reference the applied potential.

To drive the water splitting reaction bias-free, two photoelectrodes (Figure 1.2C) are usually employed to generate enough photopotential. This can be referred to as a dual photoelectrode configuration.[20] Instead of using one semiconductor with a large band gap, this configuration allows ones to utilize two semiconductor materials which smaller band gaps to maximize solar energy. Many realizations of this configuration in performing bias-free water splitting reaction have been shown in the literature.[21–24]

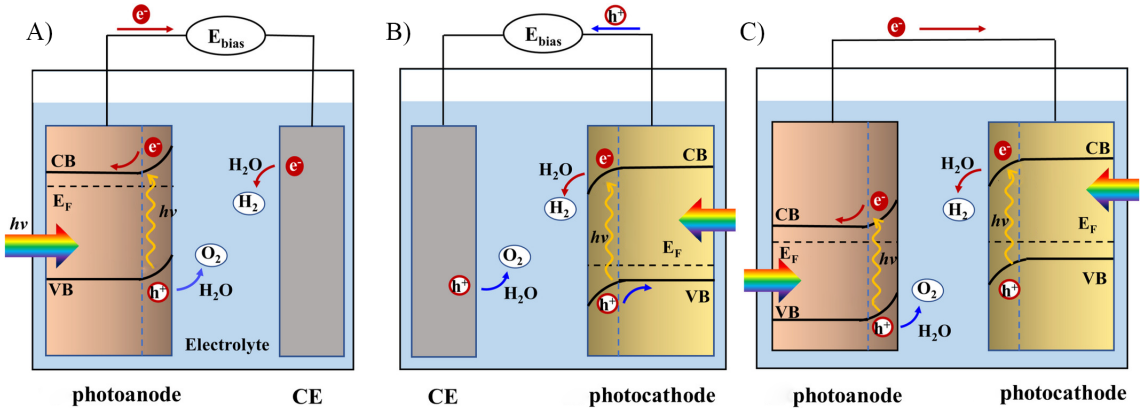

Figure 1.2: Scheme for the photoelectrochemical cells A) photoanode / counter counter electrode (CE) with external bias B) photocathode / counter electrode (CE) with external bias C) bias-free, dual photoelectrode configuration. Adapted from ref. [20]

1.2.3 WO_3 and $CuWO_4$ as photoanode materials

The property of semiconductor material highly impacts the performance of PEC cells. An ideal photoelectrode material should be made from an inexpensive material that can be easily fabricated to give a photoelectrode with excellent optoelectronic properties and high stability under extended operating conditions. The quest to find such ideal material is an ongoing endeavor. Metal oxides have been shown to have interesting properties as photoelectrode materials. Many metal oxides are semiconductors and have been found to be relatively stable under water splitting conditions. This class of materials can be relatively easy to fabricate into a thin film and must be processed under an oxygenated environment.[25] Hence, many oxides are inexpensive and can be produced on a large scale. Possible combinations of metal oxides are in a range of thousands,[25] providing a large sample pool to be explored.

Among the metal oxides, WO_3 has been shown to certain unique properties. This n-type binary oxide of W(VI) is non-toxic and inexpensive which give this material a potential to be used in large scale. WO_3 also shows great stability in acidic media, a rare behavior for a binary metal oxide semiconductor. Despite these intriguing properties, this oxide has relatively large indirect bandgap of 2.7-2.8 eV,[26,27] which limits WO_3 to harvest only a small part of the solar spectrum. The valence band maximum (VBM) of this material lies at 3 V vs. RHE but the conduction band minimum (CBM) lies at 0.3 V vs. RHE, not sufficient to perform the HER.[18] WO_3 has been found to have slow kinetics toward the OER. The products from the photoelectrolysis of water by WO_3 are found to be a mixture of molecular oxygen and peroxide species.[28] The oxidation of anions in the electrolyte, such as Cl^- and SO_4^{2-},[29] have also been reported. This is believed to be due to the slow kinetics toward the OER and the highly positive valence band position of this metal oxide.

This slow kinetics is normally regarded as a drawback for this material as a photoanode for solar water splitting. Nevertheless, WO_3 sluggish OER kinetics and its stability in acidic media makes this material particularly interesting for performing the alternative oxidation reaction, which will be the main focus of this thesis. Additionally, in the final part of this thesis, the investigation will expand to $CuWO_4$, a ternary metal tungstate which retain many advantages of WO_3, but process lower band gap.

1.3 HMF oxidation

1.3.1 Alternative reactions to the OER

Not only is the OER kinetically slower than the HER, but the oxygen it produces has low economic value as it can be produced more cheaply via condensation from the air. The production of oxygen via electrolysis has few applications such as in a submarine or in a spaceship where the supply of oxygen from the condensation from the air is hard to come by. Hydrogen, on the other hand, is the true target product of the water splitting reaction. Therefore, the sole purpose of the OER is to supply the HER with electrons. In addition, co-evolving hydrogen and oxygen gas in the same container poses the risk of explosion.

Considering the disadvantages of OER, many researchers have sought to replace the oxidation reaction at the photoanode with other oxidations with faster kinetics, lower thermodynamics potential barrier, and potentially give products with higher economic value and interest.[30–32] Examples of these alternative reactions includes glycerol oxidation to formic acid[33,34], glucose oxidation to glucaric acid[35], benzyl alcohol oxidation to benzoic acid[36–39] and chloride oxidation to chlorine[40,41]. Among these alternative reactions, the oxidation of 5-(hydroxymethyl)furfural (HMF) has received much attention in the past few years.[42–49] HMF is a biomass-derived product, in particular lignocellulosic biomass. Lignocellulose is considered to be the most abundant biomass on earth.[50] It can be found in many plant-based biomass such as sawdust, lawn trim, bagasse, and agricultural wastes.[51] There are three main polymer components in lignocellulose: cellulose, hemicellulose and lignin (Figure 1.3A). The proportion of these three polymers varies with the source of lignocellulose, but cellulose and hemicellulose normally account for around 60 %. The hydrolysis of both cellulose and hemicellulose liberate hexose sugars which can subsequently undergo dehydration to form HMF (Figure 1.3B).[52] With the abundance of lignocellulose, HMF can be considered a sustainable substrate to replace the water in the oxidation at the photoelectrode.

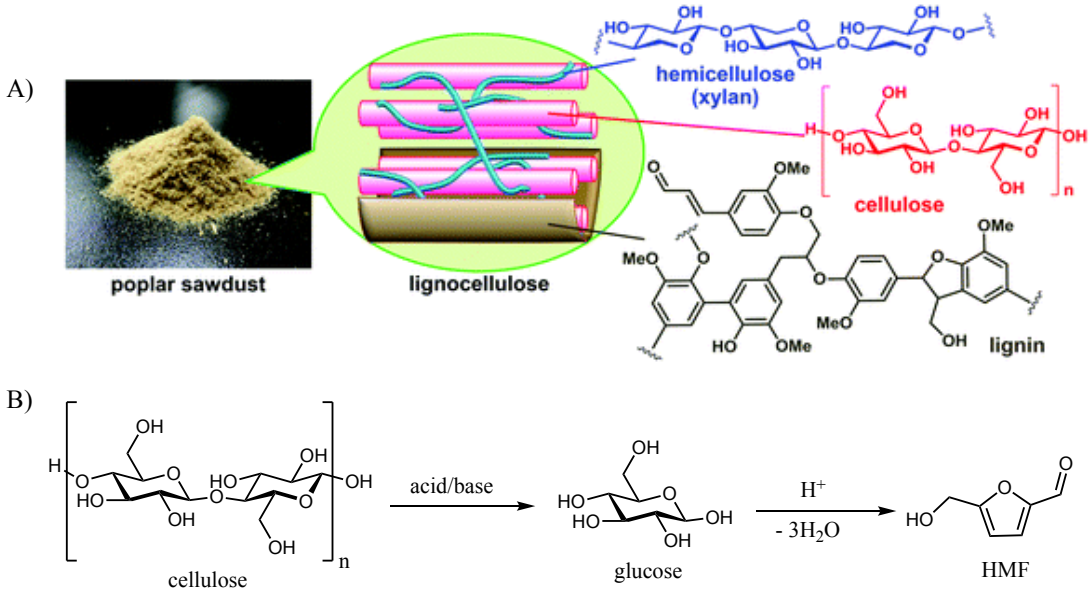

Figure 1.3: A) Component in lignocellulose biomass. B) HMF synthesis from hydrolysis of cellulose and subsequently followed by dehydration. Figure A is adapted from ref.[52] with the permission of © 2013 Royal Society of Chemistry Publishing

.

HMF can undergoes an overall 6-electrons oxidation to 2,5-furandicarboxylic acid (FDCA) in 3 sequential steps (Figure 1.4). HMF first undergoes a 2-electrons oxidation to either diformylfuran (DFF) or 5-hydroxymethyl-2-furandicarboxylic acid (HMFCA). These two intermediates then subsequently undergo another 2-electrons oxidation to form 5-formylfuran-2-carboxylic acid (FFCA). The final 2-electrons oxidation converts FFCA into the product FDCA. Yang and co-workers have calculated the standard reduction potential (E^o) of the 6-electrons oxidation from HMF to FDCA to be + 0.30 V. Nevertheless, the E^o of the 2-electrons oxidation from FFCA to FDCA, the final step in the oxidation to FDCA, is calculated to be + 0.43 V.[53] The standard reduction potential of HMF is significantly lower than that of water oxidation (1.23 V without overpotential), suggesting that the oxidation of HMF is thermodynamically more favorable.

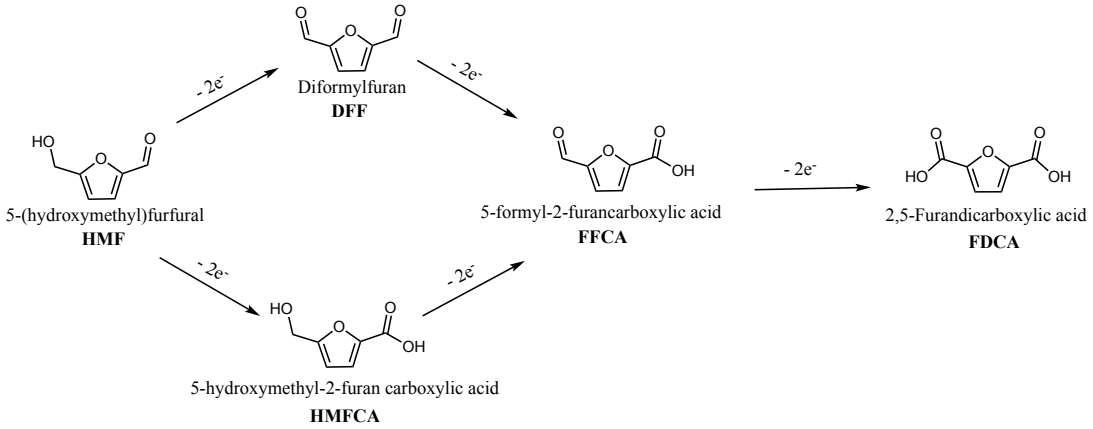

Figure 1.4: HMF oxidation to FDCA scheme

The product from HMF oxidation, FDCA, also has a higher commercial value than oxygen. One of the main use of FDCA is for the production of polyethylene furanoate (PEF). PEF shares many similar properties to Polyethylene terephthalate (PET), a plastic that is widely used for food and beverage packaging, with some even being superior. The lower gas permeability is one of the merits. In comparison to PET, the permeability of PEF to O_2 and CO_2 is 11 times and 19 times lower respectively[54,55], a great advantage for a material used for containing food and drinks. The Young's modulus of PEF has also been shown to be higher than PET. This can translate into a more resilient final products.[56] Furthermore, while FDCA which is one of the starting materials for making PEF is a biomass-derived compound, terepthalic acid, which is the monomer used to synthesize PET, is made predominantly from a petroleum-based compound.[57] This makes PEF more sustainable to synthesize compared to PET. The above-mentioned advantages of PEF have sparked an interest to use PEF as a replacement for PET.

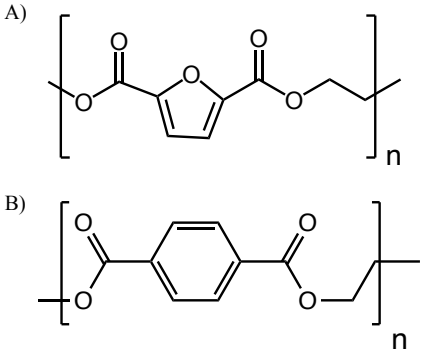

Figure 1.5: Structure of A) Polyethylene furanoate (PEF) and B) polyethylene terephthalate (PET)

1.3.2 Performing HMF oxidation

Multiple methods of performing HMF oxidation have been shown in the literature. One of the most employed methods is aerobic oxidation. Typically, the reaction is performed under elevated temperature and pressure over heterogeneous catalysts.[58–68] which commands additional energy input and added risks to the process. Other less common routes such as bioconversion[69–71] and photocatalysts[72,73] have also been reported, but examples of these approaches remains rare.

Electrochemical HMF oxidation has received attention as an alternative approach to aerobic oxidation. This approach allows the oxidation to be performed at milder conditions (usually at room temperature and pressure) compared to aerobic oxidation, with a high FDCA yield. In addition to this, oxygen is the final electron acceptor in aerobic oxidation. Oxygen is reduced to water, which is abundant and has low economical value. Electrochemical oxidation of HMF, on the other hand, is commonly paired with the HER which produces hydrogen as discussed earlier. Performing HMF oxidation via electrochemical oxidation not only offers milder operating conditions but also products with higher economical values.

For the electrochemical HMF oxidation, an electrocatalyst strongly affects the efficiency of the conversion (FDCA yield). Many electrocatalysts have been shown to date to have excellent catalytic activity toward HMF oxidation.[43,46,53] The electrocatalysts shown in the literature can be categorized into two groups: heterogeneous catalysts and homogeneous catalysts. Among the two, more examples of heterogeneous catalysts have been shown in literature. Various examples of heterogeneous catalysts for HMF oxidation are summarized in Table 1.1. The majority of the heterogeneous catalysts reported consist of transition metals and can be further categorized into noble metal-based and non-noble metal-based catalysts.

Despite excellent catalytic activity for many reactions of the noble metals, the electrocatalysts based on noble metals show low performance as a catalyst for HMF oxidation.[74,75]. In some reports, the noble metals catalysts offer lower onset potential for HMF oxidation but with low current densities.[53] The FDCA yield in many reports is also relatively low with the main products being one of the initial 2-electron oxidation products, DFF.

The non-noble metal electrocatalysts exhibit higher catalytic activities. Many of these catalysts compose of transition metals such as Mn, Fe, Co, Ni, Cu, and Mo in various forms such as oxides, hydroxide, oxy-hydroxide, and sulfides. Electrocatalysts form more complex structure such as metal-organic framework (MOF), covalent organic framework (COF), and layered double hydroxide (LDH) have also been reported. The FDAC yield of more than 90% was reported for various non-noble metal electrocatalysts.

Type	Catalyst	Supporting electrolyte	Operating applied potential (V vs. RHE)	HMF conversion (%)	yield FDCA (%)	Ref.
non-noble metals	MnO_x	0.1 M H_2SO_4	1.60	99.90	53.2	[75]
	FeOOH	0.1 M NaOH	1.71	16.00	1.6	[76]
	CoOOH	0.1 M NaOH	1.56	95.50	35.1	[76]
	Co-P	1.0 M KOH	1.42	$\sim$ 100	$\sim$ 90	[77]
	NiOOH	0.1 M NaOH	1.47	99.80	96.0	[76]
	Ni_3S_2	1.0 M KOH	1.42	100.00	98.0	[78]
	NiBDC (MOF)[a]	0.1 M KOH	1.55	$\sim$ 70	$\sim$ 60	[79]
	TpBpy-Ni (COF)[b]	0.1 M $LiClO_4$[b]	1.55	96.00	58.0	[80]
	Nanocrystaline Cu	0.1 M KOH	1.62	99.90	96.4	[81]
	$Cu(OH)_2$	1.0 M KOH	1.45	75.80	71.2	[82]
	MoO_2-FeP	1.0 M KOH	1.42	99.40	98.6	[83]
	NiFe LDH[c]	1.0 M KOH	1.23	99.00	98.0	[84]
	NiCoFe LDH[c]	1.0 M NaOH	1.52	95.50	84.9	[85]
noble metals	Pt	0.1 M H_2SO_4	2.00	99.90	0.1	[75]
	Au/C	0.1 M KOH	1.20	99.00	14.0	[74]
	Pd/C	0.1 M KOH	0.90	97.00	29.0	[74]
	Pd_1Au_2/C	0.1 M KOH	0.90	100.00	83.0	[74]

Table 1.1: Various heterogeneous electrocatalysts for HMF oxidation. a: BDC= terephthalic acid, MOF=metal–organic frameworks. b: Tp=triformylphloroglucinol, Bpy=5,5-diamino-2,2-bipyridine, COF=covalent organic frameworks, The pH of the electrolyte is 13. c: LDH=layered double hydroxide.

Electrochemical HMF oxidation in acidic media

While many high-performing electrocatalysts for HMF oxidation have been reported, the conditions employed are almost exclusively in basic conditions. Only a few reports have demonstrated such electrolysis in acidic media. Performing HMF oxidation in an acidic environment allows for a facile FDCA separation. The solubility of FDCA in the basic condition is much higher than in acidic media due to the deprotonation of the two carboxylate groups. FDCA would remain soluble in solution in basic conditions but would precipitate out in an acid. Nevertheless, a large amount of FDCA precipitation may hamper the reaction rate. Indeed, if the FDCA precipitates onto the electrode surfaces, the surface area of the will be reduced, ultimately lowering the rate of conversion. In addition to this, the precipitation may add additional complexity if this reaction were to be scaled up to an industrial scale. The precipitate may clog the tubing in a certain type of reactor which can lead to damage to the equipment. Therefore, the ideal operating scenario would be to have the product completely soluble during the reaction and allow the precipitation only after the reaction to separate the product.

Kubota and co-workers demonstrated the use of MnO_x as an anode material in acidic media.[75] The researchers demonstrated the electrocatalytic activity of MnO_x for performing HMF oxidation to FDCA, with a moderate FDCA yield of 53.8% a pH 1 H_2SO_4 solution. The main side product was found to be maleic acid (21.9%). The authors believe that the acidic conditions promote the furan ring-opening oxidation which leads to the formation of maleic acid. In this report, the authors used the differences in temperature to control the precipitation, as the solubility of FDCA increases with temperature. The reaction is performed at the elevated temperature of 60 °C in which FDCA is fully soluble. The solution is cooled down to room temperature after the reaction has finished allowing the precipitation of FDCA (Figure 1.6). In addition to this, the elevated temperature also increases the kinetics of the reaction allowing faster conversion of HMF. The facile FDCA separation can also be achieved in the basic condition by acidifying the solution after the reaction has been completed to allow FDCA precipitation. Nevertheless, in the industrial setting, increasing the reaction temperature can be achieved more easily than reducing the reaction pH. While raising reaction temperature requires additional heating elements, acidification of the solution requires the addition of acid into the solution. This adds complexity to the reaction design process and increase the cost of operation. On top of this, since the ion concentration in electrocatalytic cells is normally kept at a high salt concentration to maintain the high electrolyte conductivity, the amount of acid required is likely to be high. In addition to this, acidification also liberates heat which can be dangerous if not properly handled. This report is among the few electrochemical

HMF oxidations in acidic conditions.

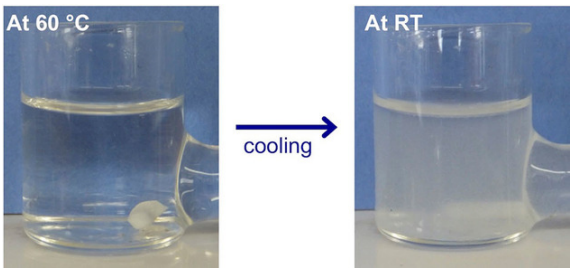

Figure 1.6: Photographs of the anodic compartment after the electrolysis of the solution containing 20 mM HMF using MnO_x as an anode at the elevated temperature and after being cooled to room temperature. The produced FDCA precipitates out after the solution is cooled down to room temperature. Adapted from ref.[75]

1.3.3 HMF oxidation to FDCA on PECs

Despite a number of publications on the alternative oxidation reactions on PECs[86–88], the oxidation of HMF to FDCA is rarely reported. Cha and co-workers first reported the oxidation of HMF to FDCA on $BiVO_4$ photoanode.[89] The team reported a high conversion yield of more than 99% and the Faradaic efficiency of more than 93 %. Nevertheless, a redox mediator (2,2,6,6-Tetramethylpiperidin-1-yl)oxyl (TEMPO) is required to drive the oxidation of HMF. No noticeable amount of HMF conversion was found in the absence of TEMPO. The illuminated surface of $BiVO_4$ alone is incapable of carrying out HMF oxidation. Rather, the photogenerated hole on $BiVO_4$ first oxidized TEMPO which is then oxidized HMF (Figure 1.7). Chadderdon and co-workers showed that the system reported by Cha and co-workers ($BiVO_4$ with TEMPO as a redox mediator) can be improved by the introduction of CoP_i electrocatalyst.[90] The $CoP_i/BiVO_4$ modified photoanode was found to have a lower onset potential of around 0.5 V for the oxidation of TEMPO compared to bare $BiVO_4$. The introduction of the CoP_i electrocatalysts layer also enhances the photocurrent and improves the selectivity toward the TEMPO oxidation over the OER. Despite improved onset potentials and selectivity toward TEMPO oxidation, the $CoP_i/BiVO_4$ modified photoanode shows negligible HMF conversion in the absence of TEMPO. The authors also aimed to improve the TEMPO oxidation rather than directly aiming at the oxidation of HMF.

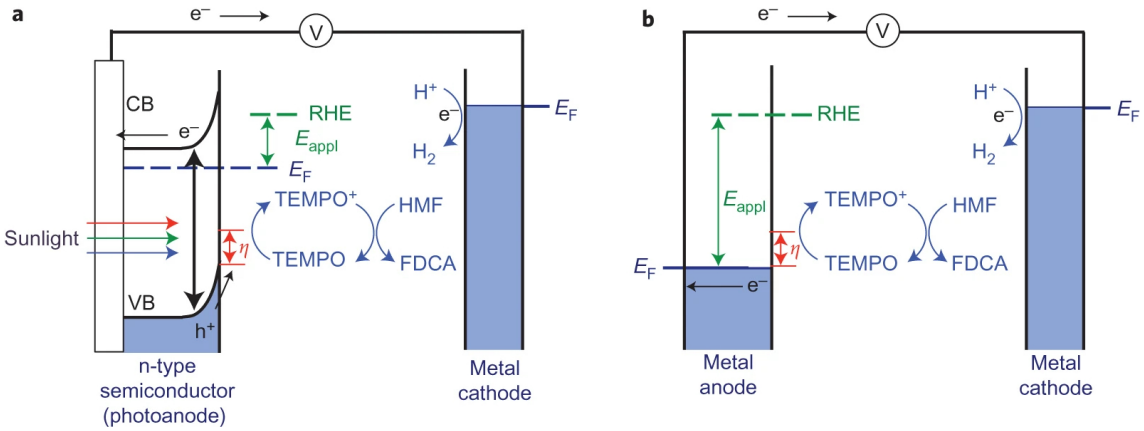

Figure 1.7: Schematic of TEMPO-mediated HMF oxidation on a) photoanode and b) metal anode. Here CB, VB and E_F are conduction band, valence band and Fermi energy respectively. Adapted from ref.[89] with the permission of © 2015 Springer Nature

Despite a high FDCA yield achieved with this approach, the use of a redox mediator adds another complexity to the product purification process which translates to higher energy, time, and capital investment in the product purification process. In addition, as previously explain,g one of the main use of FDCA is to synthesise PEF as a replacement for PET, the plastic used for water bottles. Since TEMPO has a yellow hue color, contamination of TEMPO in the FDCA would result in the resulting PEF having an unpleasant yellow hue. The contamination of TEMPO in the resulting water bottles would also raise a safety concern as TEMPO is highly water soluble and may redissolve into the water in the bottle. Therefore, a photoanode that can perform direct HMF oxidation to FDCA with high FDCA yield and Faradaic efficiency without the need for a redox mediator is desirable.

As discussed earlier, the WO_3 photoanode shows catalytic activities toward many alternative reactants with a moderate selectivity toward the OER. This illustrates the possibility for WO_3 towards the oxidation of HMF. Furthermore, the acid stability of WO_3 also illustrates the potential to perform HMF oxidation in an acidic media. These unique properties of WO_3 make this photoanode to be an intriguing material for mediator-free HMF oxidation.

1.4 Objectives

This thesis will discuss the use of WO_3 photoanode to oxidize HMF to FDCA. First, the activity of WO_3 photoanode in oxidizing HMF to FDCA will be discussed in chapter 2. The evolution of the intermediates and products will also be discussed in this chapter. Kinetic models will be used to elaborate possible degradation steps during the photoelectrolysis. Next, the effect of the applied potential on the selectivity between HMF oxidation and the water oxidation reaction is elaborated in chapter 3. A phenological model to predict the selectivity among competing reactions on photoelectrodes as a function of the applied potential was developed and will be discussed here. The model requires only the information readily obtained from linear sweep voltammograms and can be used as a quick tool to give a rough estimate of the selectivity of competing reactions. Strategies to improve FDCA yield will be discussed in chapter 4. Various electrocatalysts for alcohol and aldehyde oxidation will be fabricated onto the surface of the WO_3 photoanode, and the effect of each of the electrocatalysts will be discussed. In chapter 5, the scope of the study will be expanded to the effect oxygen vacancy, a common dopant in metal oxides, to the physical and photoelectrochemical properties of $CuWO_4$. Finally, the conclusions and outlooks of the thesis will be presented in chapter 6.

Bibliography

[1] Fankhauser, S.; Smith, S. M.; Allen, M.; Axelsson, K.; Hale, T.; Hepburn, C.; Kendall, J. M.; Khosla, R.; Lezaun, J.; Mitchell-Larson, E., et al. The meaning of net zero and how to get it right. *Nature Climate Change* **2022**, *12*, 15–21.

[2] Statistical Review of World Energy 2022. *The British Petroleum Company* **2022**, https://www.bp.com/content/dam/bp/business-sites/en/global/corporate/pdfs/energy-economics/statistical-review/bp-stats-review-2022-full-report.pdf.

[3] Gueymard, C. A.; Myers, D.; Emery, K. Proposed reference irradiance spectra for solar energy systems testing. *Solar energy* **2002**, *73*, 443–467.

[4] Ritchie, H.; Roser, M. Land Use. *Our World in Data* **2013**, https://ourworldindata.org/land-use.

[5] https://tinyurl.com/AnnualSunshine.

[6] Kalair, A. R.; Abas, N.; Seyedmahmoudian, M.; Rauf, S.; Stojcevski, A.; Khan, N. Duck curve leveling in renewable energy integrated grids using internet of relays. *Journal of Cleaner Production* **2021**, *294*, 126294.

[7] Hannah Ritchie, M. R.; Rosado, P. Energy. *Our World in Data* **2020**, https://ourworldindata.org/energy.

[8] Hannah Ritchie, M. R.; Rosado, P. CO and Greenhouse Gas Emissions. *Our World in Data* **2020**, https://ourworldindata.org/co2-and-other-greenhouse-gas-emissions.

[9] Tan, K. M.; Babu, T. S.; Ramachandaramurthy, V. K.; Kasinathan, P.; Solanki, S. G.; Raveendran, S. K. Empowering smart grid: A comprehensive review of energy storage technology and application with renewable energy integration. *Journal of Energy Storage* **2021**, *39*, 102591.

[10] Wang, W.; Yuan, B.; Sun, Q.; Wennersten, R. Application of energy storage in integrated energy systems—A solution to fluctuation and uncertainty of renewable energy. *Journal of Energy Storage* **2022**, *52*, 104812.

[11] Chu, S. The science of photons to fuel. AIP Conference Proceedings. 2008; pp 266–282.

[12] Shet, S. P.; Priya, S. S.; Sudhakar, K.; Tahir, M. A review on current trends in potential use of metal-organic framework for hydrogen storage. *International Journal of Hydrogen Energy* **2021**, *46*, 11782–11803.

[13] Moradi, R.; Groth, K. M. Hydrogen storage and delivery: Review of the state of the art technologies and risk and reliability analysis. *International Journal of Hydrogen Energy* **2019**, *44*, 12254–12269.

[14] The Battery That Flies. 2022; `https://www.nytimes.com/2022/04/16/business/beta-electric-airplane.html`.

[15] Li, S.; Thomas, A. *Advanced Nanomaterials for Electrochemical-Based Energy Conversion and Storage*; Elsevier, 2020; pp 393–423.

[16] Acar, C.; Dincer, I. Comparative assessment of hydrogen production methods from renewable and non-renewable sources. *International journal of hydrogen energy* **2014**, *39*, 1–12.

[17] Nowotny, J.; Bak, T.; Chu, D.; Fiechter, S.; Murch, G. E.; Veziroglu, T. N. Sustainable practices: solar hydrogen fuel and education program on sustainable energy systems. *International journal of hydrogen energy* **2014**, *39*, 4151–4157.

[18] Sivula, K.; Van De Krol, R. Semiconducting materials for photoelectrochemical energy conversion. *Nature Reviews Materials* **2016**, *1*, 1–16.

[19] Sivula, K. *Photoelectrochemical Solar Fuel Production*; Springer, 2016; pp 493–512.

[20] Cheng, C.; Zhang, W.; Chen, X.; Peng, S.; Li, Y. Strategies for improving photoelectrochemical water splitting performance of Si-based electrodes. *Energy Science & Engineering* **2022**, *10*, 1526–1543.

[21] Zhang, Y.; Wang, L.; Xu, X. A bias-free CuBi 2 O 4–CuWO 4 tandem cell for solar-driven water splitting. *Inorganic Chemistry Frontiers* **2021**, *8*, 3863–3870.

[22] Bornoz, P.; Abdi, F. F.; Tilley, S. D.; Dam, B.; Van De Krol, R.; Grätzel, M.; Sivula, K. A bismuth vanadate–cuprous oxide tandem cell for overall solar water splitting. *The Journal of Physical Chemistry C* **2014**, *118*, 16959–16966.

[23] Chen, M.; Liu, Y.; Li, C.; Li, A.; Chang, X.; Liu, W.; Sun, Y.; Wang, T.; Gong, J. Spatial control of cocatalysts and elimination of interfacial defects towards efficient and robust CIGS photocathodes for solar water splitting. *Energy & Environmental Science* **2018**, *11*, 2025–2034.

[24] Kim, J. H.; Kaneko, H.; Minegishi, T.; Kubota, J.; Domen, K.; Lee, J. S. Overall photoelectrochemical water splitting using tandem cell under simulated sunlight. *ChemSusChem* **2016**, *9*, 61–66.

[25] Abdi, F. F.; Berglund, S. P.; Krol, R. v. d. *Photoelectrochemical Solar Fuel Production*; Springer, 2016; pp 355–391.

[26] Kang, D.; Kim, T. W.; Kubota, S. R.; Cardiel, A. C.; Cha, H. G.; Choi, K.-S. Electrochemical synthesis of photoelectrodes and catalysts for use in solar water splitting. *Chemical reviews* **2015**, *115*, 12839–12887.

[27] González-Borrero, P.; Sato, F.; Medina, A.; Baesso, M. L.; Bento, A. C.; Baldissera, G.; Persson, C.; Niklasson, G. A.; Granqvist, C. G.; Ferreira da Silva, A. Optical band-gap determination of nanostructured WO 3 film. *Applied Physics Letters* **2010**, *96*, 061909.

[28] Augustynski, J.; Solarska, R.; Hagemann, H.; Santato, C. Nanostructured thin-film tungsten trioxide photoanodes for solar water and sea-water splitting. Solar Hydrogen and Nanotechnology. 2006; pp 136–144.

[29] Hill, J. C.; Choi, K.-S. Effect of electrolytes on the selectivity and stability of n-type WO3 photoelectrodes for use in solar water oxidation. *The Journal of Physical Chemistry C* **2012**, *116*, 7612–7620.

[30] Sayama, K. Production of high-value-added chemicals on oxide semiconductor photoanodes under visible light for solar chemical-conversion processes. *ACS Energy Letters* **2018**, *3*, 1093–1101.

[31] Xu, Y.; Zhang, B. Recent advances in electrochemical hydrogen production from water assisted by alternative oxidation reactions. *ChemElectroChem* **2019**, *6*, 3214–3226.

[32] Bender, M. T.; Yuan, X.; Choi, K.-S. Alcohol oxidation as alternative anode reactions paired with (photo) electrochemical fuel production reactions. *Nature Communications* **2020**, *11*, 1–4.

[33] Han, X.; Sheng, H.; Yu, C.; Walker, T. W.; Huber, G. W.; Qiu, J.; Jin, S. Electrocatalytic oxidation of glycerol to formic acid by CuCo2O4 spinel oxide nanostructure catalysts. *ACS Catalysis* **2020**, *10*, 6741–6752.

[34] Chen, Y.; Lavacchi, A.; Miller, H.; Bevilacqua, M.; Filippi, J.; Innocenti, M.; Marchionni, A.; Oberhauser, W.; Wang, L.; Vizza, F. Nanotechnology makes biomass electrolysis more energy efficient than water electrolysis. *Nature communications* **2014**, *5*, 1–6.

[35] Liu, W.-J.; Xu, Z.; Zhao, D.; Pan, X.-Q.; Li, H.-C.; Hu, X.; Fan, Z.-Y.; Wang, W.-K.; Zhao, G.-H.; Jin, S., et al. Efficient electrochemical production of glucaric acid and H2 via glucose electrolysis. *Nature communications* **2020**, *11*, 1–11.

[36] Liu, G.; Zhang, X.; Zhao, C.; Xiong, Q.; Gong, W.; Wang, G.; Zhang, Y.; Zhang, H.; Zhao, H. Electrocatalytic oxidation of benzyl alcohol for simultaneously promoting H 2 evolution by a Co 0.83 Ni 0.17/activated carbon electrocatalyst. *New Journal of Chemistry* **2018**, *42*, 6381–6388.

[37] Chen, X.; Zhong, X.; Yuan, B.; Li, S.; Gu, Y.; Zhang, Q.; Zhuang, G.; Li, X.; Deng, S.; Wang, J.-g. Defect engineering of nickel hydroxide nanosheets by Ostwald ripening for enhanced selective electrocatalytic alcohol oxidation. *Green Chemistry* **2019**, *21*, 578–588.

[38] Zheng, J.; Chen, X.; Zhong, X.; Li, S.; Liu, T.; Zhuang, G.; Li, X.; Deng, S.; Mei, D.; Wang, J.-G. Hierarchical porous NC@ CuCo nitride nanosheet networks: highly efficient bifunctional electrocatalyst for overall water splitting and selective electrooxidation of benzyl alcohol. *Advanced Functional Materials* **2017**, *27*, 1704169.

[39] You, B.; Liu, X.; Liu, X.; Sun, Y. Efficient H2 evolution coupled with oxidative refining of alcohols via a hierarchically porous nickel bifunctional electrocatalyst. *Acs Catalysis* **2017**, *7*, 4564–4570.

[40] Luo, W.; Yang, Z.; Li, Z.; Zhang, J.; Liu, J.; Zhao, Z.; Wang, Z.; Yan, S.; Yu, T.; Zou, Z. Solar hydrogen generation from seawater with a modified BiVO4 photoanode. *Energy & Environmental Science* **2011**, *4*, 4046–4051.

[41] Iguchi, S.; Miseki, Y.; Sayama, K. Efficient hypochlorous acid (HClO) production via photoelectrochemical solar energy conversion using a BiVO 4-based photoanode. *Sustainable Energy & Fuels* **2018**, *2*, 155–162.

[42] Zhao, D.; Su, T.; Wang, Y.; Varma, R. S.; Len, C. Recent advances in catalytic oxidation of 5-hydroxymethylfurfural. *Molecular Catalysis* **2020**, *495*, 111133.

[43] Zhao, Y.; Cai, M.; Xian, J.; Sun, Y.; Li, G. Recent advances in the electrocatalytic synthesis of 2, 5-furandicarboxylic acid from 5-(hydroxymethyl) furfural. *Journal of Materials Chemistry A* **2021**, *9*, 20164–20183.

[44] Li, C.; Na, Y. Recent Advances in Photocatalytic Oxidation of 5-Hydroxymethylfurfural. *ChemPhotoChem* **2021**, *5*, 502–511.

[45] Pal, P.; Saravanamurugan, S. Recent advances in the development of 5-hydroxymethylfurfural oxidation with base (nonprecious)-metal-containing catalysts. *ChemSusChem* **2019**, *12*, 145–163.

[46] Simoska, O.; Rhodes, Z.; Weliwatte, S.; Cabrera-Pardo, J. R.; Gaffney, E. M.; Lim, K.; Minteer, S. D. Advances in Electrochemical Modification Strategies of 5-Hydroxymethylfurfural. *ChemSusChem* **2021**, *14*, 1674–1686.

[47] Zhao, Y.; Cai, M.; Xian, J.; Sun, Y.; Li, G. Recent advances in the electrocatalytic synthesis of 2, 5-furandicarboxylic acid from 5-(hydroxymethyl) furfural. *Journal of Materials Chemistry A* **2021**, *9*, 20164–20183.

[48] Zhang, Z.; Deng, K. Recent advances in the catalytic synthesis of 2, 5-furandicarboxylic acid and its derivatives. *Acs Catalysis* **2015**, *5*, 6529–6544.

[49] Kucherov, F. A.; Romashov, L. V.; Galkin, K. I.; Ananikov, V. P. Chemical transformations of biomass-derived C6-furanic platform chemicals for sustainable energy research, materials science, and synthetic building blocks. *ACS sustainable chemistry & engineering* **2018**, *6*, 8064–8092.

[50] Abdel-Hamid, A. M.; Solbiati, J. O.; Cann, I. K. *Advances in applied microbiology*; Elsevier, 2013; Vol. 82; pp 1–28.

[51] Isikgor, F. H.; Becer, C. R. Lignocellulosic biomass: a sustainable platform for the production of bio-based chemicals and polymers. *Polymer Chemistry* **2015**, *6*, 4497–4559.

[52] Kobayashi, H.; Fukuoka, A. Synthesis and utilisation of sugar compounds derived from lignocellulosic biomass. *Green Chemistry* **2013**, *15*, 1740–1763.

[53] Yang, Y.; Mu, T. Electrochemical oxidation of biomass derived 5-hydroxymethylfurfural (HMF): pathway, mechanism, catalysts and coupling reactions. *Green Chemistry* **2021**, *23*, 4228–4254.

[54] Burgess, S. K.; Karvan, O.; Johnson, J.; Kriegel, R. M.; Koros, W. J. Oxygen sorption and transport in amorphous poly (ethylene furanoate). *Polymer* **2014**, *55*, 4748–4756.

[55] Burgess, S. K.; Kriegel, R. M.; Koros, W. J. Carbon dioxide sorption and transport in amorphous poly (ethylene furanoate). *Macromolecules* **2015**, *48*, 2184–2193.

[56] Loos, K.; Zhang, R.; Pereira, I.; Agostinho, B.; Hu, H.; Maniar, D.; Sbirrazzuoli, N.; Silvestre, A. J.; Guigo, N.; Sousa, A. F. A perspective on PEF synthesis, properties, and end-life. *Frontiers in Chemistry* **2020**, *8*, 585.

[57] Pacheco, J. J.; Davis, M. E. Synthesis of terephthalic acid via Diels-Alder reactions with ethylene and oxidized variants of 5-hydroxymethylfurfural. *Proceedings of the National Academy of Sciences* **2014**, *111*, 8363–8367.

[58] Casanova, O.; Iborra, S.; Corma, A. Biomass into chemicals: aerobic oxidation of 5-hydroxymethyl-2-furfural into 2, 5-furandicarboxylic acid with gold nanoparticle catalysts. *ChemSusChem: Chemistry & Sustainability Energy & Materials* **2009**, *2*, 1138–1144.

[59] Villa, A.; Schiavoni, M.; Campisi, S.; Veith, G. M.; Prati, L. Pd-modified Au on carbon as an effective and durable catalyst for the direct oxidation of HMF to 2, 5-furandicarboxylic acid. *ChemSusChem* **2013**, *6*, 609–612.

[60] Gao, Z.; Xie, R.; Fan, G.; Yang, L.; Li, F. Highly efficient and stable bimetallic AuPd over La-doped Ca–Mg–Al layered double hydroxide for base-free aerobic oxidation of 5-hydroxymethylfurfural in water. *ACS Sustainable Chemistry & Engineering* **2017**, *5*, 5852–5861.

[61] Rathod, P. V.; Jadhav, V. H. Efficient method for synthesis of 2, 5-furandicarboxylic acid from 5-hydroxymethylfurfural and fructose using Pd/CC catalyst under aqueous conditions. *ACS Sustainable Chemistry & Engineering* **2018**, *6*, 5766–5771.

[62] Ke, C.; Li, M.; Fan, G.; Yang, L.; Li, F. Pt Nanoparticles Supported on Nitrogen-Doped-Carbon-Decorated CeO2 for Base-Free Aerobic Oxidation of 5-Hydroxymethylfurfural. *Chemistry–An Asian Journal* **2018**, *13*, 2714–2722.

[63] Pichler, C. M.; Al-Shaal, M. G.; Gu, D.; Joshi, H.; Ciptonugroho, W.; Schüth, F. Ruthenium Supported on High-Surface-Area Zirconia as an Efficient Catalyst for the Base-Free Oxidation of 5-Hydroxymethylfurfural to 2, 5-Furandicarboxylic Acid. *ChemSusChem* **2018**, *11*, 2083–2090.

[64] Xie, J.; Nie, J.; Liu, H. Aqueous-phase selective aerobic oxidation of 5-hydroxymethylfurfural on Ru/C in the presence of base. *Chinese Journal of Catalysis* **2014**, *35*, 937–944.

[65] Hayashi, E.; Komanoya, T.; Kamata, K.; Hara, M. Heterogeneously-catalyzed aerobic oxidation of 5-hydroxymethylfurfural to 2, 5-furandicarboxylic acid with MnO2. *ChemSusChem* **2017**, *10*, 654–658.

[66] Rao, K. T. V.; Rogers, J. L.; Souzanchi, S.; Dessbesell, L.; Ray, M. B.; Xu, C. Inexpensive but Highly Efficient Co–Mn Mixed-Oxide Catalysts for Selective Oxidation of 5-Hydroxymethylfurfural to 2, 5-Furandicarboxylic Acid. *ChemSusChem* **2018**, *11*, 3323–3334.

[67] Yan, Y.; Li, K.; Zhao, J.; Cai, W.; Yang, Y.; Lee, J.-M. Nanobelt-arrayed vanadium oxide hierarchical microspheres as catalysts for selective oxidation of 5-hydroxymethylfurfural toward 2, 5-diformylfuran. *Applied Catalysis B: Environmental* **2017**, *207*, 358–365.

[68] Zhou, C.; Deng, W.; Wan, X.; Zhang, Q.; Yang, Y.; Wang, Y. Functionalized carbon nanotubes for biomass conversion: the base-free aerobic oxidation of 5-hydroxymethylfurfural to 2, 5-furandicarboxylic acid over platinum supported on a carbon nanotube catalyst. *ChemCatChem* **2015**, *7*, 2853–2863.

[69] Becerra, M. L.; Lizarazo, L. M.; Rojas, H. A.; Prieto, G. A.; Martinez, J. J. Biotransformation of 5-hydroxymethylfurfural and furfural with bacteria of bacillus genus. *Biocatalysis and Agricultural Biotechnology* **2022**, *39*, 102281.

[70] Sayed, M.; Gaber, Y.; Junghus, F.; Martín, E. V.; Pyo, S.-H.; Hatti-Kaul, R. Oxidation of 5-hydroxymethylfurfural with a novel aryl alcohol oxidase from Mycobacterium sp. MS1601. *Microbial Biotechnology* **2022**,

[71] Jiménez, D. J.; Korenblum, E.; van Elsas, J. D. Novel multispecies microbial consortia involved in lignocellulose and 5-hydroxymethylfurfural bioconversion. *Applied Microbiology and Biotechnology* **2014**, *98*, 2789–2803.

[72] Bao, X.; Liu, M.; Wang, Z.; Dai, D.; Wang, P.; Cheng, H.; Liu, Y.; Zheng, Z.; Dai, Y.; Huang, B. Photocatalytic Selective Oxidation of HMF Coupled with H2 Evolution on Flexible Ultrathin g-C3N4 Nanosheets with Enhanced N–H Interaction. *ACS Catalysis* **2022**, *12*, 1919–1929.

[73] Ye, H.-F.; Shi, R.; Yang, X.; Fu, W.-F.; Chen, Y. P-doped ZnxCd1- xS solid solutions as photocatalysts for hydrogen evolution from water splitting coupled with photocatalytic oxidation of 5-hydroxymethylfurfural. *Applied Catalysis B: Environmental* **2018**, *233*, 70–79.

[74] Chadderdon, D. J.; Xin, L.; Qi, J.; Qiu, Y.; Krishna, P.; More, K. L.; Li, W. Electrocatalytic oxidation of 5-hydroxymethylfurfural to 2, 5-furandicarboxylic acid on supported Au and Pd bimetallic nanoparticles. *Green Chemistry* **2014**, *16*, 3778–3786.

[75] Kubota, S. R.; Choi, K.-S. Electrochemical Oxidation of 5-Hydroxymethylfurfural to 2, 5-Furandicarboxylic Acid (FDCA) in Acidic Media Enabling Spontaneous FDCA Separation. *ChemSusChem* **2018**, *11*, 2138–2145.

[76] Taitt, B. J.; Nam, D.-H.; Choi, K.-S. A comparative study of nickel, cobalt, and iron oxyhydroxide anodes for the electrochemical oxidation of 5-hydroxymethylfurfural to 2, 5-furandicarboxylic acid. *Acs Catalysis* **2018**, *9*, 660–670.

[77] Jiang, N.; You, B.; Boonstra, R.; Terrero Rodriguez, I. M.; Sun, Y. Integrating electrocatalytic 5-hydroxymethylfurfural oxidation and hydrogen production via Co–P-derived electrocatalysts. *ACS Energy Letters* **2016**, *1*, 386–390.

[78] You, B.; Liu, X.; Jiang, N.; Sun, Y. A general strategy for decoupled hydrogen production from water splitting by integrating oxidative biomass valorization. *Journal of the American Chemical society* **2016**, *138*, 13639–13646.

[79] Cai, M.; Zhang, Y.; Zhao, Y.; Liu, Q.; Li, Y.; Li, G. Two-dimensional metal–organic framework nanosheets for highly efficient electrocatalytic biomass 5-(hydroxymethyl) furfural (HMF) valorization. *Journal of Materials Chemistry A* **2020**, *8*, 20386–20392.

[80] Cai, M.; Ding, S.; Gibbons, B.; Yang, X.; Kessinger, M. C.; Morris, A. J. Nickel (ii)-modified covalent-organic framework film for electrocatalytic oxidation of 5-hydroxymethylfurfural (HMF). *Chemical Communications* **2020**, *56*, 14361–14364.

[81] Nam, D.-H.; Taitt, B. J.; Choi, K.-S. Copper-based catalytic anodes to produce 2, 5-furandicarboxylic acid, a biomass-derived alternative to terephthalic acid. *Acs Catalysis* **2018**, *8*, 1197–1206.

[82] Chen, H.; Wang, J.; Yao, Y.; Zhang, Z.; Yang, Z.; Li, J.; Chen, K.; Lu, X.; Ouyang, P.; Fu, J. Cu- Ni Bimetallic Hydroxide Catalyst for Efficient Electrochemical Conversion of 5-Hydroxymethylfurfural to 2, 5-Furandicarboxylic Acid. *ChemElectroChem* **2019**, *6*, 5797–5801.

[83] Yang, G.; Jiao, Y.; Yan, H.; Xie, Y.; Wu, A.; Dong, X.; Guo, D.; Tian, C.; Fu, H. Interfacial engineering of MoO2-FeP heterojunction for highly efficient hydrogen evolution coupled with biomass electrooxidation. *Advanced Materials* **2020**, *32*, 2000455.

[84] Liu, W.-J.; Dang, L.; Xu, Z.; Yu, H.-Q.; Jin, S.; Huber, G. W. Electrochemical oxidation of 5-hydroxymethylfurfural with NiFe layered double hydroxide (LDH) nanosheet catalysts. *ACS Catalysis* **2018**, *8*, 5533–5541.

[85] Zhang, M.; Liu, Y.; Liu, B.; Chen, Z.; Xu, H.; Yan, K. Trimetallic NiCoFe-layered double hydroxides nanosheets efficient for oxygen evolution and highly selective oxidation of biomass-derived 5-hydroxymethylfurfural. *Acs Catalysis* **2020**, *10*, 5179–5189.

[86] He, Y.; Zhang, H.; Wang, Z.; Zheng, Z.; Wang, P.; Liu, Y.; Cheng, H.; Zhang, X.; Da, Y.; Huang, B. Photoelectrochemical Oxidation of Amines to Imines and Production of Hydrogen through Mo-Doped BiVO4 Photoanode. *ACS omega* **2022**, *7*, 12816–12824.

[87] Hambourger, M.; Gervaldo, M.; Svedruzic, D.; King, P. W.; Gust, D.; Ghirardi, M.; Moore, A. L.; Moore, T. A. [FeFe]-hydrogenase-catalyzed H2 production in a photoelectrochemical biofuel cell. *Journal of the American Chemical Society* **2008**, *130*, 2015–2022.

[88] Antón-García, D.; Edwardes Moore, E.; Bajada, M. A.; Eisenschmidt, A.; Oliveira, A. R.; Pereira, I. A.; Warnan, J.; Reisner, E. Photoelectrochemical hybrid cell for unbiased CO2 reduction coupled to alcohol oxidation. *Nature Synthesis* **2022**, *1*, 77–86.

[89] Cha, H. G.; Choi, K.-S. Combined biomass valorization and hydrogen production in a photoelectrochemical cell. *Nature chemistry* **2015**, *7*, 328–333.

[90] Chadderdon, D. J.; Wu, L.-P.; McGraw, Z. A.; Panthani, M.; Li, W. Heterostructured bismuth vanadate/cobalt phosphate photoelectrodes promote TEMPO-mediated oxidation of 5-hydroxymethylfurfural. *ChemElectroChem* **2019**, *6*, 3387–3392.

Chapter 2

Photoelectrolysis of HMF on WO_3 Photoanode

This chapter has been adapted from the following article: **Plainpan, N.**; Lhermitte, C. R.; Canjura, P.; Boudoire, F.; Sivula, K. Direct photoelectrochemical oxidation of hydroxymethylfurfural on tungsten trioxide photoanodes. RSC Advances **2021**, 11, 198–202.[1]

2.1 Introduction

In this chapter, we demonstrate for the first time that WO_3 photoanodes can directly oxidize HMF in aqueous electrolyte under illumination. Our detailed analysis of the resulting product distribution and reaction kinetics gives important insights into the reaction pathways, suggesting routes to further enhance the performance.

Based on the unique PEC properties of WO_3, we hypothesized that it could provide advantages toward the direct photo-oxidization of HMF. Specifically, compared to $BiVO_4$, which has a valence band maximum (VBM) at a potential of 2.4 V vs. NHE,[2] the VBM of WO_3 is considerably more oxidizing at 3.1 – 3.2 V vs. NHE[2] suggesting an increased driving force to overcome the activation energy barrier associated with HMF oxidation. In addition, WO_3 also demonstrates poor selectivity for the OER, even in aqueous solution. In fact, WO_3 often prefers to oxidize other small molecules, or anions such as MeOH, and chloride.[3–7] This can reduce or eliminate competition from water oxidation when operating in aqueous conditions. This strategy has been employed in the past, where WO_3 was used to oxidize alcohols photoelectrochemically in aqueous solution.[8] Finally, WO_3 is easy to prepare and demonstrates stability in acidic aqueous media. These properties are highly

desirable for a PEC material if it is to be employed in an H_2 producing PEC cell since acidic conditions favour the production of H_2 from water.

2.2 Results and discussions

Tungsten trioxide photoanodes prepared by the sol–gel method (see Appendix A for details) were first examined for HMF oxidation in aqueous electrolyte using linear sweep voltammetry (LSV), and the results were compared to $BiVO_4$ and Fe_2O_3 (similar photoanode materials, for synthesis see Appendix A). Figure 2.1A–C shows LSV results in the dark and under simulated 1 Sun illumination, with and without 5 mM HMF in the electrolyte. We note that different pHs were used due to the stability limits of each material, thus all LSVs are plotted versus the reversible hydrogen electrode, RHE. We also note that HMF oxidation is favoured under basic conditions, which should be advantageous for $BiVO_4$ and Fe_2O_3.[9–12] However, while the current density, J, exhibits similar behaviour with and without HMF with $BiVO_4$ and Fe_2O_3 photoanodes, a clear difference is observed with WO_3. In a pH 4 electrolyte containing no HMF, WO_3 shows a photocurrent onset potential at 0.63 V vs. RHE and a saturated photocurrent density of 1.2 mA cm^2. However, when 5 mM HMF is added to the solution, the onset potential shifts by 100 mV, and the saturated photocurrent density increases by 26 % to 1.52 mA cm^2. The unresponsiveness of $BiVO_4$ and Fe_2O_3 to HMF suggests that these photoanodes do not favour photo-oxidization of HMF over the OER, however the significant shift of the J–E curve observed with WO_3 suggests that WO_3 possesses a unique ability to oxidize the HMF substrate directly. Although these results alone do not directly confirm the inability of either Fe_2O_3 or $BiVO_4$ to oxidize HMF directly, other groups have demonstrated that $BiVO_4$ in particular is unable to perform this reaction on its own.[13] Furthermore, the marked J-E shift observed with the WO_3 suggests that the HMF is a kinetically easier substrate to oxidize. In this case, if a photoanode were capable of directly oxidizing this substrate, then we would expect to observe a shift toward the more positive potential in the photocurrent onset.

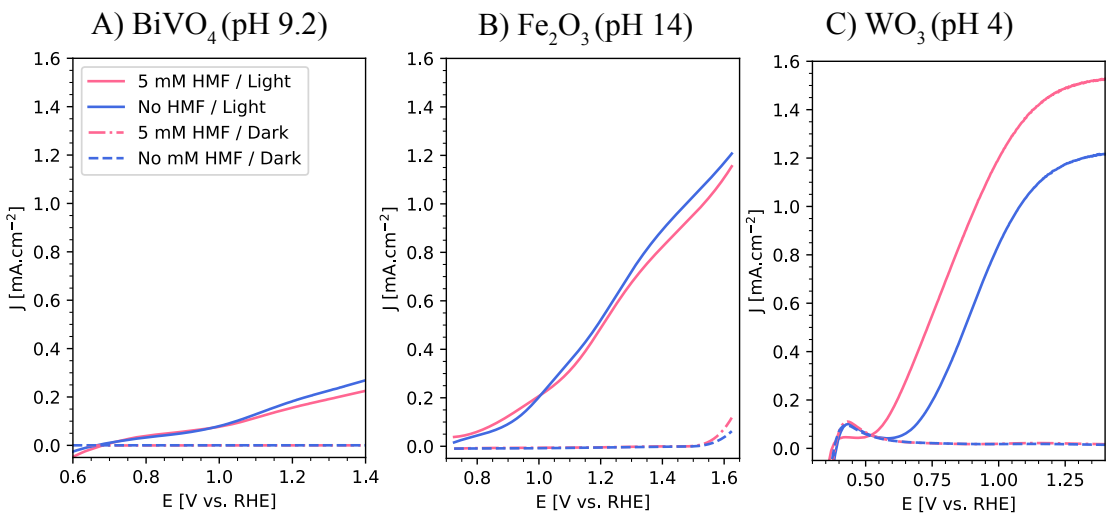

Figure 2.1: Linear sweep voltammogram of (A) $BiVO_4$ photoanode in pH 9.2 NaB_i buffer (+5 mM HMF), (B) α-Fe_2O_3 photoelectrode in pH 14 NaOH electrolyte (+5 mM HMF), and (C) WO_3 photoanode in pH 4 NaP_i buffer (+5 mM HMF). The solid lines and dotted lines are LSVs under simulated 1 Sun illumination, and in the dark, respectively. The light illumination was from the back (glass) side.

The selectivity towards various HMF oxidation products and the durability of WO_3 was next examined *via* the continuous photo-oxidation of a 5 mM HMF electrolyte (aqueous NaP_i buffer pH 4) under simulated solar illumination using a constant applied potential of 0.68 V vs. RHE in a 2-compartment cell (working and counter electrodes separated by a Nafion membrane) in order to eliminate the possibility of reducing oxidized products at the cathode. Larger-area photoelectrodes (*ca.* 3 cm^2 *vs.* 1 cm^2) and 3 Suns equivalent illumination were used to maximize the quantity of products formed. The concentration of HMF and the formed products were monitored using HPLC. Figure 2.2A shows the evolution of the photocurrent and HMF concentration [HMF], over 64 h (data has been averaged from three independent runs). We note that the measured photocurrent was lower than expected from Figure 2.1C due to the increased substrate resistance of the larger area photoanodes.[14,15] In addition, the photocurrent decreases from an initial 0.3 to 0.1 mA cm^2 over 64 h of continuous operation due to the depletion of oxidizable substrate (at the applied potential no photocurrent from the OER was observed in the absence of HMF). Indeed [HMF] decreased to *ca.* 200 μM. In contrast, only a 12 % decrease in [HMF] was observed in a control experiment without WO_3 where the 5 mM HMF electrolyte was irradiated for 64 hours (see Figure A.4 and Table A.1). This small decease in [HMF] results from its photo-decomposition which has been reported previously.[10,16,17]

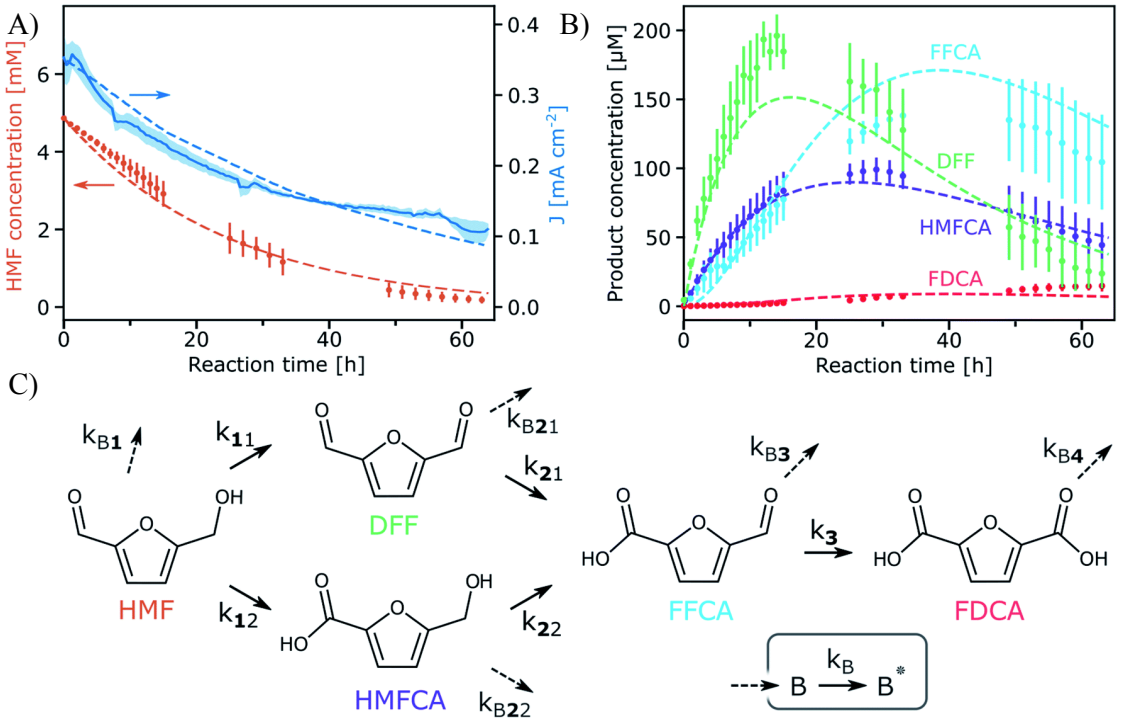

Figure 2.2: Continuous photo-oxidation of HMF with WO_3 is shown by the evolution over time of: (A) the concentration of HMF and the photocurrent; (B) the concentration of DFF, HMFCA, FFCA and FDCA; the dashed lines are the result of the chemical kinetics fitting. Data is averaged over three independent runs and the error bars represent the standard deviation. (C) Reactions pathways for the formation of FDCA from HMF and by-product reactions leading to oxidized products B and B*.

Rate constant ($\times 10^{-3}$ h^{-1})		Rate constant ($\times 10^{-3}$ h^{-1})	
k_{11}	5.54 (0.19)	k_{B1}	30.2 (0.4)
k_{12}	1.82 (0.05)	k_{B21}	43.5 (7.1)
k_{21}	64.9 (4.1)	k_{B22}	0.03 (8.4)
k_{22}	38.0 (8.5)	k_{B3}	54.5 (4.3)
k_3	7.30 (0.39)	k_{B4}	72.7 (5.9)
		$\mathbf{k}_B$	1.73 (0.27)

Table 2.1: Pseudo-first order rate constants for oxidation by WO_3 photoanode at 0.68 V vs. RHE (pH 4, 3 Sun illumination), as extracted from model fitting (see reactions Figure 2.2). Standard error from fitting the averaged experimental data in parentheses.

We note that no obvious corrosion of the WO_3 photoanode was observed *via* scanning electron microscopy during extended operation (see Figure A.5). This confirms the stability of the anode under these operation conditions. The detected products formed during the continuous photo-oxidation with WO_3 are shown in Figure 2.2B. 2,5-furandicarboxaldehyde (DFF), 5-hydroxymethyl-2-furan-carboxylic acid (HMFCA), 5-formyl-2-furancarboxylic acid (FFCA), and 2,5-furandicarboxylic acid (FDCA) are observed. It appears that DFF and FFCA are the primary products, with DFF being formed first at yields up to 4 % (based on HMF), while FFCA and finally FDCA appear later, as expected from the established oxidation pathways[18] (Figure 2.2C). While the FDCA concentration is still slightly increasing after 64 hours, its yield is quite modest (*ca.* 25 μM, 0.5 % based on HMF), and raises important questions about the reaction pathways and reaction kinetics occurring during the direct oxidation at the photoanode. Indeed, we note that the amount of consumed HMF is not equivalent to the amount of produced DFF and HMFCA. Moreover, the FDCA production rate appears smaller than the FFCA oxidation rate. This implies that side reactions involving the HMF and the other small molecules is occurring. We note that the formation of macromolecular humin by-products has been previously reported to occur with HMF oxidation.[19] Given the relatively complex reaction pathways, the limited yield of FDCA compared to the other products, and the possible production of macromolecular by-products, we next developed a model of the photo-electrochemical oxidation reactions. The set of differential equations describing the evolution of the concentration of the reactants/products and an equation for the photocurrent were solved numerically and fit with pseudo first order reaction rate constants, k's, defined in Figure 2.2C (see for full details and explanation in Appendix A). Briefly, we considered that the concentration of photogenerated holes at the WO_3 surface to be in excess, and that mass transfer from the bulk of the electrolyte to the surface of the photoanode to be similar for all components (see Figure A.6 and A.7). To obtain reasonable rate constant fitting, we accounted for the formation of unknown oxidation by-products, B, by the oxidation of the known products, and the further oxidation of these species (into B*), as shown in Figure 2.2C, which is consistent with the formation of macromolecular oxidation products. The simulated photocurrent and product concentrations from the fit model are shown as dashed lines in Figure 2.2A and 2.2B, and the obtained reaction rate constants (shown in Table 2.1) with given standard error show a high-quality fit. Moreover, these values give quantitative insight to the oxidation pathways on the WO_3 photoanode. Since the rate constant for DFF production (k_{11}) is 2.5 times larger than for HMFCA production (k_{12}), it appears that the oxidation of HMF to DFF is preferred. This result is corroborated by LSV performed with only HMF, DFF, or the diol, 2,5-bis(hydroxymethyl)furan (BHMF), which shows a

higher photocurrent for HMF or BHMF compared to DFF, implying that WO_3 reacts faster with the alcohol moiety (see Figure A.8). Furthermore, for both pathways to produce FDCA, it appears that the initial HMF oxidation is the rate limiting step as k_3, k_{21}, and k_{22} are all larger than k_{11} and k_{12}. Regarding the formation of unknown by-products, this generally occurs faster than oxidation by the known pathways. For example, the oxidation of HMF to either DFF or HMFCA is 4 times slower than the oxidation of HMF to the likely humin by-products. As an exception, the oxidation of HMFCA to FFCA occurs relatively fast (k_{22}) compared to its competing oxidation to by-product (k_{B22}). This suggests that FDCA yield may be improved by driving the reaction through the HMFCA pathway. Finally, we note that the desired FDCA product is further oxidized at the WO_3 surface (as verified by LSV, Figure A.9), and this by-product reaction appears to occur with the fastest rate constant. Thus, the low FDCA yield is in part due its quick oxidation with the photogenerated holes at the WO_3 surface. Overall, it is clear that identifying strategies to reduce the rate of the by-product reactions (*i.e.* by adding a selective surface catalyst) will be needed to further advance the direct PEC production of FDCA.

2.3 Conclusions

In summary, we demonstrate the first example of direct PEC oxidation of HMF to DFF and FDCA. The unique reactivity of WO_3, including its known poor selectivity for the OER and stability in aqueous acidic electrolyte are likely contributing factors towards its unique ability to directly photo-oxidize HMF under aqueous conditions. A maximum yield of DFF up to ca. 4 % was observed under prolonged operation, and although yields of FDCA remain modest at < 1 %, modelling the reaction kinetics suggests that increasing the rate of intermediate HMFCA production and reducing the unwanted oxidation by-products can lead to further improvements. Overall, this demonstration represents an important simplification over previous works and progresses PEC systems towards the scalable and economical production of both solar fuels and valorized biomass products—without requiring the sluggish OER.

References

[1] Lhermitte, C. R.; Plainpan, N.; Canjura, P.; Boudoire, F.; Sivula, K. Direct photoelectrochemical oxidation of hydroxymethylfurfural on tungsten trioxide photoanodes. *RSC Advances* **2021**, *11*, 198–202.

[2] Vedrine, J. C. *Metal Oxides in Heterogeneous Catalysis*; Elsevier, 2018; Google-Books-ID: xS0sDwAAQBAJ.

[3] McDonald, K. D.; Bartlett, B. M. Photocatalytic primary alcohol oxidation on WO_3 nanoplatelets. *RSC Advances* **2019**, *9*, 28688–28694.

[4] Lhermitte, C. R.; Verwer, J. G.; Bartlett, B. M. Improving the stability and selectivity for the oxygen-evolution reaction on semiconducting WO_3 photoelectrodes with a solid-state FeOOH catalyst. *Journal of Materials Chemistry A* **2016**, *4*, 2960–2968.

[5] Mi, Q.; Zhanaidarova, A.; S. Brunschwig, B.; B. Gray, H.; S. Lewis, N. A quantitative assessment of the competition between water and anion oxidation at WO_3 photoanodes in acidic aqueous electrolytes. *Energy & Environmental Science* **2012**, *5*, 5694–5700.

[6] Hill, J. C.; Choi, K.-S. Effect of Electrolytes on the Selectivity and Stability of n-type WO_3 Photoelectrodes for Use in Solar Water Oxidation. *The Journal of Physical Chemistry C* **2012**, *116*, 7612–7620.

[7] Tateno, H.; Iguchi, S.; Miseki, Y.; Sayama, K. Photo-Electrochemical CH Bond Activation of Cyclohexane Using a WO3 Photoanode and Visible Light. *Angew. Chem. Int. Ed.* **2018**, *57*, 11238–11241, _eprint: https://onlinelibrary.wiley.com/doi/pdf/10.1002/anie.201805079.

[8] Tomita, O.; Otsubo, T.; Higashi, M.; Ohtani, B.; Abe, R. Partial Oxidation of Alcohols on Visible-Light-Responsive WO3 Photocatalysts Loaded with Palladium Oxide Cocatalyst. *ACS Catalysis* **2016**, *6*, 1134–1144, Publisher: American Chemical Society.

[9] van Putten, R.-J.; van der Waal, J. C.; de Jong, E.; Rasrendra, C. B.; Heeres, H. J.; de Vries, J. G. Hydroxymethylfurfural, A Versatile Platform Chemical Made from Renewable Resources. *Chemical Reviews* **2013**, *113*, 1499–1597.

[10] Kubota, S. R.; Choi, K.-S. Electrochemical Oxidation of 5-Hydroxymethylfurfural to 2,5-Furandicarboxylic Acid (FDCA) in Acidic Media Enabling Spontaneous FDCA Separation. *ChemSusChem* **2018**, *11*, 2138–2145.

[11] Liu, W.-J.; Dang, L.; Xu, Z.; Yu, H.-Q.; Jin, S.; Huber, G. W. Electrochemical Oxidation of 5-Hydroxymethylfurfural with NiFe Layered Double Hydroxide (LDH) Nanosheet Catalysts. *ACS Catalysis* **2018**, *8*, 5533–5541.

[12] Vuyyuru, K. R.; Strasser, P. Oxidation of biomass derived 5-hydroxymethylfurfural using heterogeneous and electrochemical catalysis. *Catalysis Today* **2012**, *195*, 144–154.

[13] Cha, H. G.; Choi, K.-S. Combined biomass valorization and hydrogen production in a photoelectrochemical cell. *Nat. Chem.* **2015**, *7*, 328–333.

[14] Yao, L.; Rahmanudin, A.; Jeanbourquin, X. A.; Yu, X.; Johnson, M.; Guijarro, N.; Sekar, A.; Sivula, K. Catalyst-Free, Fast, and Tunable Synthesis for Robust Covalent Polymer Network Semiconducting Thin Films. *Adv. Funct. Mater.* **2018**, *28*, 1706303.

[15] Hernández, S.; Gerardi, G.; Bejtka, K.; Fina, A.; Russo, N. Evaluation of the charge transfer kinetics of spin-coated BiVO4 thin films for sun-driven water photoelectrolysis. *Applied Catalysis B: Environmental* **2016**, *190*, 66–74.

[16] Filiciotto, L.; Balu, A. M.; Romero, A. A.; Angelici, C.; van der Waal, J. C.; Luque, R. Reconstruction of humins formation mechanism from decomposition products: A GC-MS study based on catalytic continuous flow depolymerizations. *Molecular Catalysis* **2019**, *479*, 110564.

[17] Patil, S. K. R.; Heltzel, J.; Lund, C. R. F. Comparison of Structural Features of Humins Formed Catalytically from Glucose, Fructose, and 5-Hydroxymethylfurfuraldehyde. *Energy & Fuels* **2012**, *26*, 5281–5293.

[18] Verdeguer, P.; Merat, N.; Gaset, A. Oxydation catalytique du HMF en acide 2,5-furane dicarboxylique. *Journal of Molecular Catalysis* **1993**, *85*, 327–344.

[19] Kim, M.; Su, Y.; Fukuoka, A.; Hensen, E. J. M.; Nakajima, K. Aerobic Oxidation of 5-(Hydroxymethyl)furfural Cyclic Acetal Enables Selective Furan-2,5-dicarboxylic Acid Formation with CeO $_2$ -Supported Gold Catalyst. *Angewandte Chemie International Edition* **2018**, *57*, 8235–8239.

Chapter 3

Probing Reaction Selectivity Using Derivative Voltammetry

This chapter has been adapted from the following article: **Plainpan, N.**; P.; Boudoire, F.; Sivula, K. Derivative voltammetry: a simple tool to probe reaction selectivity in photoelectrochemical cell. Sustainable Energy & Fuels **2022**, 6, 3926–3930.[1]

3.1 Introduction

In the most commonly-used aqueous systems, an alternative oxidation reaction must compete with the OER, and enhancing the selectivity of the oxidation to the desired alternate product is an important goal. Many parameters such as solvent choice,[2] electrode material,[3] and the waveform of the applied potential[4] have been shown to influence oxidative selectivity. Among these parameters, the controlling the working potential of the anode holds a key influence.[5–10] Since the standard half-cell potential and any kinetic barriers are different for each reaction, one can expect separate reactions to proceed at different rates at a given applied potential. Hence, the applied potential can greatly affect the selectivity of the reaction. Furthermore, since Faradaic current is proportional to the rate of the redox reaction on the electrode surfaces, linear sweep voltammetry (LSV) can be used to gain some insight into the relationship between the rate of the reaction and the applied potential. In practice, the resulting voltammogram can be convoluted when multiple reactions take place on the electrode, making the interpretation of the voltammogram challenging. Performing mathematical derivation of the voltammogram with respect to the applied potential can help to resolve the current density-applied potential (J-E) curve that is convoluted from multiple

reactions.[11] The derivation can reveal buried features in the J-E curve and allows one to gain more insight into the reactions that takes place on the electrode surface at a different applied potential.[12] Derivative voltammograms (also called $\partial J/\partial E$ analysis) has been demonstrated to aid the analysis of a complex systems consisting of many redox-active substrates.[13,14] To the best of our knowledge, the $\partial J/\partial E$analysis approach has not been applied to PEC systems with photoanodes where alternative oxidation reactions are sought to be optimized over the OER, despite the added information one can obtain with no additional experimental setup requirement. In this chapter, we demonstrate that the $\partial J/\partial E$ can aid in analyzing the J-E curve for the oxidation of HMF to FDCA on WO_3 photoanode. The $\partial J/\partial E$ analysis is a simple tool to gain insight into the relationship between reaction selectivity and the applied potential.

3.2 Results and discussion

The J-E curves of a typical WO_3 photoanode in sodium phosphate buffer electrolyte (NaP_i) with and without and 5 mM HMF are shown in Figure 3.1. The J-E curve of WO_3 in both electrolytes are the same in the dark, no significant current is observed in the potential range scanned versus the reversible hydrogen electrode (RHE). With simulated solar illumination (1-Sun), the J-E curve in the HMF/NaP_i solution shows a shift in photocurrent onset potential of – 0.18 V and a higher saturated photocurrent density by 0.37 mA cm^{-2} in comparison to the J-E curve in the NaP_i electrolyte.

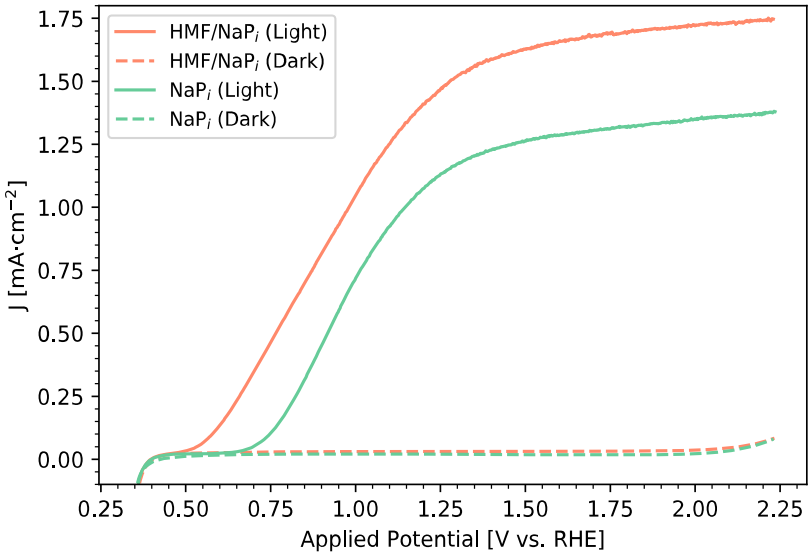

Figure 3.1: LSV of WO_3 in NaP_i and HMF/NaP_i solution with and without illumination.

The derivative of the J-E curve (with respect to the applied potential, $\partial J/\partial E$) was approximated numerically and is shown for the NaP_i electrolyte in Figure 3.2A where a single peak at + 0.95 V vs. RHE is observed. In contrast, the $\partial J/\partial E$ curve of the photoanode in HMF/NaP_i electrolyte (Figure 3.2B) shows a broad, two-humped peak from approximately + 0.65 to + 0.95 V vs. RHE. To gain more insight into the obtained derivative voltammogram, we fit the derivative photocurrent to a mathematical model as described in the Appendix B. In brief, the model takes a basis from Gericher's equation with a Gaussian density of states and accounts for the increasing photocurrent in the plateau region of the J-E curve due to the additional band-bending at higher applied potentials, which drives additional carriers to the semiconductor liquid junction in low-carrier-mobility semiconductors like oxides.[15] The model fitting parameters are shown in Table B.1 in the Appendix B and graphically the fit reveals one peak at + 0.96 V vs. RHE in the NaP_i electrolyte case (red line in Figure 3.2A). For the HMF/NaP_i electrolyte, the best fit (red line in Figure 3.2B) shows two peaks at + 0.66 V vs. RHE ($\partial J/\partial E$-peak 1) and + 0.96 V vs. RHE ($\partial J/\partial E$-peak 2). The attempt to fit the $\partial J/\partial E$ of the HMF/NaP_i electrolyte with only one fitting curve does not yield a good fit (see Figure B.1). We suggest that each peak in the derivative voltammogram corresponds to a different reaction taking place on the electrode surface, thus there is at least one reaction taking place in the NaP_i electrolyte while for the HMF/NaP_i solution there are at least two reactions. Since the peak at + 0.66 V vs. RHE is only found when HMF is present in the system. We, therefore, assign this peak to the oxidation of HMF. Since the peak at + 0.96 V vs. RHE is found in both cases, it is reasonable to assign this to the water oxidation reaction.

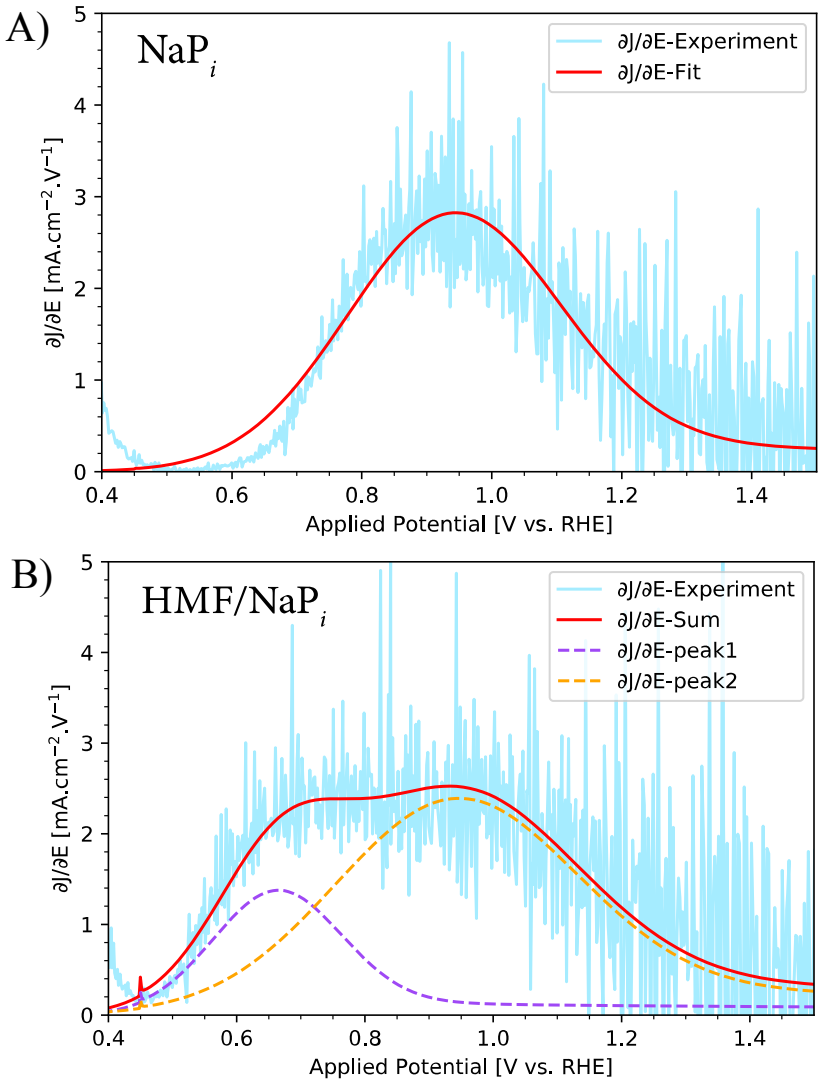

Figure 3.2: The $\partial J/\partial E$ analysis of WO_3 in (A) NaP_i electrolyte and (B) HMF/NaP_i solution.

Numerical integration of the mathematical fit of the $\partial J/\partial E$ yields a simulated J-E curve. The simulated J-E curves in the NaP_i electrolyte and the HMF/NaP_i solution are depicted in Figure 3.3A and Figure 3.3B, respectively, in comparison to the experimental data. The simulated J-E curves (red solid line) match the experimental value (blue solid line) well in both cases. As our observation that the $\partial J/\partial E$-peak 1 and $\partial J/\partial E$-peak 2 in the $\partial J/\partial E$ analysis of the HMF/NaP_i solution are correlated with the oxidation of HMF and water, respectively, we propose that the numerical integration of these two peaks (J_{sim}-peak 1 and J_{sim}-peak 2) are the decoupled photocurrent densities associated with HMF oxidation and water oxidation, respectively. These decoupled J-E curves are also shown in Figure 3.3B. We can see that the ratio of the photogenerated charges going to either HMF oxidation or water oxidation is dependent on the applied potential. With the information on this deconstructed photocurrent, we can predict the selectivity for HMF oxidation

as the function of the applied potential from Equation A.1

$$Selectivity_{\,HMF\ oxidation} = \frac{J_{sim}\text{-}peak\ 1}{J_{sim}\text{-}sum} \times 100\% \tag{3.1}$$

Where J_{sim}-Sum represents the sum of the two decoupled J-E curves. We tested this prediction by performing photoelectrolysis of HMF at + 0.65 V, 0.85 V and 1.20 V vs. RHE. The concentration of HMF (as measured by high performance liquid chromatography) as a function of the passed charge is shown in Figure 3.3C. The oxidation of HMF to FDCA is a multistep reaction with each of the steps proceeding through a two-electron oxidation (see Figure 1.4). Therefore, we calculate the selectivity for HMF oxidation based on the assumption that HMF undergoes a two-electron oxidation. Moreover, since the presence of HMF affects the $\partial J/\partial E$ analysis and the concentration of HMF drops with an increasing passed charge, the estimation of selectivity from the data in Figure 3.3C was performed using the initial rate of HMF consumption during an extended photo electrolysis (i.e., by considering the initial time points from each of the runs) to ensure minimal deviation from the condition used to perform the $\partial J/\partial E$ analysis. The extrapolated initial rate of HMF consumption for the different potentials is shown as the broken lines in Figure 3.3C. The predicted selectivity (calculated from Equation A.1) and the experimental values (obtained from the HMF consumption rate are compared in Figure 3.3D and Table 3.1. The prediction is very accurate at the low applied potential (+0.65 V vs. RHE) but deviates from the experimental values at the higher applied potentials (+0.85 and 1.20 V vs. RHE). We attribute this deviation to the mathematical foundation of the $\partial J/\partial E$ analysis which based purely on thermodynamics. At the high applied bias, if the kinetics of water oxidation were faster than that of HMF oxidation we would expect the observed deviation. It has been shown in the literature that water oxidation on WO_3 proceeds through the formation of peroxo species. In addition, the oxidation of anionic electrolytes has also been observed.[16,17] The kinetics of these reactions may be faster than HMF oxidation. Alternatively, the difference in the predicted and the experimental-determined selectivity could be the result of mass transport limitations. The number of available photogenerated holes is higher at the more positive applied potential. If there are not enough HMF molecules to react with, the excess holes may react with other species in the solution, resulting in a lower selectivity. We addressed this possibility by performing photoelectrolysis of HMF at a higher initial HMF concentration of 100 mM at 0.65 V and 1.20 V vs. RHE (see Figure B.2). We found that the selectivity is lower at 1.2 V vs. RHE than at 0.65 V vs. RHE in both initial concentrations. This suggests that the decrease in the selectivity is not due to mass transport limitations.

Provided with an ability to probe the relationship between the applied potential and the

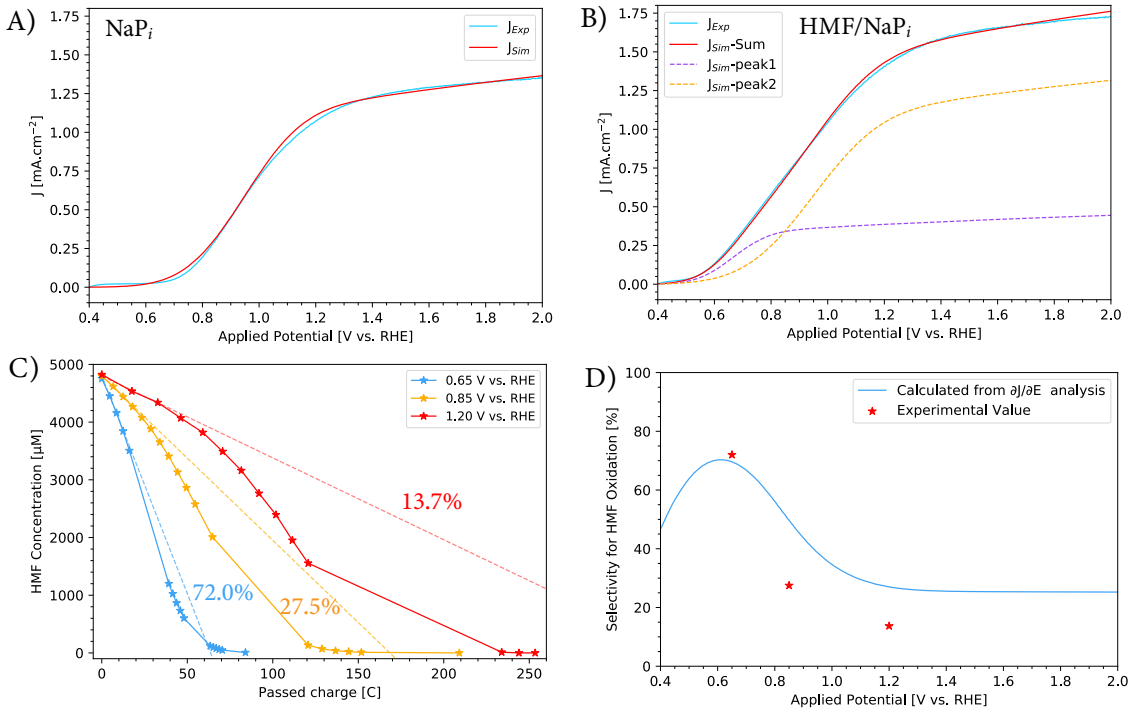

Figure 3.3: Experimental and simulated photocurrent in (A) NaP$_i$ electrolyte and in (B) HMF/NaP$_i$ solution. (C) The concentration of HMF as a function of passed charge at 0.65 V, 0.85 V and 1.20 V vs. RHE with the fitted selectivity for HMF oxidation. (D) Predicted and the experimental-determined selectivity for HMF oxidation at different applied potential

selectivity of the reaction demonstrated earlier, we next aimed to describe and provide the physical meaning of the peaks in the derivative voltammogram. Chemical reactions on photoelectrodes utilize the photoexcited minority charge carriers to perform redox reactions. The minority charge carriers are photogenerated holes and photogenerated electrons for n-type and p-type semiconductors, respectively. Typically, the photogenerated holes and photogenerated electrons are energetically localized at the valence band edge and conduction band edge, respectively. Nevertheless, some electronic states with energy levels that lie within the bandgap of semiconductors can be present. These electronics states can have diverse origins ranging from any features that break the symmetry of the bulk semiconductors such as vacancies and dangling bonds to the chemical states between the semiconductor surface and the chemical species in the electrolyte. These latter electronics states are known as surface states.[18,19] The minority charge carriers can accumulate within the surface states and then react with the redox-active species in the electrolyte, hence performing the redox reaction. Alternatively, the accumulated charge carriers can also recombine with the majority charge carriers. The surface states that promote the reactions are known as an intermediate surface state (i-SS) and the ones that promote recombination are called recombining surface state (r-SS).[18]

One probable physical meaning of the derivative voltammogram was proposed by Can Li and

Applied Potential (V vs. RHE)	**Selectivity for HMF oxidation (%)**	
	Experimental	**Predicted**
0.65	72.0	68.2
0.85	27.5	47.7
1.20	13.7	28.8

Table 3.1: Predicted and the experimental-determined selectivity for HMF oxidation

co-workers.[20] The researchers proposed that the derivative voltammogram is proportional to the density of intermediate states on the surface of semiconductors as a function of the applied potential (DOS(E)). Using a set of surface modified hematite photoanodes and comparing the DOS(E) as probed by the derivative voltammogram to electrochemical impedance spectroscopy (EIS) and fast cyclic voltammetry (the common methods for detecting intermediate states), the authors found a similar trend, which supported their view.[20]

To verify if this postulation applies to our system, we first investigate the DOS(E) in our system by EIS (See Figure B.3 and B.4 for the Nyquist and Bode plot and the results of the fitting to the circuit model in Figure 3.4). For EIS, the accumulation of charge in the surface states is assumed to contribute to the surface capacitance (C_{SS}) with the relationship $C_{SS} = q \times DOS(E)$, where q is the electron charge.[21] The analysis of the WO_3 photoanode with and without HMF in the electrolyte show very similar results with one surface capacitive (C_{SS}) peak at + 0.95 V vs. RHE with relatively the same magnitude. The capacitance greatly increases at applied potentials below + 0.6 V vs. RHE (see Figure B.5 C_{SS}). When comparing the DOS(E) as found by EIS to the $\partial J/\partial E$, we found the DOS(E) peak observed by EIS overlaps well with the $\partial J/\partial E$-peak 2 (Figure B.6). This supports the view that the $\partial J/\partial E$-peak 2 can represent the distribution of the intermediate states (i-SS) which are associated with water oxidation on WO_3. As for the $\partial J/\partial E$-peak 1, since the EIS analysis does not show any surface states around + 0.60 V vs. RHE, we cannot directly link the $\partial J/\partial E$-peak 1 to the intermediate states. This demonstrates that the $\partial J/\partial E$ analysis can give additional and complimentary information to EIS.

Regarding the origin of the $\partial J/\partial E$-peak 1, it may come from a short-lived i-SS or an i-SS that does not involve charge accumulation at the surface. Since probing EIS relies on the charge accumulation at the steady-state, such i-SSs may not be detectable by EIS. Heidary and co-workers studied the interaction between HMF and NiOOH thin film using surface-enhanced Raman spectroscopy and found that HMF can be adsorbed onto the surface of NiOOH.[22]The interaction was found to be a non-covalent bond, as the team only observed a slight shift in the Raman signal.

It is thus reasonable to think that HMF may have certain non-covalent interactions with WO_3, and this adsorbed HMF may be the i-SS that is responsible for $\partial J/\partial E$-peak 1. Nevertheless, we cannot discount the possibility of an outer sphere charge transfer mechanism between HMF and WO_3 where HMF directly inject electrons into WO_3 without being adsorbed onto the WO_3 surface.

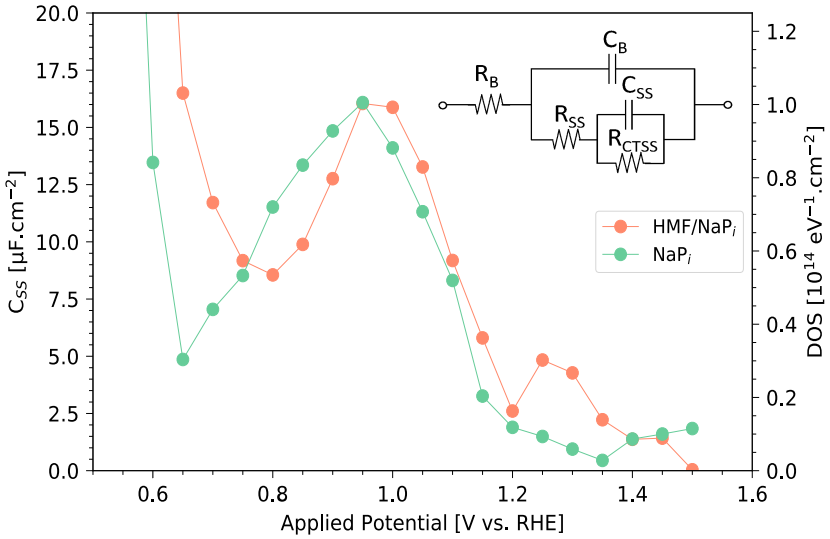

Figure 3.4: DOS(E) as probed by EIS analysis of WO_3 in NaP$_i$ electrolyte and HMF/NaP$_i$ solution

3.3 Conclusions

We demonstrated the use of an $\partial J/\partial E$ analysis of linear scanning voltammograms from a photoanode in a system with competing oxidation reactions in predicting selectivity. We applied this analysis to study the selectivity between HMF oxidation and water oxidation on WO_3 photoanode and found that the $\partial J/\partial E$ analysis can predict the selectivity trend of HMF oxidation over the OER. The prediction is accurate at low applied potential and showed a deviation from the experimental value at the higher applied potential. We attributed this deviation to the kinetics of the reaction that should have a more profound effect at the higher bias. By comparing the $\partial J/\partial E$ curves to EIS analysis, we conclude that $\partial J/\partial E$ provides additional information that helps to give insight about the nature of surface states. Overall, we believe that this method could be used to give a quick estimation of the selectivity of the reaction as the function of applied potential for other photoelectrosynthesis systems.

References

[1] Plainpan, N.; Boudoire, F.; Sivula, K. Derivative voltammetry: a simple tool to probe reaction selectivity in photoelectrochemical cells. *Sustainable Energy & Fuels* **2022**, *6*, 3926–3930.

[2] Zhang, L.; Hu, X. Nickel catalysis enables convergent paired electrolysis for direct arylation of benzylic C–H bonds. *Chemical Science* **2020**, *11*, 10786–10791.

[3] Chadderdon, D. J.; Xin, L.; Qi, J.; Qiu, Y.; Krishna, P.; More, K. L.; Li, W. Electrocatalytic oxidation of 5-hydroxymethylfurfural to 2,5-furandicarboxylic acid on supported Au and Pd bimetallic nanoparticles. *Green Chem.* **2014**, *16*, 3778–3786.

[4] Wills, A. G.; Poole, D. L.; Alder, C. M.; Reid, M. A Mechanistic and Cautionary Case Study on the Use of Alternating Potential in Electrochemical Reactions. *ChemElectroChem* **2020**, *7*, 2771–2776.

[5] Rosatella, A. A.; Simeonov, S. P.; Frade, R. F. M.; Afonso, C. A. M. 5-Hydroxymethylfurfural (HMF) as a building block platform: Biological properties, synthesis and synthetic applications. *Green Chemistry* **2011**, *13*, 754.

[6] Kuster, B. F. M. 5-Hydroxymethylfurfural (HMF). A Review Focussing on its Manufacture. *Starch - Stärke* **1990**, *42*, 314–321.

[7] Wang, F.; Stahl, S. S. Merging Photochemistry with Electrochemistry: Functional-Group Tolerant Electrochemical Amination of C(sp ^{3})H Bonds. *Angewandte Chemie International Edition* **2019**, *58*, 6385–6390.

[8] Huang, H.; Lambert, T. H. Electrophotocatalytic Acetoxyhydroxylation of Aryl Olefins. *Journal of the American Chemical Society* **2021**, *143*, 7247–7252.

[9] Shen, T.; Lambert, T. H. C–H Amination via Electrophotocatalytic Ritter-type Reaction. *Journal of the American Chemical Society* **2021**, *143*, 8597–8602.

[10] Ren, D.; Fong, J.; Yeo, B. S. The effects of currents and potentials on the selectivities of copper toward carbon dioxide electroreduction. *Nature Communications* **2018**, *9*, 925.

[11] Perone, S. P.; Mueller, T. R. Application of Derivative Techniques to Stationary Electrode Polarography. *Analytical Chemistry* **1965**, *37*, 2–9.

[12] Murthy, A.; Manthiram, A. Application of Derivative Voltammetry in the Analysis of Methanol Oxidation Reaction. *The Journal of Physical Chemistry C* **2012**, *116*, 3827–3832.

[13] Gonzalez, A.; Vidal, S.; Ugliano, M. Untargeted voltammetric approaches for characterization of oxidation patterns in white wines. *Food Chemistry* **2018**, *269*, 1–8.

[14] Ugliano, M.; Slaghenaufi, D.; Picariello, L.; Olivieri, G. Oxygen and SO $_2$ Consumption of Different Enological Tannins in Relationship to Their Chemical and Electrochemical Characteristics. *Journal of Agricultural and Food Chemistry* **2020**, *68*, 13418–13425.

[15] Cendula, P.; Tilley, S. D.; Gimenez, S.; Bisquert, J.; Schmid, M.; Grätzel, M.; Schumacher, J. O. Calculation of the Energy Band Diagram of a Photoelectrochemical Water Splitting Cell. *The Journal of Physical Chemistry C* **2014**, *118*, 29599–29607.

[16] Mi, Q.; Zhanaidarova, A.; S. Brunschwig, B.; B. Gray, H.; S. Lewis, N. A quantitative assessment of the competition between water and anion oxidation at WO_3 photoanodes in acidic aqueous electrolytes. *Energy & Environmental Science* **2012**, *5*, 5694–5700.

[17] Hill, J. C.; Choi, K.-S. Effect of Electrolytes on the Selectivity and Stability of n-type WO_3 Photoelectrodes for Use in Solar Water Oxidation. *The Journal of Physical Chemistry C* **2012**, *116*, 7612–7620.

[18] George, K.; Khachatrjan, T.; van Berkel, M.; Sinha, V.; Bieberle-Hütter, A. Understanding the Impact of Different Types of Surface States on Photoelectrochemical Water Oxidation: A Microkinetic Modeling Approach. *ACS Catalysis* **2020**, *10*, 14649–14660.

[19] Tang, P.; Arbiol, J. Engineering surface states of hematite based photoanodes for boosting photoelectrochemical water splitting. *Nanoscale Horizons* **2019**, *4*, 1256–1276.

[20] Wang, Z.; Fan, F.; Wang, S.; Ding, C.; Zhao, Y.; Li, C. Bridging surface states and current–potential response over hematite-based photoelectrochemical water oxidation. *RSC Advances* **2016**, *6*, 85582–85586.

[21] Liu, Y.; Formal, F. L.; Boudoire, F.; Yao, L.; Sivula, K.; Guijarro, N. Insights into the interfacial carrier behaviour of copper ferrite ($CuFe_2O_4$) photoanodes for solar water oxidation. *Journal of Materials Chemistry A* **2019**, *7*, 1669–1677.

[22] Heidary, N.; Kornienko, N. Electrochemical biomass valorization on gold-metal oxide nanoscale heterojunctions enables investigation of both catalyst and reaction dynamics with *operando* surface-enhanced Raman spectroscopy. *Chemical Science* **2020**, *11*, 1798–1806.

Chapter 4

Strategies to Improve FDCA Yield

4.1 Introduction

We have demonstrated in chapter 2 that the illuminated surface of WO_3 can oxidize HMF to FDCA, but the yield of the reaction is very modest. The majority of HMF undergoes a degradation reaction, resulting in many unidentifiable products. In chapter 3, we show that the applied potential has a great impact on the selectivity between HMF oxidation and the water oxidation reactions. Nevertheless, the FDCA yield remains unchanged regardless of the applied potential. In this chapter, various strategies to improve FDCA yield will be discussed. Different initial HMF concentrations and the applied potentials to perform photoelectrolysis of HMF are employed due to the limitation in the stability of the modified electrodes made with different strategies. For the sake of comparison, we will regard any modification that ultimately leads to FDCA yield of lower than 1 % as not significant in comparison to that of the bare WO_3 electrode.

4.2 Results and discussion

4.2.1 MnO_x

A plethora of heterogeneous electrocatalysts for HMF oxidation to FDCA have been shown in the literature in the past few years. Many of these catalysts have achieved an FDCA yield of more than 90 % with good stability.[1–5] Nevertheless, almost all of these electrocatalysts are metal oxides which are stable only in basic conditions. Therefore, many of the reported electrocatalysts cannot be used with WO_3 due to the pH mismatch. Only a few electrocatalysts for HMF oxidation have been reported to function in acidic media. One of the most interesting ones is MnO_x. Kubota

and co-workers reported the use of MnO_x as an electrocatalyst for HMF oxidation in pH 1 H_2SO_4 solution. The team found that the MnO_x gives a modest FDCA yield of 53.8 %.[6] With this potential to improve FDCA yield and compatible pH range with WO_3, we decided to apply MnO_x onto WO_3 in order to improve the FDCA yield.

The amount of MnO_x to be deposited onto WO_3 was optimized first. The deposition of MnO_x was performed by photoelectrodeposition. The amount of the deposited MnO_x was controlled by the amount of the charge passed during the photoelectrodeposition. The resulting MnO_x/WO_3 electrodes were first assessed by LSV. The chopped-light linear sweep voltammograms are shown in Figure 4.1. The voltammograms illustrate that the photocurrent drops with an increasing amount of photoelectrodeposited MnO_x. We hypothesized two explanations for the phenomenon: The deposited MnO_x progressively covers more surface of WO_3 with an increasing amount of photoelectrodeposited MnO_x, preventing WO_3 from directly oxidizing water and HMF. Since MnO_x is not a good catalyst for OER[7], the current is reduced but the selectivity for HMF oxidation may have improved. Alternatively, MnO_x may act as a recombination center. The reduction in the photocurrent is a result of the recombination loss at the surface of WO_3.

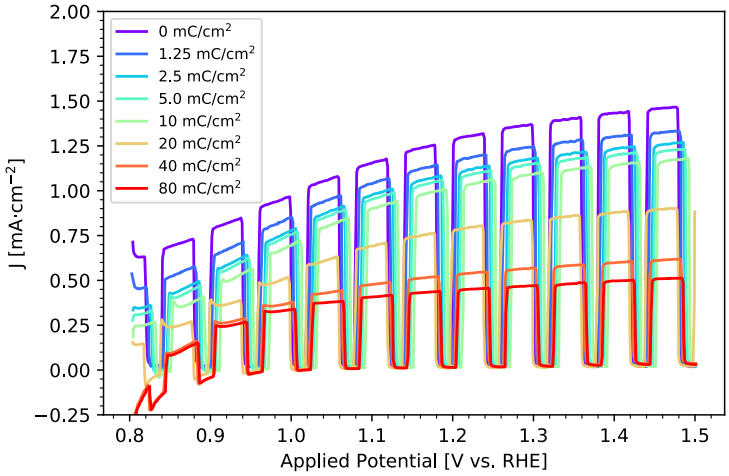

Figure 4.1: Chopped-light linear sweep voltammogram of the MnO_x/WO_3 electrode with different amount of passed charge for photoelectrodepositted MnO_x.The voltammogram was recorded in 5 mM HMF solution under 1 sun illumination.

To verify the proposed hypotheses, we performed extended photoelectrolysis of HMF using MnO_x/WO_3 as a working electrode. The detail for the fabrication and the characterization of this MnO_x/WO_3 working electrode is discussed in the Appendix C. The photoelectrolysis was performed at 1.50 V vs. RHE in 0.1 M H_2SO_4 solution. We decided to keep the condition as close to what was reported by Kubota and co-workers.[6] We note that the applied potential will be different from what was reported by Kubota and co-workers as there is an added photopotential from WO_3 in our

case, resulting in our actual applied potential to be higher than 1.50 V vs. RHE. Nevertheless, this preliminary photoelectrolysis aims to investigate whether or not MnO_x can improve the FDCA yield. The evolution of HMF, the intermediates (DFF, HMFCA and FFCA; these three compounds will be referred to as the intermediates hereafter) and FDCA are shown in Figure 4.2. The evolution of the intermediates and FDCA are very low (with a yield of roughly 0.1 %) despite a majority of HMF being consumed. The low evolution of the intermediates and FDCA found here is similar to that observed when WO_3 is used as a working electrode (Figure 2.2). As the deposition of MnO_x on WO_3 reduces the photocurrent without improving FDCA yield, we believe that MnO_x acts as a recombination center and hence, cannot be used with WO_3.

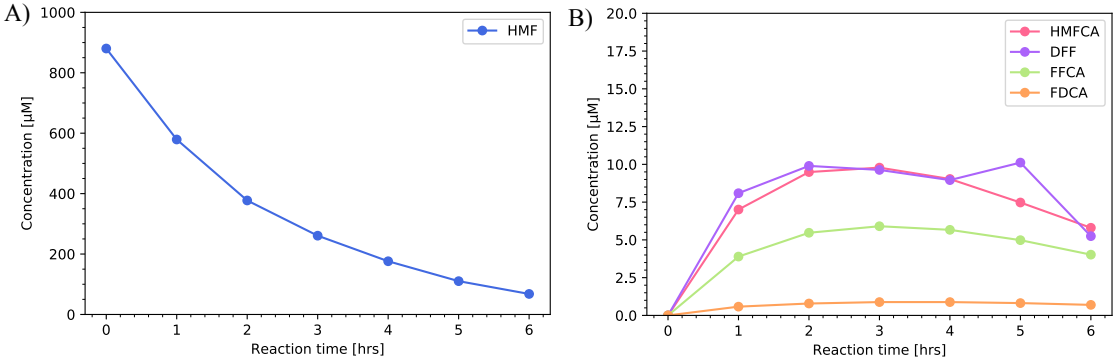

Figure 4.2: The evolution of of A) HMF and B) the intermediates (HMFCA, DFF and FFCA) and the product (FDCA) as a function of reaction time from the photoelectrolysis of HMF using the MnO_x/WO_3 as a working electrode. The photoelectrolysis was performed at 1 sun illumination and at the constant applied potential of 1.50 V vs. RHE. The supporting electrolyte was 0.1 M H_2SO_4 at pH 1.

4.2.2 TEMPO

2,2,6,6-Tetramethylpiperidin-1-yl)oxyl (TEMPO) has been shown in literature as an efficient electrocatalyst for alcohol and aldehyde oxidation.[8–11] As mentioned in chapter 1, Cha and co-workers have demonstrated the use of TEMPO as a redox mediator for HMF oxidation to FDCA, using $BiVO_4$ as a photoanode with a very high FDCA yield of 99 %.[12] Therefore, TEMPO is an interesting electrocatalyst for HMF oxidation, but immobilization to the electrode surface is required to reduce the amount of TEMPO needed. Due to its versatility in performing alcohol and aldehyde oxidation, TEMPO has been modified with various supports.[13] Nevertheless, almost all of the immobilization strategies shown in the literature involve covalent modification. The structure of TEMPO is modified with a linker group, before being covalently attached to a support such as magnetic nanoparticles[14,15], carbon nanotubes[16], fullerene[17–20], graphene oxide[21] or polymers[22–24]. Despite great success in immobilization of TEMPO to various supports via covalent modification, employing this strategy with WO_3 may result in poor electrode stability. As shown in chapter 2,

WO_3 can degrade HMF into various unidentifiable products. Organic linkers can be prone to oxidative degradation in the same manner. If the linker is destroyed, the TEMPO molecule will leach into the solution. Therefore, non-covalent modification is preferred in our system. Belgsir and co-workers demonstrated the non-covalent immobilization technique using Nafion® film. The team immobilized TEMPO by mixing TEMPO with Nafion® polymer solution, before casting it onto a graphite felt electrode. The modified electrode was shown to have activity toward the oxidation of the alcohol moiety on carbohydrates to give the respective carboxylic acids.[25] Given this promising strategy, we applied this technique to our system.

To assess the stability of the modified electrodes, the fabrication method was first optimized on an FTO substrate. TEMPO was mixed with a commercial 5 wt % Nafion® solution in a mixture of lower aliphatic alcohols and water to give a precursor solution with a concentration of 25 and 500 mg/mL. The precursor solutions were deposited onto an FTO substrate by drop casting, doctor blading, spin coating and spray coating (only the precursor concentration of 25 mg/mL was used for spray coating). Photographs of the fabricated electrodes are shown in Figure 4.3. The modified electrode will be referred to with the method used in the fabrication and the concentration of the precursor solution used in the fabrication e.g. the film fabricated by spin coating with the precursor solution of 500 mg/mL will be referred to as the spin coating-500 electrode. Homogeneous films (both translucent and transparent) are preferable as an inhomogeneous film can result in non-reproducibility in the performance of the electrode. The drop casting-25, drop casting-500 and doctor blading-500 are non-homogeneous. Spray coating results in a more homogeneous and translucent film. The films from the spin coating technique are homogeneous and transparent.

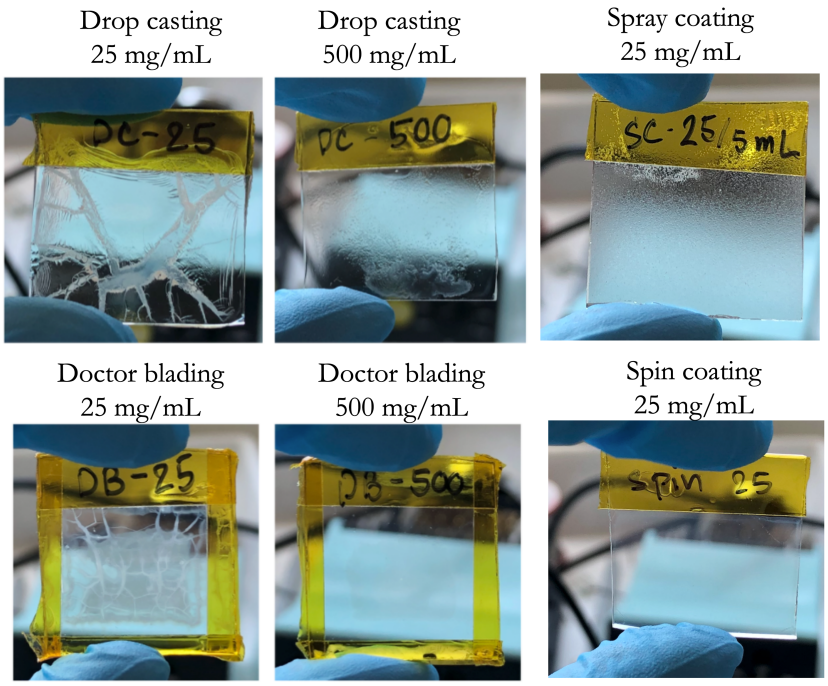

Figure 4.3: Photographs of TEMPO/Nafion® modified electrodes fabricated by drop casting, spray coating, doctor blading and spin coating using the precursor solution concentration of 25 and 500 mg/mL. The modified electrode fabricated from spin coating method with the precursor concentration of 25 and 500 mg/mL have similar appearance. Only the film fabricated with the precursor concentration of 25 mg/ml is shown here.

In a catalytic cycle, TEMPO is first oxidized to the oxoammonium ion (OXO) which is the active species for alcohol and aldehyde oxidation. The oxo ion then oxidizes alcohols or aldehydes and in turns, being reduced back to TEMPO (Figure 4.4).[26] During photoelectrolysis, the TEMPO/Nafion® modified electrodes have to go through many of catalytic cycles. Cyclic voltammetry can be used to simulate this process and hence can be used to probe the stability of the fabricated electrode.

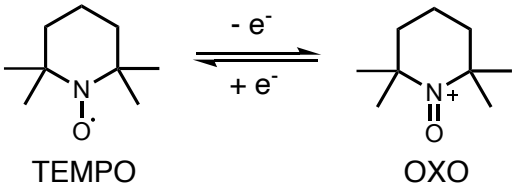

Figure 4.4: Electron transfer reaction of TEMPO[26]

The CV was repeated for 50 scans. The cyclic voltammograms of the fabricated films are shown in Figure C.2 - C.8. The cyclic voltammograms show reversible oxidation with an anodic peak potential (E_{pa}) and a cathodic peak potential (E_{pc}) of 1.5 and 0.9 V vs. RHE respectively. The E_{pa} corresponds to the oxidation of TEMPO to OXO and the E_{pc} corresponds to the reduction of

OXO back to TEMPO. To better visualize the effect of the fabrication conditions on the stability of the resulting modified electrodes, the anodic peak current (i_{pa}) of each scan was extracted and plotted against the cycle number (CN). We will refer to this plot as i_{pa}-CN plot hereafter. The i_{pa}-CN plot illustrates the evolution of i_{pa} as a function of cycle number, allowing one to track the stability of the modified electrodes. The i_{pa}-CN plot from the stability test of the TEMPO/Nafion® modified electrodes are shown in Figure 4.5. The i_{pa} of the doctor blading-25, spin coating-25 and spin coating-500 electrodes are very low. We suspected that the low i_{pa} is the result of the TEMPO/Nafion® film being too thin in the case of spin coating (both the spin coating-25 and spin coating-500 electrodes). For the doctor blading-25 electrode, the low i_{pa} is due to the low catalyst loading in the film since the i_{pa} of the doctor blading-500 electrode is significantly higher. The spray coating-25, drop casting-25, drop casting-500 and doctor blading-500 electrodes experience a drop in i_{pa} with an increasing cycle number. The drop casting-25 electrode shows a peculiar behavior in which the i_{pa} increases and plateaus from the cycle number 5-15, before showing a steady decline. The i_{pa} at the plateau is also the highest i_{pa} of all tested TEMPO/Nafion® modified electrodes. This peculiar behavior may have been the result of the film thickness and the rough morphology. The electrolyte may not fully penetrate through all of the Nafion® film in the first few potential cycles. As the electrolyte penetrates through the Nafion® film, more immobilized TEMPO is in contact with the electrolyte, and thus the film becomes more redox-active. Hence, the sharp increase of the i_{pa} in the first few potential cycling steps. The decline in the i_{pa} shows the instability of the electrodes. Two hypotheses were made to explain this decline. The immobilized TEMPO can slowly leach out into the electrolyte. Although the leached TEMPO in the electrolyte can still participate in the redox reaction, the dissolution will result in a decrease in the concentration of TEMPO near the electrode surface. Hence, decreasing the i_{pa}. Alternatively, TEMPO can be degraded due to the potential cycling. The degradation of TEMPO is likely to result in many degraded products, some of which would be redox-active. Should this be the case, many new oxidation or reduction peaks from these redox-active degraded products would have appeared in the cyclic voltammogram. As the emergence of a new peak was not observed, leaching of TEMPO into the electrolyte is the more probable explanation for the instability of the TEMPO/Nafion® modified electrodes. To further confirm the hypothesis on the leaching of TEMPO, the electrolyte was replaced after CV 50 scans with a fresh electrolyte before another run of CV was performed. The cyclic voltammograms before and after changing the solution are shown in Figure C.9 - C.15. The i_{pa} of the cyclic voltammogram in the fresh electrolyte is smaller in all of the electrodes tested which confirms the leaching of TEMPO into the electrolyte.

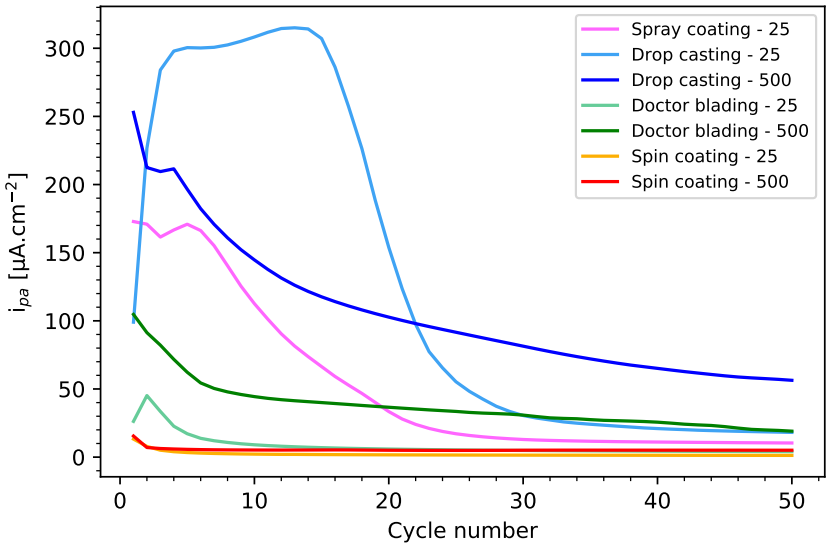

Figure 4.5: i_{pa}-CN plot of the TEMPO/Nafion® modified electrode prepared with various fabrication techniques and precursor concentrations.

Considering the i_{pa} of all of the tested electrodes, the drop casting-500 electrode retains the highest i_{pa} after 50 cycles (Figure 4.5). In addition to this, the i_{pa} in the fresh electrolyte of the drop cast-500 electrode (Figure C.16) is also the highest, suggesting that the drop cast-500 electrode retains the highest amount of TEMPO after 50 potential cyclings. Some immobilized TEMPO that may be not well anchored to the substrate may leach out in the initial potential cycling. Once these loosely bounded TEMPO has completely leached out, the decline in the i_{pa} may stop. The drop casting-500 electrode may be in the process of reaching the plateau. To test this hypothesis, another drop casting-500 electrode was fabricated and the potential cycling was repeated for 350 cycles. The drop casting-500 electrode may show the stability of i_{pa} if enough potential cycle has been achieved. The cyclic voltammogram of the extended stability test is shown in Figure C.17 and the i_{pa}-CN plot in shown in Figure 4.6.

The i_{pa} of the drop casting-500 electrode in Figure 4.6 increases sharply in the first few cycle number. The i_{pa} reaches the maximum on the 8^{th} cycle at 92 μA.cm^{-2} before it declines steadily with increasing cycle number. The i_{pa} does not show any sign of reaching the plateau and the i_{pa} after 350 potential cycling is very low (approximately 5 μA.cm^{-2}). The immobilized TEMPO is likely to keep leaching out and the i_{pa} is unlikely to reach the plateau. In addition to this, the i_{pa} of the drop casting-500 electrode in Figure 4.5 and Figure 4.6 are also significantly different in magnitude, despite the same fabrication technique and condition used in the fabrication of the two electrodes. This comparison illustrates the poor reproducibility of the films fabricated by the drop casting technique, likely due to the film inhomogeneity.

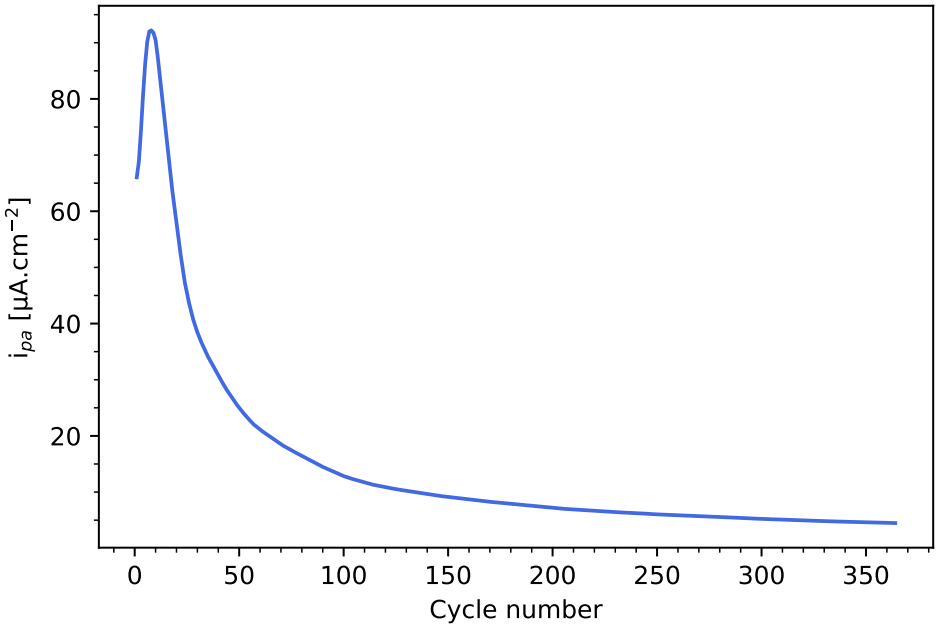

Figure 4.6: i_{pa}-CN plot of the extended stability test of the drop casting-500 electrode

To tackle the dissolution of TEMPO, 4-Hydroxy-TEMPO benzoate (Figure 4.7), the less water-soluble derivative of TEMPO was used. This molecule will be referred to as TemBen hereafter. Modified electrodes from TemBen/Nafion® were fabricated. To avoid the film inhomogeneity, the spin coating was used exclusively for the fabrication of TemBen/Nafion® modified electrodes. The solubility of TemBen in the commercial Nafion® precursor solution is also lower than that of TEMPO. The preliminary solubility test was conducted and suggests that the maximum solubility of TemBen in the commercial Nafion® precursor solution is approximately 166 mg/mL. Nevertheless, when a higher concentration of TemBen in the precursor solution is used, the fabricated films tend to be non-homogeneous. As a result, the lower TemBen concentration of 50 mg/mL was chosen for the film fabrication step. The TemBen/Nafion® films were fabricated by spin coating on FTO with a rotational speed of 500, 1000, 1500, 2000, 2500 and 3000 rpm. These electrodes will be referred to by the speed used in the spin coating (e.g. the electrode that was fabricated using the spin coating speed of 500 rpm will be referred to as the 500 rpm electrode) hereafter. The cyclic voltammogram of TemBen (Figure C.18 - C.21) is similar to that of TEMPO with the E_{pa} and E_{pc} also appearing at 1.5 and 0.9 V vs. RHE respectively. The electrode stability will be assessed by cyclic voltammetry. The i_{pa}-CN plot of the stability test of the TemBen/Nafion® modified electrodes of various fabrication conditions is shown in Figure 4.8A.

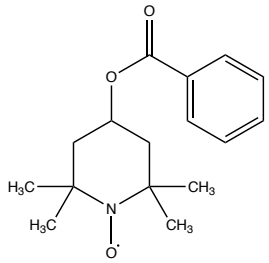

Figure 4.7: Structure of 4-Hydroxy-TEMPO benzoate (TemBen)

The i_{pa} of all of the electrodes are very low (< 10 μA.cm^{-2}) which could be the result of the catalyst layer being too thin. The i_{pa} of all of the electrodes show an initial drop in the first few cycles before slowly increasing. We believe that the initial drop in the i_{pa} is due to the oxidation of the contamination at the surface of the electrodes. The current from the oxidation of the contamination is pronounced here as the current from the oxidation of the immobilized TemBen in these sets of electrodes is very low. The later increase of i_{pa} may be explained by the gradual penetration of the electrolyte into the Nafion® layer discussed earlier. The i_{pa} of all of the electrodes tested show minimal differences in magnitude from one another. The small difference suggests that the spin speed has a small impact on the performance of the modified electrode. Despite the low i_{pa}, all of the modified electrodes show good stability in the first 50 scans as the i_{pa} do not show signs of decline as found in TEMPO/Nafion® modified electrode (Figure 4.5). To further investigate the stability of the modified electrodes, another 500 rpm electrode was fabricated and subjected to the extended stability test. Since all of the electrodes show very similar i_{pa} after 50 scans, any of the electrodes could have been chosen for the extended stability test. The cyclic voltammograms of the extended stability test are shown in Figure C.22 and the i_{pa}-CN is shown in Figure 4.8B. The i_{pa} in the extended stability test follows the same trend as observed in the 500 rpm electrode in Figure 4.8A with the initial drop in the first few cycles before slowly increasing with increasing cycle number. The i_{pa} reached the maximum of 3.4 μA.cm^{-2} at the 70^{th} cycle before declining. The i_{pa} declines back to the level after an initial drop of 1.6 μA.cm^{-2} after 130 cycles. The decline of the i_{pa} shows the instability of the TemBen/Nafion® modified electrodes.

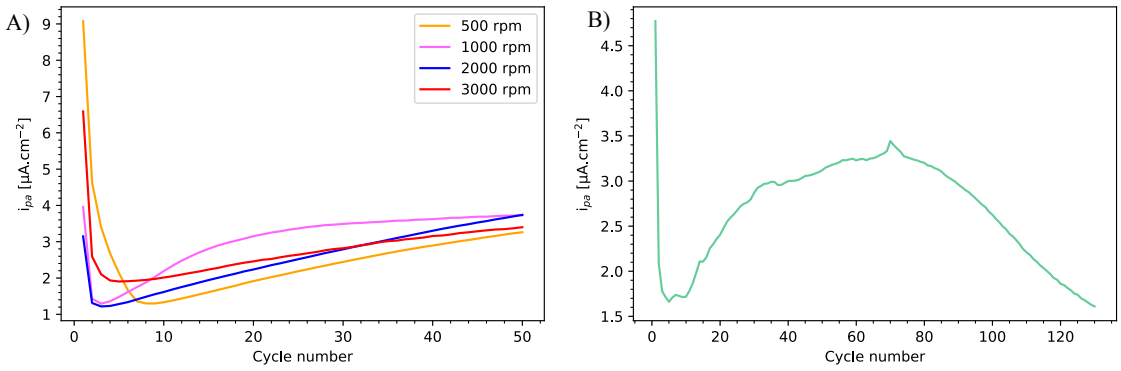

Figure 4.8: i_{pa}-CN plot from A) stability test of TemBen/Nafion® modified electrodes of various fabrication conditions and B) the extended stability test of the 500 rpm electrode.

The leaching of TenBen into the electrolyte may have been the reason for the decline of the i_{pa}. To prove this hypothesis, the electrolyte after the stability test was subjected to UV-Vis spectroscopy. The UV-Vis absorption of these electrolytes was compared with the UV-Vis absorption of the saturated TemBen solution in Figure 4.9. Due to the very small i_{pa}, after the stability test (< 5 μA.cm^{-2}) in every case, UV-Vis absorption is used to probe the leaching instead of comparing the cyclic voltammogram of the cycling and the fresh electrolyte used to investigate TEMPO/Nafion® modified electrodes. All of the electrolytes used in the stability tests show UV-Vis absorption similar to that of the saturated TemBen solution. This confirms the hypothesis that TemBen leaching is the cause of the instability of the electrolyte. Moreover, the UV-Vis absorption in all of the tested electrolyte is smaller than that of the saturated TemBen solution suggesting that the concentration of TemBen in these electrolytes has not reached saturation. Hence, TemBen will continue to leach out of the Nafion® matrix which will further deteriorate the i_{pa}.

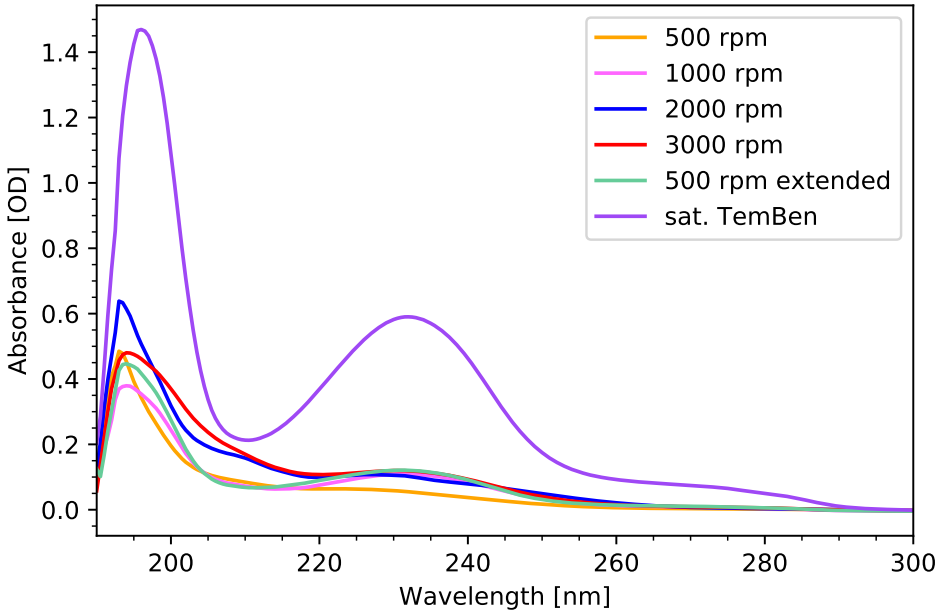

Figure 4.9: UV-Vis absorption spectra of the solution after stability test of various TemBen/Nafion® modified electrodes and the UV-Vis absorption spectrum of the saturated TemBen solution.

Despite the possible leaching of TemBen into the electrolyte, the improved stability of the TemBen/Nafion® modified electrodes may be enough to perform the electrolysis of HMF. We therefore performed the electrolysis of HMF using TemBen/Nafion® modified electrodes. The electrolysis of HMF was performed using the 500 rpm electrode. The current and passed charge as a function of reaction time are shown in Figure 4.10A. The current drops sharply from 8 μA.cm^{-2} to almost 0 μA.cm^{-2}. Shortly after the electrolysis, TemBen may have leached out from the Nafion® matrix, causing the sharp drop in the current. Despite a sharp drop in the current, the electrolysis was left running. The evolution of any of the intermediates would suggest the capability of TemBen/Nafion® modified electrode to perform HMF oxidation. The stability and the current of the TemBen/Nafion® can be further optimized. Nevertheless, the current continued to be very low (almost 0 μA.cm^{-2}). We decided to terminate the reaction after 23 hours. The linear sweep voltammogram before and after the reaction (23 hours) is shown in Figure 4.10B. The current density before the reaction was found to be around 8 μA.cm^{-2}. The current density decayed over the course of the reaction to approximately 0 μA.cm^{-2}. This observation is in good agreement with the relationship between the current as a function of reaction time (Figure 4.10A). We believe that the reduction in the current at 1.5 V vs. RHE is due to the leaching of TemBen from the electrode surface as discussed earlier. The linear sweep voltammogram after the electrolysis shows a higher current density from the applied potential of 2.0 V vs. RHE onward. Water oxidation by FTO is responsible for this current. The Nafion® layer may have hindered some part of the FTO surface

at the beginning of the reaction, reducing the contact between FTO and the electrolyte. After the extended electrolysis, the Nafion® may have also delaminated away from the electrode surface, exposing more FTO to the electrolyte. The higher exposed FTO area to the electrolyte increases the current density from the water oxidation reaction.

The total passed charge after the reaction is very low, 50 mC (Figure 4.10A). If this amount of charge were to be used to oxidize HMF, only 5.2 μM would have been consumed (the calculation is shown in the Appendix: Calculation for HMF consumption from photoelectrolysis of HMF using TemBen/Nafion® modified electrode). The concentration of HMF, the intermediates and FDCA as determined by HPLC before and after the electrolysis are shown in Table 4.1. The concentration of HMF reduced by 22 μM after the reaction with no detectable evolution of any of the intermediates nor the product, FDCA. We have shown in our control study that HMF degrades slowly under illumination (Table A.1). In addition, if TemBen could act as a catalyst for HMF oxidation, the evolution of some of the intermediates should have been detected. Therefore, we conclude that the observed reduction in HMF concentration is mainly due to this degradation under the illumination of HMF and TemBen cannot catalyze HMF oxidation.

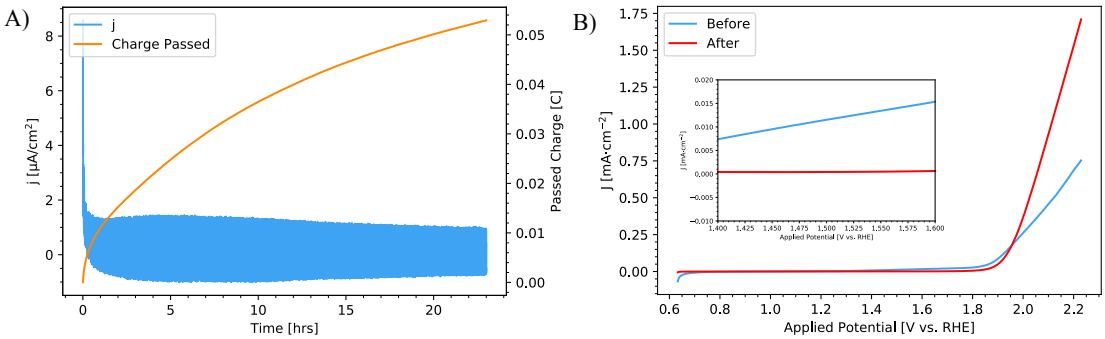

Figure 4.10: A) Chronoameperogram with passed charge and B) linear sweep voltammograms before and after the electrolysis of HMF solution using the 500 rpm electrode as a working electrode. The electrolysis was performed at the applied potential of 1.5 V vs. RHE in NaB_i solution at pH 9

	Concentration (μM)				
	HMF	DFF	HMFCA	FFCA	FDCA
Before	485	0	0	0	0
After	463	0	0	0	0

Table 4.1: Concentration of HMF, DFF, HMFCA, FFCA and FDCA before and after electrolysis of HMF solution using TemBen/Nafion®/FTO electrode as a working electrode.

In summary, the immobilization of TEMPO using Nafion® can be realized but the modified electrodes suffer from instability due to the gradual leaching of TEMPO into the electrolyte. Replacing TEMPO with the derivative with lower water solubility helps improve the stability of the modified electrode but the leaching still compromises the electrode stability. The electrolysis of the TemBen/Nafion® modified electrode shows that TemBen is likely to leach away quickly from the electrode surface under the operating conditions. No evidence of the capability of TemBen to catalyze HMF oxidation was found. Therefore, neither TEMPO/Nafion® nor TemBen/Nafion® modified electrodes are suitable for performing HMF oxidation due to the low stability of the catalyst layer.

4.2.3 NHPI

The strategy to immobilize electrocatalysts onto the electrode surface using Nafion® remains a feasible strategy. To tackle the issues of low current and electrode stability, we sought to replace TEMPO with other electrocatalysts for HMF oxidation. N-Hydroxyphthalimide (NHPI) is an interesting replacement for TEMPO as this molecule has been shown to catalyze various alcohol and aldehyde oxidation reactions to carboxylic acids.[27–32] Kompanets and co-workers reported the use of NHPI (with Cu^{2+} salt as a co-catalyst) to perform aerobic oxidation of HMF to DFF with a moderate yield.[33] To the best of our knowledge, NHPI has never been shown to catalyze electrochemical HMF oxidation. Therefore, the ability of NHPI to catalyze electrochemical HMF oxidation has to be first verified. During the catalytic cycle, NHPI is first oxidized to phthalimide N-Oxyl (PINO) which is the active species for the catalytic alcohol and aldehyde oxidation. This active species, PINO, then oxidizes alcohols or aldehydes and in turn, is reduced back to NHPI (Figure 4.11).[26]

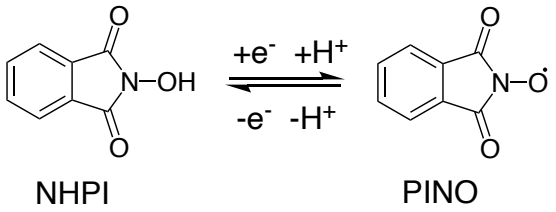

Figure 4.11: Electron transfer reaction of NHPI[26]

Cyclic voltammetry was used to assess the ability of NHPI to catalyze HMF oxidation electrochemically. The cyclic voltammograms are shown in Figure 4.12. The cyclic voltammogram of the electrolyte containing NHPI shows a quasi-reversible behavior. The oxidation of NHPI to PINO gives rise to the anodic peak with E_{pa} of 2.2 V vs. RHE, while the reduction of PINO back to

NHPI causes the cathodic peak with E_{pc} of 0.9 V vs. RHE. When HMF is introduced into the electrolyte, the cathodic peak disappears while the anodic peak remains roughly the same. The newly formed PINO rapidly oxidizes HMF and is reduced back to NHPI, causing the disappearance of the cathodic peak. This suggests that NHPI can catalyze HMF oxidation electrochemically.

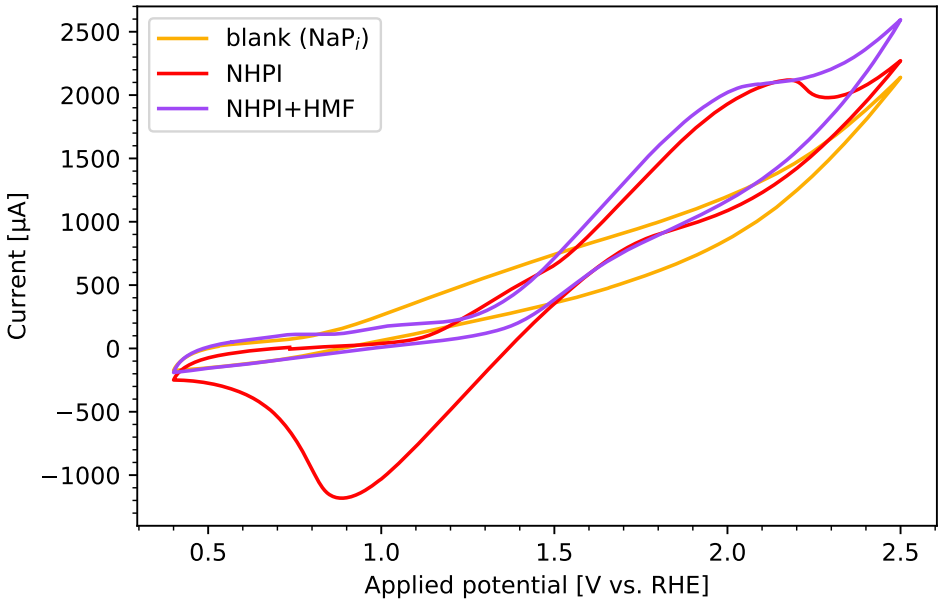

Figure 4.12: Cyclic voltammograms of the blank electrolyte (NaP_i) , 7.5 mM NHPI in NaP_i solution and 7.5 mM NHPI + 5 mM HMF in NaP_i solution. Graphite rode was used as a working electrode.

With a promising result from a graphite electrode, the graphite rod was replaced with WO_3 as a working electrode. The CVs were run both under 1 sun illumination and in the dark. The cyclic voltammograms are shown in Figure 4.13. In the dark, the cyclic voltammograms in the solution with and without NHPI show no difference. Under illumination, the increase in photocurrent of approximately 100 $\mu A.cm^{-2}$ is observed. The onset potential is also shifted cathodically by 150 mV. Nevertheless, no i_{pa} nor i_{pc} is observed. The absence of the i_{pa} may be caused by the faster kinetics of NHPI oxidation and the mass transfer of NHPI from the bulk to the electrode surface at this concentration compared to the rate of hole diffusion to the surface. The increased photocurrent when NHPI is presence, suggests that WO_3 can oxidize NHPI. Nevertheless, since the reversibility cannot be observed, we cannot conclude whether NHPI is oxidized to PINO (which should subsequently oxidize HMF) or being degraded.

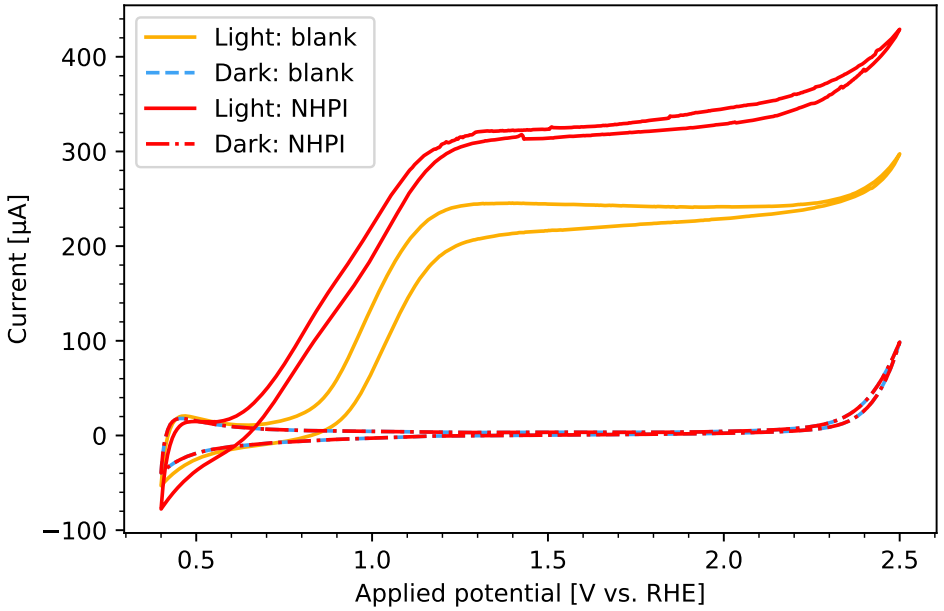

Figure 4.13: Cyclic voltammograms of WO_3 under illumination and in the dark in the blank solution (NaP_i solution) and 7.5 mM NHPI in NaP_i solution

To investigate the ability of NHPI as a catalyst for HMF oxidation with WO_3 as a working electrode, the photoelectrolyses of the solutions containing NHPI, HMF and both HMF and NHPI over WO_3 were conducted. The photocurrent and the passed charge as a function of the reaction time of all three solutions tested are depicted in Figure 4.14. Both the photocurrent and the passed charge of the solution containing 1 mM HMF are the highest followed by that of 1 mM HMF + 1.5 mM NHPI. The solution containing 1.5 mM NHPI gives the lowest photocurrent and passed charge. This suggests that WO_3 has higher reactivity toward HMF as compared to NHPI. Since the photocurrent and the passed charge of the solution containing both HMF and NHPI is lower than that of HMF alone, it can be inferred that NHPI reduces the reactivity of WO_3 toward HMF.

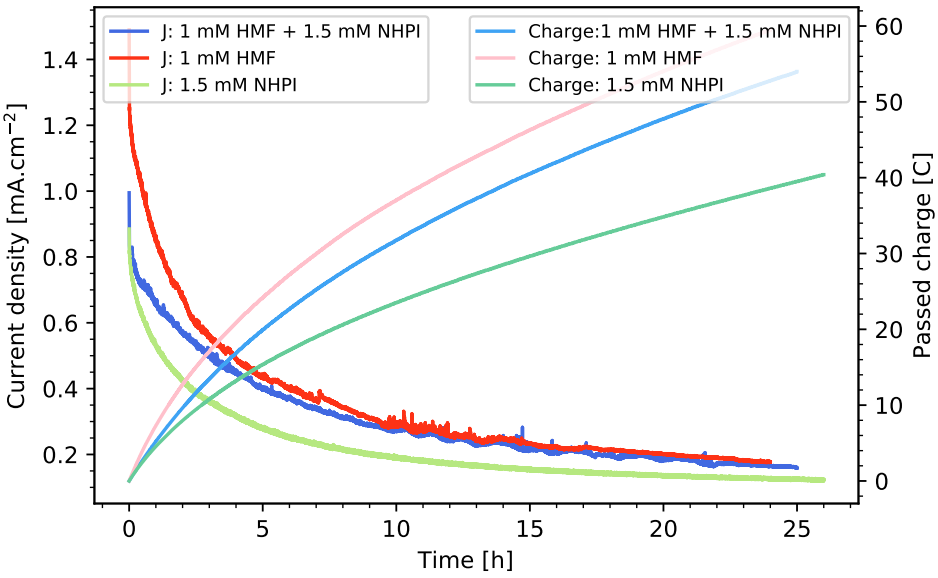

Figure 4.14: Photocurrent and the passed charge as a function of reaction time of the photoelectrolysis of the solution containing 1.5 mM NHPI, 1 mM HMF and both 1.5 mM NHPI and 1 mM HMF over WO_3. The photoelectrolyses were performed under 1 sun illumination and at the applied potential of 1.43 V vs. RHE

The concentration of HMF, the intermediates and FDCA as a function of passed charge from the photoelectrolysis of the solution containing HMF and both HMF and NHPI are shown in Figure 4.15. The consumption of HMF in both cases remains roughly the same. The evolution of the intermediates shows an improvement with the presence of NHPI. The concentration of DFF is slightly higher at the same amount of passed charge. The increase in the concentration is more pronounced for HMFCA and FFCA. The biggest improvement is observed in the product, FDCA. Without NHPI, the concentration of FDCA starts to decline after 30 C of charge has been passed. The decline is due to the degradation of FDCA by WO_3 discussed in chapter 2. Such decline is not observed when NHPI is presence. Despite an improvement in the concentration of FDCA and the disappearance of the decline in the FDCA concentration in the prolonged reaction, the yield of FDCA remains low ($\approx$ 1 %).

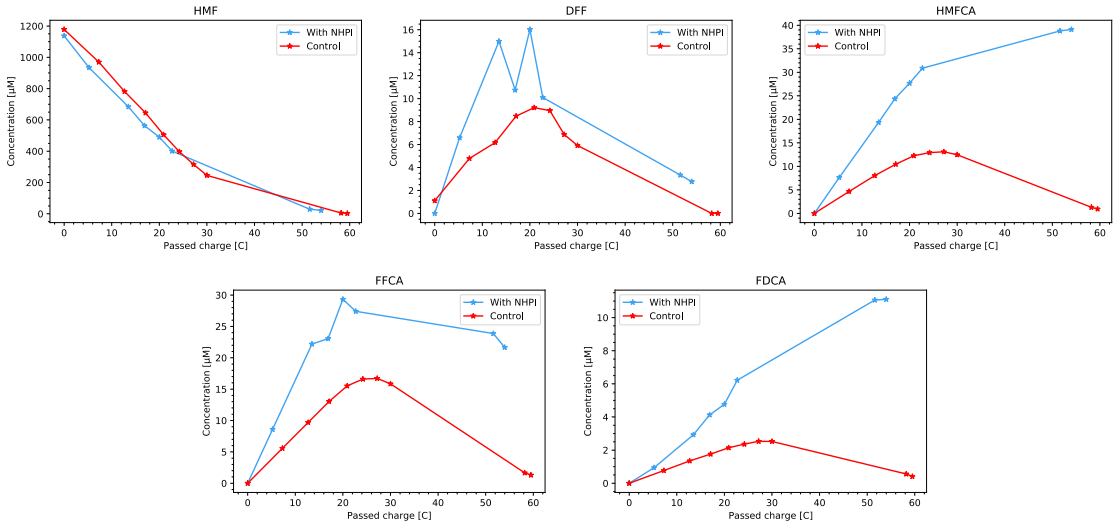

Figure 4.15: Concentration of HMF, DFF, HMFCA, FFCA and FDCA as a function of a passed charge from the photoelectrolysis of the solution containing HMF (denoted as control) and both HMF and NHPI (denoted as with NHPI).

The HPLC chromatograms from the photoelectrolysis of NHPI give an insight into the improved yield. First, the peak position of NHPI is determined. The chromatogram of 1 mM NHPI (Figure 4.16A) shows an unusual behavior where two peaks at the retention time (r.t.) of 33 and 77 minutes (these two peaks will be denoted as the rt-33 and rt-77 peak respectively hereafter) are observed. The rt-77 peak is much larger than the rt-33 peak. A tailing effect is also observed between the two peaks. NHPI has been used as a catalyst in many aerobic oxidation.[28,34–36] In other words, NHPI can be oxidized to PINO by atmospheric oxygen. We believe that the two peaks in the chromatogram belong to NHPI and PINO. The photoelectrolysis of NHPI was performed to aid the peak assignment. The peak area of the two peaks show an opposite trend where the rt-33 peak increases while the rt-77 peak decreases as the reaction progress (Figure 4.16B). We, therefore, hypothesized that the rt-33 peak and the rt-77 peak belong to PINO and NHPI respectively.

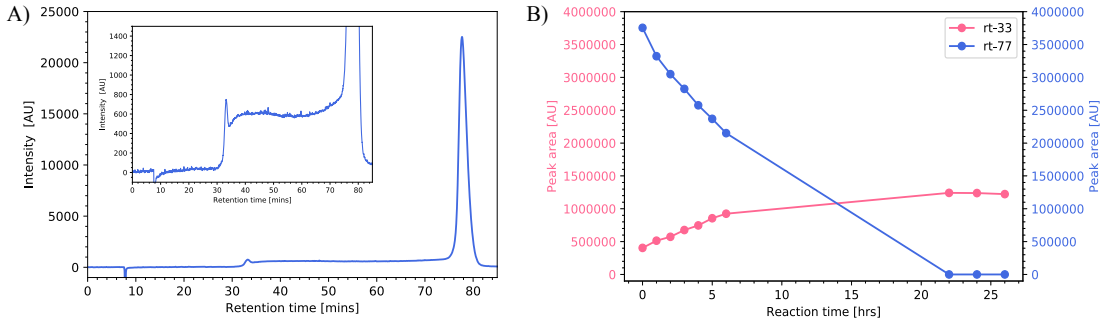

Figure 4.16: A) HPLC chromatogram of NHPI solution (1 mM) in NaP_i buffer. The inset shows the tailing between the rt-33 and rt-77 peaks. B) Peak area of the rt-33 and rt-77 as a function of reaction time from photoelectrolysis of NHPI over WO_3 electrode

The HPLC chromatogram before and after the photoelectrolysis of NHPI (Figure 4.17) suggests the degradation of NHPI by WO_3. Many new peaks appear after the photoelectrolysis. We believe that WO_3 can oxidize NHPI to PINO but can also degrade NHPI into multiple products. In addition to this, a comparison between the chromatogram of the NHPI and the NHPI+HMF solution after photoelectrolysis over WO_3 (Figure 4.18) suggests a peak overlap for FDCA and HMFCA. Two of the degraded products of NHPI appear at a retention time close to that of FDCA and HMFCA (retention times of 21.14 and 27.73 minutes respectively). The peak overlap results in an overestimation of the concentration of HMFCA and FDCA in the photoelectrolysis of the NHPI + HMF solution discussed earlier.

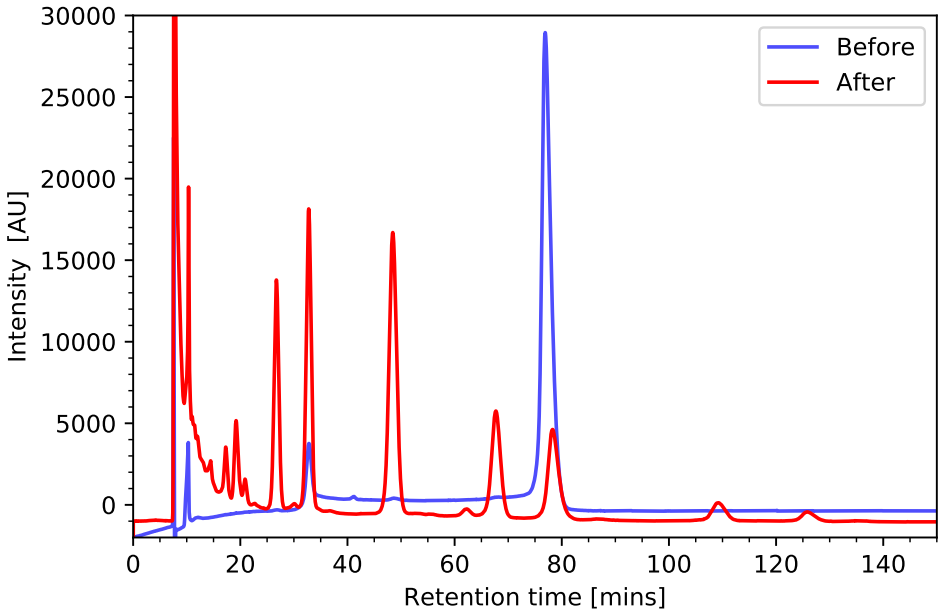

Figure 4.17: HPLC chromatogram of NHPI solution before and after photoelectrolysis over WO_3

Despite the overestimation of FDCA concentration due to the peak overlapping, the concentration of FDCA remains low. The calculated yield remains around 1 % despite a possible formation of the catalytic active species, PINO. This suggests that PINO may not be able to perform HMF oxidation and hence cannot be used as a catalyst under the current condition. Another possibility for the low FDCA yield is the produced FDCA is degraded by WO_3 as shown in Table 2.1, as the rate constant for FDCA degradation is very high. The presence of NHPI may have improved the FDCA yield but the produced FDCA is destroyed by WO_3. The degradation of NHPI by WO_3 also adds complexity to the system as NHPI now acts as another organic reactant for the degradation reaction. The kinetics and selectivity of the HMF oxidation may have been interfered with by the introduction of other competing substrates. To exclude the possible convolution of these factors, we

sought to mix PINO and HMF solutions and observe whether or not PINO can chemically oxidize HMF.

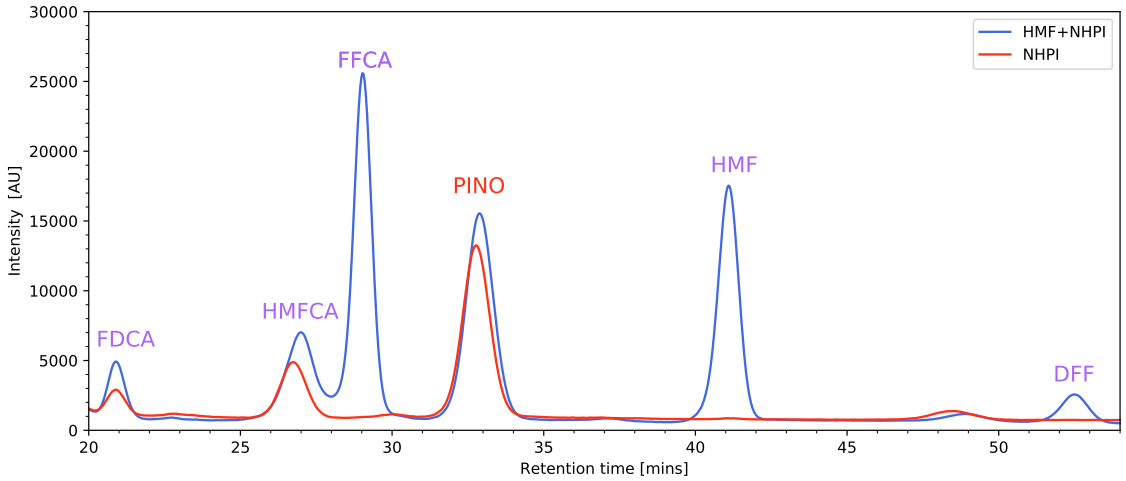

Figure 4.18: HPLC chromatogram of the HMF+NHPI and NHPI solution after the photoelectrolysis over WO_3

To realize this, the electrolysis of NHPI to produce PINO was performed over FTO to prevent the degradation of NHPI. The chromatograms before and after the electrolysis (Figure C.23) show an increase in the rt-33 peak area and a reduction in the rt-77 peak. Despite a stoichiometric amount of charge to perform 1-electron oxidation of NHPI to PINO being passed (7.24 C), the rt-77 peak is still present. This suggests a non-unity conversion of NHPI to PINO. Nevertheless, unlike the photoelectrolysis of NHPI over WO_3, no other observable peak besides the rt-33 and the rt-77 peaks is observed. This suggests that NHPI is not degraded under this electrolysis condition. The water oxidation reaction may have been a competing reaction since the electrolysis was performed at high applied potential (2 V vs. RHE). Based on the HPLC chromatogram, NHPI was partially converted to PINO. The solution after electrolysis was then mixed with the HMF solution (1 mM). The resulting solution was left stirring in the dark for 2 hours. Aliquotes from the resulting solution were taken immediately after the mixing and after 2 hours of stirring in the dark and were subjected to HPLC analysis. The resulting concentration of HMF, the intermediates and FDCA and the peak area of the rt-33 and the rt-77 peak are shown in Table 4.2.

If PINO is capable of oxidizing HMF, the concentration of HMF should decrease while the evolution of some of the intermediates or FDCA should be observed. The peak area of the rt-33 and the rt-77 peak should reduce and increase respectively as PINO oxidizes HMF and is reduced back to NHPI. An almost opposite behavior was observed. No evolution of the intermediates or FDCA was observed even after 2 hours of continuous stirring while the HMF concentration

dropped slightly. The rt-33 peak area increases while the rt-77 peak area drops after 2 hours. This observation suggests that NHPI cannot oxidize HMF to FDCA at the current condition. The slight drop in HMF concentration can be the result of aerobic oxidation. The change in the peak area of the rt-33 and the rt-77 peaks can also be the result of aerobic oxidation as NHPI has been reported to be a catalyst in many aerobic oxidations.[28,35–39] The oxidation of NHPI to PINO by the atmospheric oxygen results in the reduction of the rt-77 peak and the increase in the rt-33 peak area. In summary, NHPI cannot be used as a catalyst for HMF oxidation.

Time	Concentration (μM)					Peak area (AU)	
(hrs)	HMF	DFF	HMFCA	FFCA	FDCA	rt-33	rt-77
Immediately after mixing	559	0	0	0	0	1,013,454	1,877,127
2	540	0	0	0	0	1,146,748	1,800,394

Table 4.2: Concentration of HMF, DFF, HMFCA, FFCA, FDCA and the peak area of the rt-33 and the rt-77 peaks immediately after mixing the electrolyte from the electrolysis of NHPI using FTO as a working electrode with HMF solution and after 2 hours of stirring in the dark

4.3 Conclusions

Four electrocatalysts were introduced to the surface of WO_3 with an aim to improve the FDCA yield. The introduction of MnO_x results in a significant drop in the photocurrent with no improvement in the FDCA yield. Manganese oxides act as a recombination center when deposited onto the surface of WO_3. The TEMPO/Nafion® modified electrode shows a promising capability of oxidizing HMF but the electrode suffers from poor stability as TEMPO slowly leaches away from the Nafion® matrix. Replacing TEMPO with TemBen, the less water-soluble derivative of TEMPO, helps slow down the leaching, but the electrode stability remains insufficient for the extended electrolysis of HMF. The alternative electrocatalyst, NHPI, cannot oxidize HMF despite showing a promising result in CV. NHPI can undergo degradation on WO_3 in the photoelectrolysis condition. In conclusion, none of the catalysts tested can significantly improve the FDCA yield.

References

[1] Gao, L.; Liu, Z.; Ma, J.; Zhong, L.; Song, Z.; Xu, J.; Gan, S.; Han, D.; Niu, L. NiSe@ NiOx core-shell nanowires as a non-precious electrocatalyst for upgrading 5-hydroxymethylfurfural into 2, 5-furandicarboxylic acid. *Applied Catalysis B: Environmental* **2020**, *261*, 118235.

[2] Zhou, Z.; Chen, C.; Gao, M.; Xia, B.; Zhang, J. In situ anchoring of a Co 3 O 4 nanowire on nickel foam: an outstanding bifunctional catalyst for energy-saving simultaneous reactions. *Green Chemistry* **2019**, *21*, 6699–6706.

[3] Taitt, B. J.; Nam, D.-H.; Choi, K.-S. A comparative study of nickel, cobalt, and iron oxyhydroxide anodes for the electrochemical oxidation of 5-hydroxymethylfurfural to 2, 5-furandicarboxylic acid. *Acs Catalysis* **2018**, *9*, 660–670.

[4] Jiang, N.; You, B.; Boonstra, R.; Terrero Rodriguez, I. M.; Sun, Y. Integrating electrocatalytic 5-hydroxymethylfurfural oxidation and hydrogen production via Co–P-derived electrocatalysts. *ACS Energy Letters* **2016**, *1*, 386–390.

[5] Liu, W.-J.; Dang, L.; Xu, Z.; Yu, H.-Q.; Jin, S.; Huber, G. W. Electrochemical oxidation of 5-hydroxymethylfurfural with NiFe layered double hydroxide (LDH) nanosheet catalysts. *ACS Catalysis* **2018**, *8*, 5533–5541.

[6] Kubota, S. R.; Choi, K.-S. Electrochemical Oxidation of 5-Hydroxymethylfurfural to 2, 5-Furandicarboxylic Acid (FDCA) in Acidic Media Enabling Spontaneous FDCA Separation. *ChemSusChem* **2018**, *11*, 2138–2145.

[7] Huynh, M.; Bediako, D. K.; Nocera, D. G. A functionally stable manganese oxide oxygen evolution catalyst in acid. *Journal of the American Chemical Society* **2014**, *136*, 6002–6010.

[8] Cella, J. A.; Kelley, J. A.; Kenehan, E. F. Nitroxide-catalyzed oxidation of alcohols using m-chloroperbenzoic acid. New method. *The Journal of Organic Chemistry* **1975**, *40*, 1860–1862.

[9] Bobbitt, J. M.; BrüCkner, C.; Merbouh, N. Oxoammonium-and Nitroxide-Catalyzed Oxidations of Alcohols. *Organic Reactions* **2004**, 103–424.

[10] Rafiee, M.; Miles, K. C.; Stahl, S. S. Electrocatalytic alcohol oxidation with TEMPO and bicyclic nitroxyl derivatives: Driving force trumps steric effects. *Journal of the American Chemical Society* **2015**, *137*, 14751–14757.

[11] De Nooy, A. E.; Besemer, A. C.; van Bekkum, H. On the use of stable organic nitroxyl radicals for the oxidation of primary and secondary alcohols. *Synthesis* **1996**, *1996*, 1153–1176.

[12] Cha, H. G.; Choi, K.-S. Combined biomass valorization and hydrogen production in a photoelectrochemical cell. *Nature chemistry* **2015**, *7*, 328–333.

[13] Beejapur, H. A.; Zhang, Q.; Hu, K.; Zhu, L.; Wang, J.; Ye, Z. TEMPO in chemical transformations: from homogeneous to heterogeneous. *ACS Catalysis* **2019**, *9*, 2777–2830.

[14] Schätz, A.; Grass, R. N.; Stark, W. J.; Reiser, O. TEMPO Supported on Magnetic C/Co-Nanoparticles: A Highly Active and Recyclable Organocatalyst. *Chemistry–A European Journal* **2008**, *14*, 8262–8266.

[15] Tucker-Schwartz, A. K.; Garrell, R. L. Simple preparation and application of TEMPO-coated Fe3O4 superparamagnetic nanoparticles for selective oxidation of alcohols. *Chemistry–A European Journal* **2010**, *16*, 12718–12726.

[16] Wang, Y.; Song, X.; Shao, S.; Zhong, H.; Lin, F. An efficient, soluble, and recyclable multiwalled carbon nanotubes-supported TEMPO for oxidation of alcohols. *Rsc Advances* **2012**, *2*, 7693–7698.

[17] Campestrini, S.; Corvaja, C.; De Nardi, M.; Ducati, C.; Franco, L.; Maggini, M.; Meneghetti, M.; Menna, E.; Ruaro, G. Investigation of the Inner Environment of Carbon Nanotubes with a Fullerene-Nitroxide Probe. *Small* **2008**, *4*, 350–356.

[18] Gubskaya, V.; Berezhnaya, L. S.; Yanilkin, V.; Morozov, V.; Nastapova, N.; Efremov, Y.; Nuretdinov, I., et al. Phosphorylated methano [60] fullerenes containing nitroxyl radicals: synthesis, structures, and electrochemical behavior. *Russian chemical bulletin* **2005**, *54*, 1642–1655.

[19] Ishida, T.; Shinozuka, K.; Nogami, T.; Kubota, M.; Ohashi, M. Synthesis and characterization of C60 derivatives possessing TEMPO radicals. *Tetrahedron* **1996**, *52*, 5103–5112.

[20] Conti, F.; Corvaja, C.; Maggini, M.; Scorrano, G.; Ceroni, P.; Paolucci, F.; Roffia, S. A fulleropyrrolidine binitroxide: synthesis, EPR and electrochemical features. *Physical Chemistry Chemical Physics* **2001**, *3*, 3518–3525.

[21] Shakir, A. J.; Culita, D. C.; Calderon-Moreno, J.; Musuc, A.; Carp, O.; Ionita, G.; Ionita, P. Covalently grafted TEMPO on graphene oxide: A composite material for selective oxidations of alcohols. *Carbon* **2016**, *105*, 607–614.

[22] Ferreira, P.; Phillips, E.; Rippon, D.; Tsang, S. C.; Hayes, W. Poly (ethylene glycol)-supported nitroxyls: branched catalysts for the selective oxidation of alcohols. *The Journal of organic chemistry* **2004**, *69*, 6851–6859.

[23] Subhani, M. A.; Beigi, M.; Eilbracht, P. Polyurethane-and Polystyrene-Supported 2, 2, 6, 6-Tetramethyl-piperidine-1-oxyl (TEMPO); Facile Preparation, Catalytic Oxidation and Application in a Membrane Reactor. *Advanced Synthesis & Catalysis* **2008**, *350*, 2903–2909.

[24] Liu, S.; Chu, X.; Wang, H.; Zhao, F.; Tang, E. Preparation of nitroxide polymer brushes and their applications in the synthesis of an epoxidized soybean oil acrylate as an inhibitor. *Industrial & Engineering Chemistry Research* **2015**, *54*, 5475–5480.

[25] Belgsir, E.; Schäfer, H. Selective oxidation of carbohydrates on Nafion®–TEMPO-modified graphite felt electrodes. *Electrochemistry communications* **2001**, *3*, 32–35.

[26] Rafiee, M.; Karimi, B.; Alizadeh, S. Mechanistic Study of the Electrocatalytic Oxidation of Alcohols by TEMPO and NHPI. *ChemElectroChem* **2014**, *1*, 455–462.

[27] Chen, B.; Li, J.; Yang, G.; Gao, S. Aerobic oxidation of benzyl alcohols using a novel combination of N-hydroxyphthalimide (NHPI) with HNO3 and CuBr2. *Research on Chemical Intermediates* **2015**, *41*, 3929–3936.

[28] Yang, G.; Wang, L.; Li, J.; Zhang, Y.; Dong, X.; Lv, Y.; Gao, S. Aerobic oxidation of alcohols using a novel combination of N-hydroxyphthalimide (NHPI) and CuBr. *Research on Chemical Intermediates* **2012**, *38*, 775–783.

[29] Hu, Y.; Chen, L.; Li, B. NHPI/tert-butyl nitrite: A highly efficient metal-free catalytic system for aerobic oxidation of alcohols to carbonyl compounds using molecular oxygen as the terminal oxidant. *Catalysis Communications* **2016**, *83*, 82–87.

[30] Zhao, H.; Sun, W.; Miao, C.; Zhao, Q. Aerobic oxidation of secondary alcohols using NHPI and iron salt as catalysts at room temperature. *Journal of Molecular Catalysis A: Chemical* **2014**, *393*, 62–67.

[31] Rajabi, F.; Karimi, B. Efficient aerobic oxidation of alcohols using a novel combination N-hydroxy phthalimide (NHPI) and a recyclable heterogeneous cobalt complex. *Journal of Molecular Catalysis A: Chemical* **2005**, *232*, 95–99.

[32] Deng, W.; Luo, W.-P.; Tan, Z.; Liu, Q.; Liu, Z.-M.; Guo, C.-C. Remarkable effect of simple aliphatic alcohols on the controlled aerobic oxidation of toluene catalyzed by (T (p-Cl) PP) MnF/NHPI. *Journal of Molecular Catalysis A: Chemical* **2013**, *372*, 84–89.

[33] Kompanets, M.; Kushch, O.; Litvinov, Y. E.; Pliekhov, O.; Novikova, K.; Novokhatko, A.; Shendrik, A.; Vasilyev, A.; Opeida, I. Oxidation of 5-hydroxymethylfurfural to 2, 5-diformylfuran with molecular oxygen in the presence of N-hydroxyphthalimide. *Catalysis Communications* **2014**, *57*, 60–63.

[34] Arzumanyan, A. V.; Goncharova, I. K.; Novikov, R. A.; Milenin, S. A.; Boldyrev, K. L.; Solyev, P. N.; Tkachev, Y. V.; Volodin, A. D.; Smol'yakov, A. F.; Korlyukov, A. A., et al. Aerobic Co or Cu/NHPI-catalyzed oxidation of hydride siloxanes: synthesis of siloxanols. *Green Chemistry* **2018**, *20*, 1467–1471.

[35] Wang, L.; Wang, Y.; Du, R.; Dao, R.; Yuan, H.; Liang, C.; Yao, J.; Li, H. N-Hydroxyphthalimide (NHPI) Promoted Aerobic Baeyer-Villiger Oxidation in the Presence of Aldehydes. *ChemCatChem* **2018**, *10*, 4947–4952.

[36] Wang, L.; Zhang, Y.; Du, R.; Yuan, H.; Wang, Y.; Yao, J.; Li, H. Selective One-Step Aerobic Oxidation of Cyclohexane to -Caprolactone Mediated by N-Hydroxyphthalimide (NHPI). *ChemCatChem* **2019**, *11*, 2260–2264.

[37] Al-Taher, M. M.; Kalamaras, C.; Alqahtani, M. A.; Alomar, F. S. Aerobic oxidation of hydrocarbons using N-hydroxyphthalimide (NHPI) catalysts for cetane enhancement. *Fuel* **2022**, *324*, 124563.

[38] Gunchenko, P. A.; Li, J.; Liu, B.; Chen, H.; Pashenko, A. E.; Bakhonsky, V. V.; Zhuk, T. S.; Fokin, A. A. Aerobic oxidations with N-hydroxyphthalimide in trifluoroacetic acid. *Molecular Catalysis* **2018**, *447*, 72–79.

[39] Ishii, Y.; Sakaguchi, S. Recent progress in aerobic oxidation of hydrocarbons by N-hydroxyimides. *Catalysis today* **2006**, *117*, 105–113.

Chapter 5

Effects of Oxygen Vacancies on the Physical and Photoelectrochemical Properties of Copper Tungstate Photoanodes

5.1 Introduction

In the previous chapters, WO_3 was used as the photoatctive material in photoanodes. However, this material has a wide band gap which permits WO_3 to utilize only a small portion of the solar radiation spectrum. To address this limitation researchers have turned to the ternary metal oxide analogs of WO_3, many examples of these ternary metal oxides such as α –$SnWO_4$ [1–3], and Fe_2WO_6 [4,5] have been shown to have smaller bandgaps while retaining the stability of WO_3 in acid. Copper tungstate ($CuWO_4$) is one example of these ternary metal oxides. The bandgap of $CuWO_4$ has been reported in the range of 2.3 - 2.4 eV [6], which is approximately 0.5 eV smaller than that of WO_3 (2.7-2.8 eV) [6,7].The shrinkage of the bandgap of $CuWO_4$ is due to the less positive valence band edge of $CuWO_4$ compared to that of WO_3. The conduction band and the valence band of WO_3 mainly compose of the contribution from W $5d$ orbitals and the O $2p$ orbitals respectively. For $CuWO_4$, while the conduction band remains largely composed of the contribution from W $5d$ orbitals at the same energy level as in WO_3, the valence band has the additional contribution from the Cu $2d$ orbitals in addition to that of the O $2p$ orbitals. The added contribution from the Cu $3d$

orbitals results in the less positive valence band edge in $CuWO_4$, which in turn is smaller than the band gap value of this ternary metal oxide (Figure 5.1).[8]

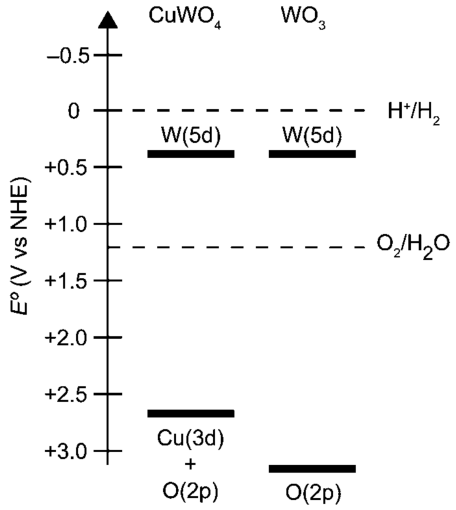

Figure 5.1: Band diagrams for $CuWO_4$ and WO_3. Adapted from ref.[8] with the permission of © 2011 Royal Society of Chemistry Publishing

In addition to a smaller band gap, $CuWO_4$ processes other advantages over WO_3. The stability over a larger pH range is one of the key advantages. While WO_3 is only stable in strongly acidic conditions and starts to dissolve in the solution from pH > 5,[9] $CuWO_4$ has been reported to be stable up to pH 10.[10] The larger range of pH stability allows this ternary oxide to be used not only in acidic conditions but also in neutral and even dilute basic conditions which help expand the application range for this material. Improved photostability is another key advantage of $CuWO_4$. WO_3 has moderate selectivity toward the OER and produces peroxide species as side products when performing water oxidation.[11] The produced peroxide species, in turn, degrade the surface of WO_3, resulting in poor photostability over an extended period of operation time. $CuWO_4$ has been shown to have nearly unity selectivity toward the OER reaction, resulting in greater photostability in comparison to WO_3.[12] Despite some key advantages of $CuWO_4$ over WO_3, this ternary metal oxide has been shown to have low charge separation efficiency (η_{sep}) which results in the observed photocurrent to be much lower than the theoretical maximum photocurrent density (J_{max}).[13]

In an ideal case where all of the absorbed photons with energy equal to or greater than the band gap of the photoanode materials are used in the OER, J_{max} is the function of the band gap energy (Figure 5.2A). In practice, however, the observed photocurrent (J_{PEC}) is lower than J_{max} due to the loss from charge recombination (Figure 5.2B). Not every photogenerated hole participates in the OER at the surface of the photoanode. Multiple recombination pathways, both in the bulk

and at the surface of the photoanode, can consume the photogenerated holes, preventing them from participating in the OER at the surface. These recombination pathways in the bulk and at the surface of the photoanode are summarized in Figure 5.2C and 5.2D respectively. Pathway 3 is the desired pathway in which the photogenerated holes diffuse from the bulk to the surface of the photoanode and participate in the OER while the photogenerated electron is collected at the Ohmic contact. This desired pathway is the only pathway in these two diagrams that result in a photocurrent. The other pathways result in a recombination loss.

In the bulk, there are two possible recombination pathways. The photogenerated electron in the CB can undergo recombination with the photogenerated holes in the VB. This pathway is known as band-to-band recombination (Figure 5.2C, pathway 1). Alternatively, the photogenerated electron-hole pair can recombine at a trap state within the bulk. This pathway is referred to as recombination via defect states in the bulk (Figure 5.2C, pathway 2). At the surface of the photoanode, despite the fact that the built-in electron field from the band-bending improves the charge separation, the recombination of the photogenerated hole is still possible. The photogenerated holes can recombine at the surface trap states (Figure 5.2D, pathway 4) or recombine with the electron in the conduction band (back electron-hole pair recombination, Figure 5.2D, pathway 5).[14] These recombination pathways at the surface compete with the OER.

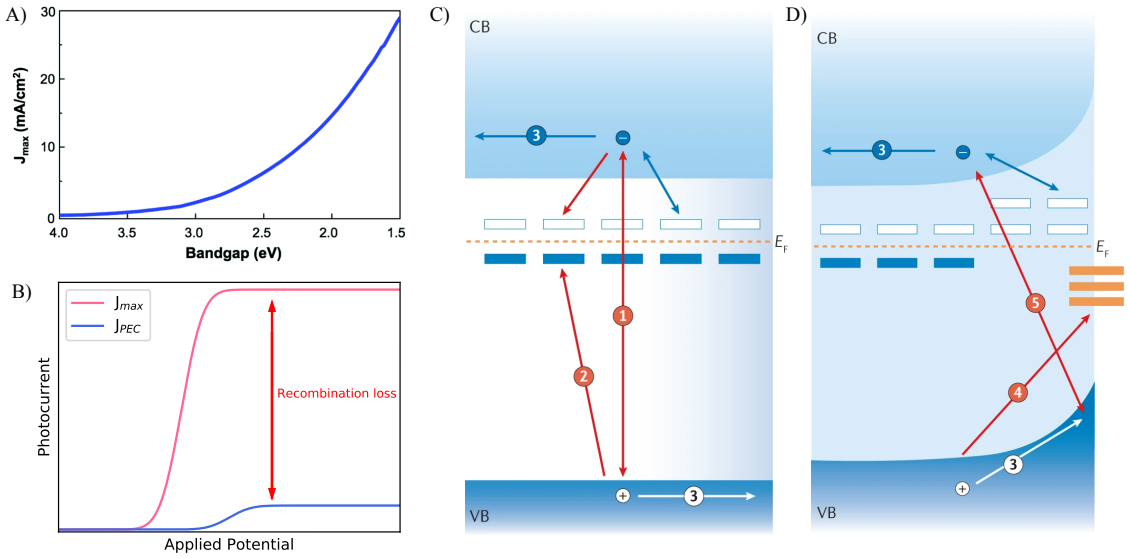

Figure 5.2: A) Theoretical maximum photocurrent (J_{max} as a function of the band gap of a semiconductor. B) LSV showing J_{max} and J_{PEC}. Scheme of charge separation and recombination C) in the bulk and D) at the surface of a photoanode. Figure A) is adapted from ref.[13] with the permission of © 2019 Royal Society of Chemistry Publishing. Figures C) and D) are adapted from ref.[14] with the permission of © 2021 Springer Nature publishing

The relationship between J_{max} and J_{PEC} is described in Equation 5.1. Here, η_{sep} and η_{inj} are

the efficiency of charge separation in the bulk and the efficiency of the charge injection into the solution respectively.[15]

$$J_{PEC} = J_{max} \times \eta_{sep} \times \eta_{inj} \tag{5.1}$$

Most metal oxide photoanode materials suffer from low η_{sep}, $CuWO_4$ included. The value of the η_{inj} for most materials is higher than η_{sep}. Additionally, η_{inj} can be improved by the decoration with an electrocatalyst for OER onto the surface of the photoanode while η_{sep} is more challenging to improve as it stems from the bulk properties of the photoanode.[13] Therefore, the focus has typically been shifted toward improving η_{sep}. Doping has been shown to be an effective methods to mitigate low photocurrent. Dopants are introduced to the bulk of the material ($CuWO_4$ in this case) to improve the charge transport (from the bulk to the surface), resulting in improved photocurrent. An oxygen vacancy (OV) is one of the example dopants in metal oxides. This loss in the oxygen atoms in the semiconductor crystal is one of the most common defects in metal oxides and has also been reported to be a dopant in many metal oxide semiconductors as well. Since the presence of an OV results in the reduction of some metals in the metal oxide crystal, an OV is considered an n-type dopant.

For $CuWO_4$, OVs have been shown to help improve the photocurrent. The presence of the OVs have been linked to increased electron conductivity in the bulk[16–20] as well as improved charge separation and charge injection efficiency[16,17,20]. Nevertheless, if OV only helps improve the photocurrent, then one would expect the photocurrent to increase with the number of OVs before eventually reaching a plateau where the increase in the number of OVs no longer improves the photocurrent. In reality, multiple reports have shown a different story from this ideal case. The photocurrent does go up with the number of OV. Once too many OVs are introduced to the system, the photocurrent does not plateau but rather decreases.[17,18,20] In other words, there is an optimum point in the number of OVs whereafter too many has a detrimental effect on the photocurrent. Guo and co-workers studied the effect of OV on the $CuWO_4$ and found that despite the fact that $CuWO_4$ with more OVs exhibits higher photocurrent, the presence of OVs increases the charge recombination at the surface. The authors suggested that OVs create trap states at the surface of $CuWO_4$ which causes charge recombination.[16]

Despite such observations in many reports, the focus has been shifted toward understanding the benefit of an OV to the photocurrent but few try to address the reason for the negative impact when an excessive number of OVs are present in the system. Multiple factors contribute to the photocurrent. While some factors such as electron conductivity may improve the photocurrent,

some other factors such as the density of the surface trap state have an adverse effect. An OV may increase the number of species for many factors (for example increasing both electron conductivity and the density of the surface trap state) resulting in an optimum point for the improvement of the photocurrent. In this chapter, a series of $CuWO_4$ with different numbers of OVs were fabricated and the effect of the number of OVs on the factors that affect the photocurrent of $CuWO_4$ is explored. The reasons behind both positive and negative effects of the number of OVs on the photocurrent are investigated and discussed.

5.2 Results and discussion

Copper tungstate films with a different number of OVs were fabricated using a sol-gel method. The precursor solution was deposited onto an FTO substrate by spin coating and then annealed under compressed air at 550 °C for 1 hour. OVs were introduced by subjecting the $CuWO_4$ film to secondary annealing under a reductive atmosphere (13 % H_2 in Ar, at 300 °C) for different amounts of time. It is predicted that longer the secondary annealing times, lead to more OVs present in the film. The full detail of the synthesis is discussed in the experimental section in the Appendix D. Four conditions of the $CuWO_4$ films were fabricated (conditions A, B, C, and D). The photograph of these $CuWO_4$ films on an FTO substrate is shown in Figure 5.3. The film in condition A was not subjected to secondary annealing while the films in conditions B, C, and D were subjected to secondary annealing for 20, 60, and 80 minutes respectively.

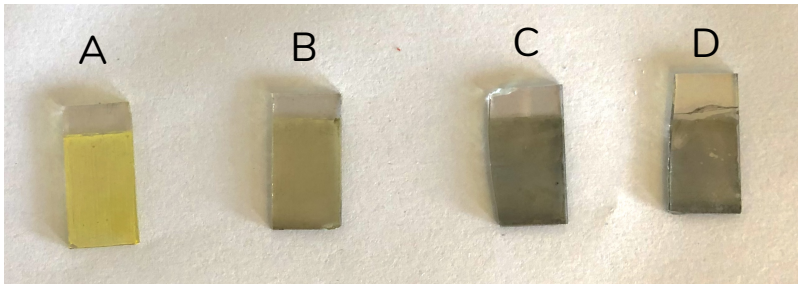

Figure 5.3: Photograph of $CuWO_4$ films for conditions A, B, C and D on FTO substrates ($\sim$ 1.25 $\times$ 2.5 cm)

The number of OVs can be indirectly determined by the oxidation state of the constituent metals in the films.[21] Therefore, the four films were subjected to x-ray photoelectron spectroscopy (XPS) to determine the oxidation state of Cu and W in each of the conditions. The XPS spectra for Cu and W are shown in Figure 5.4A and 5.4B respectively. The Cu $2p_{3/2}$ peak can be used to quantify the relative amount between Cu(II) and Cu(I)/Cu(0). The main Cu $2p_{3/2}$ peak appears around 933 eV. If Cu(II) is present, two satellite peaks at around 940 - 947 eV will appear. The

presence of Cu(I) or Cu(0) gives rise to another main peak around 933 eV. The exact peak position of these four peaks differs from sample to sample.[22] Nevertheless, XPS cannot distinguish between Cu(I) and Cu(0) due to the peak overlapping.[23] The ratio between the peak area of peak 2-4 and peak 1 gives the relative ratio between Cu(II) and Cu(I)/Cu(0) in the sample.[24] The percentage of Cu(I)/Cu(0) to the total Cu of the four conditions for the $CuWO_4$ films is shown in Table 5.1. The percentage of Cu(I)/Cu(0) to the total Cu increase progressively from 17 % in condition A to 64 % in condition D. For W, both W(V) and W(VI) give rise to a doublet in W 4f binding region (W $3f_{5/2}$ and W $3f_{7/2}$). The doublet peak of W(VI) appears at higher binding energy around 36 and 38 eV compared to that of W(V) at 34.8 and 36.8 eV.[21] In all four conditions, no presence of W(V) is observed. All of the W atoms remain at a +6 oxidation state. This behavior where the reduction only affects Cu atoms and leaves W intact is in line with previous reports.[20] Since 2 Cu(I) atoms give rise to 1 OV site while 1 Cu(0) atom will bring about 1 OV site, the relative ratio between Cu(I) and Cu(0) is crucial to determine the percentage of OV in the film. As this ratio cannot be reliably determined, the percentage of OV cannot be exactly calculated. Nevertheless, we believe that the number of OVs increases with the percentage of Cu(I)/Cu(0) to the total Cu. Therefore, the number of OVs in condition D > C > B > A.

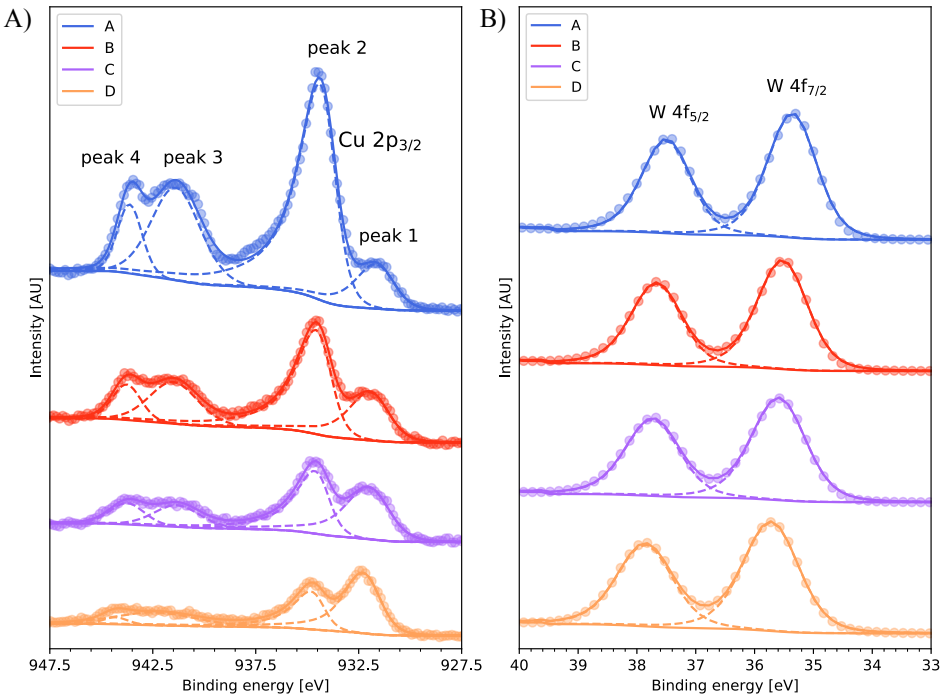

Figure 5.4: XPS spectra of $CuWO_4$ films for conditions A, B, C and D. A) A Zoom in of Cu $2p_{3/2}$ region and B) A zoom in of W 4f region.

Condition	Percentage of Cu(I)/Cu(0) to the total copper (%)
A	17
B	33
C	50
D	64

Table 5.1: Percentage between Cu(I)/Cu(0) to the total copper of the electrode in condition A, B, C and D as determined from XPS.

It can be seen in Figure 5.3 that the $CuWO_4$ films appear darker with an increasing number of OVs. The condition A film is yellow while the condition D is grey. The band gap of the film at all four conditions was determined by Tauc plot (Figure D.1) and was found to be identical at 2.5 eV. Despite having the same band gap, the UV-Vis absorption spectra (Figure 5.5) show broad absorption in the sub-band gap region ($\lambda > 496$ nm), increasing from condition A to D. The darker appearance and the increase in the sub-band gap region are in line with work performed by Tang and co-workers.[17]

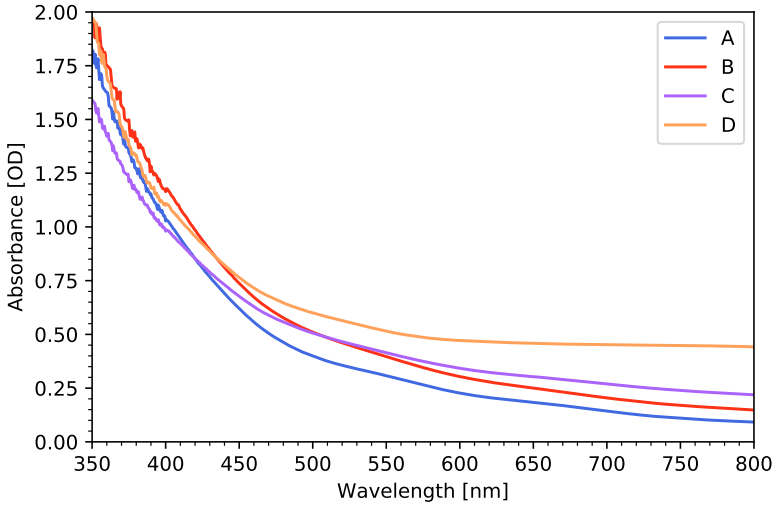

Figure 5.5: UV-Vis spectra of the $CuWO_4$ film condition A, B, C and D

The morphology of the films was examined by scanning electron microscope (SEM). The electron micrographs are shown in Figure 5.6. All four conditions were found to produce films with porous morphology. A cross-sectional SEM micrograph of the condition A film (Figure D.2) suggests that

the film thickness is approximately 400 nm. Nevertheless, independent particles with sizes ranging from 200-700 nm are observed on the surface of the films in conditions C and D (Figure 5.6C and Figure 5.6D). The number of these particles in condition D is higher than in condition C. These particles have well-defined crystal facets, suggesting that these particles may be crystalline.

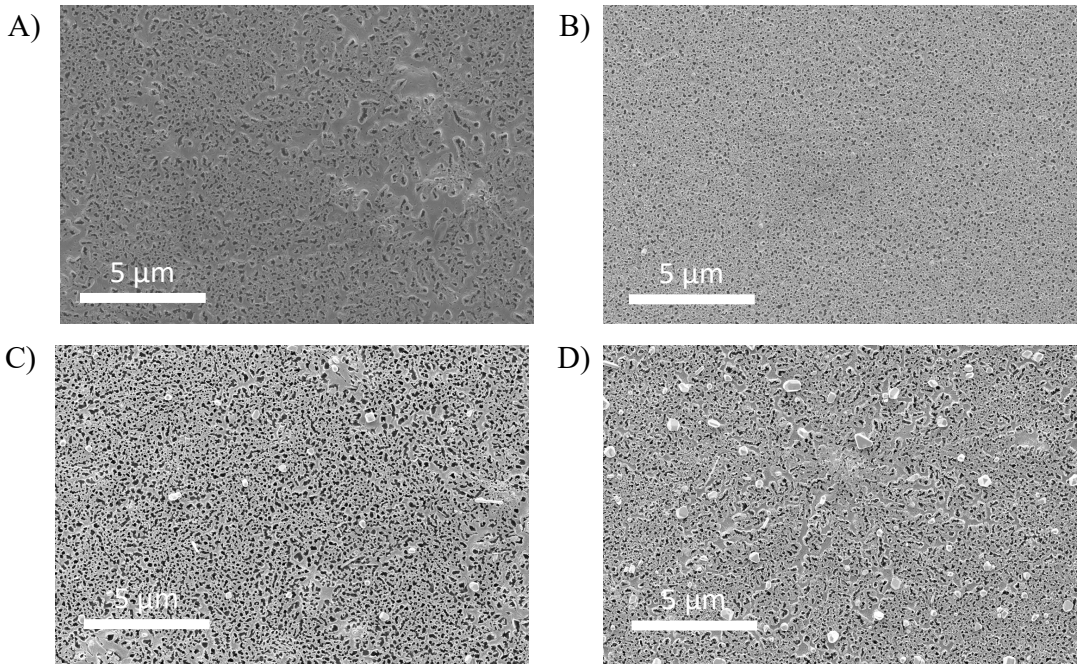

Figure 5.6: Top-down SEM micrographs of $CuWO_4$ films of A) condition A, B) condition B, C) condition C and D) condition D.

The chemical and structural identity of the $CuWO_4$ film of all four conditions is examined using Raman spectroscopy and X-ray diffraction (XRD). The Raman spectrum (Figure 5.7A) for each condition is identical to the reference spectrum reported in the literature, confirming the identity of $CuWO_4$.[25] The XRD spectra are shown in Figure 5.7B. The XRD spectra for the condition A and B films are identical to one another. Apart from the diffraction peaks from the FTO substrate, every peak corresponds well with the reference spectrum. It should be noted that some peaks in the reference spectrum do not appear as the XRD spectra shown here are obtained from the thin film of $CuWO_4$, not powder. The XRD spectrum of conditions C and D start to show signs of peak broadening as compared to the spectra of conditions A and B. Some small peaks also start to disappear (a peak at $2\theta = 19.5^\circ$ and peaks at 2θ ranges from 29° - 34°). This phenomenon has been suggested to arise from the loss of crystallinity.[17] The degree of peak broadening and disappearing in condition D is more pronounced than the condition C. Interestingly, a peak at 43.5 degrees emerges in conditions C and D (highlighted in blue in 5.7B). The intensity of this emerging peak in

condition D is higher than that of condition C, contradicting the peaks of $CuWO_4$ which show signs of broadening and disappearance . The new peak does not match with the peaks in the reference spectrum, suggesting a formation of a new phase not belonging to $CuWO_4$. The comparison of this emerging peak to the diffraction patterns of the species related to $CuWO_4$ (Cu metal, CuO, Cu_2O, W metal, and WO_3) suggests that this emerging peak may have come from the diffraction pattern of Cu metal (Figure 5.7C). The formation of Cu(0) suggests that the particles observed on the surface of the condition C and D films might be Cu metal particles (Figure 5.6C and Figure 5.6D). The higher XRD peak intensity of condition D compared to condition C also reflects the larger abundance of the crystalline particles found on the surface of the condition D film. In addition, the formation of Cu particles may have contributed to a broad absorption in the sub-band gap region observed in the UV-Vis absorption spectra (Figure 5.5).

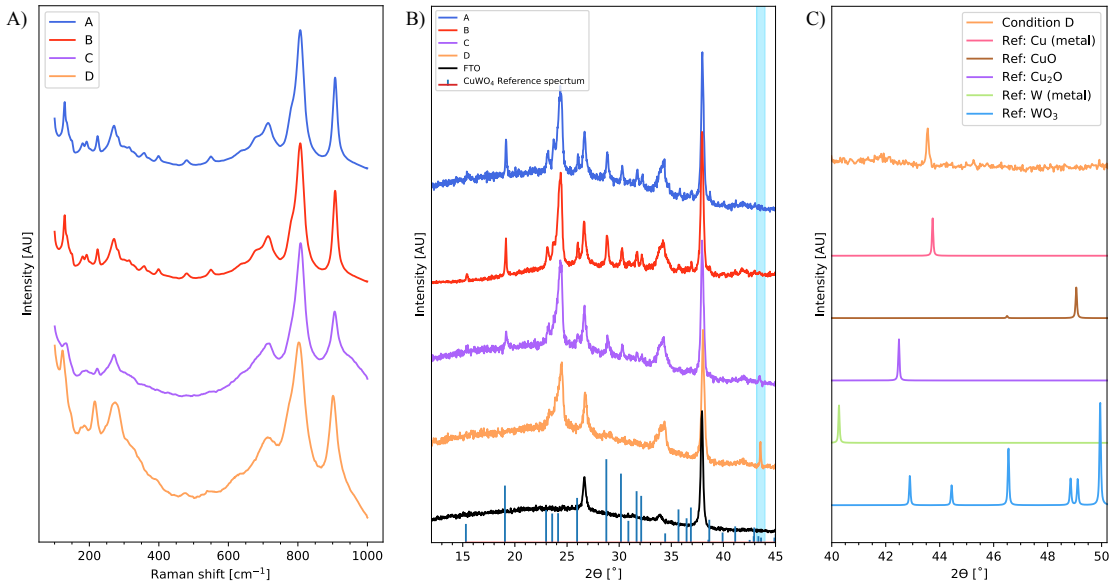

Figure 5.7: A) Raman spectra and B) XRD spectra of the $CuWO_4$ films for conditions A, B, C and D. C) Comparison of the XRD spectrum of condition D film with various reference spectra.

Photoelectrochemical properties were examined using a chopped-light illumination linear sweep voltammogram. The voltammograms of the four condition $CuWO_4$ conditions are shown in Figure 5.8A. The photocurrent density at 1.23 V vs. RHE ($J_{1.23Vvs.RHE}$) is one of the parameters used to assess the performance of a photoanode. Here, it is found that condition A produces the highest photocurrent density at this potential. The $J_{1.23Vvs.RHE}$ decreases with an increasing number of OVs (Figure 5.8B). Nevertheless, at higher potentials greater than 1.75 V vs. RHE (Figure 5.8C), condition B produces the highest photocurrent density, slightly higher than that of condition A. The photocurrent of the condition C and D films are lower than that of the condition A and B at both

1.23 and 1.75 V vs. RHE. This observation infers that the number of OVs in these two conditions are already beyond the optimum point. Furthermore, the photocurrent of the condition C film is higher that that of D at both applied potentials which suggests that an excess number of OV pose a detrimental effect to the photocurrent. As for conditions A and B, since the photocurrent density at 1.75 V vs. RHE of B is only slightly higher than that of condition A, it is possible that the optimum point for the number of OVs lies between conditions A and B. The gap between the percentage of Cu(I)/Cu(0) between the condition A and B (17 % and 33 % respectively, Table 5.1) is also relatively big. The optimum point of the number of OVs may reside between the percentage of Cu(I)/Cu(0) of 17 % and 33 %. To discount this possibility, $CuWO_4$ films with a secondary annealing time of 5 and 10 minutes were fabricated and subjected to photoelectrochemical testing. Since the annealing time for the secondary annealing of the condition B electrode is 20 minutes, the number of OVs in these two films should lie between that conditions A and B. If the optimum point for the number of OVs exits between conditions A and B, the photocurrent density of these two films should be higher than that of conditions A and B. Nevertheless, the photocurrent density of these two new middle conditions are lower than that of condition B at both 1.23 and 1.75 V vs. RHE (Figure D.3A and D.3B). We, therefore, conclude that there is no optimum point between conditions A and B. Currently, condition A gives the highest photocurrent density at 1.23 V vs. RHE, while at the higher applied potential of 1.75 V vs. RHE, condition B is the optimum condition. We believe that the efficiency of charge separation (η_{sep}) and the efficiency of charge injection (η_{inj}) may account for this difference in the optimum point at the different conditions and will be discussed later.

Another key difference between the voltammograms in condition A and the rest is the onset potential of the dark current. The dark current onset of condition A film is around 2 V vs. RHE while the rest start at around 1.8 V vs. RHE. The shift of the onset potential to the more negative potential can be linked to the introduction of the electrocatalyst onto the surface of the photoelectrode. Nevertheless, the introduction of the electrocatalyst onto the surface of the photoanode should also result in an improved photocurrent which is not observed here. In addition, the charge injection efficiency (η_{inj}) of the photoanode decorated with an electrocatalyst should be higher than that of the bare photoanode. Again, this is not observed in the case presented here (discussed later). Therefore, the improvement in the dark onset potential is unlikely due to the formation of the electrocatalyst species during the secondary annealing. Since the introduction of OVs has been shown to improve the electron conductivity in the bulk [19,20], we believe that the improved dark current onset potential is likely due to the improved film conductivity.

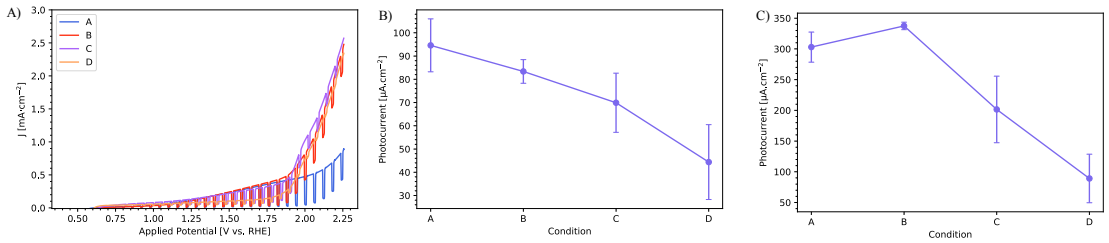

Figure 5.8: A) Chopped-light illumination linear sweep voltammograms of $CuWO_4$ films condition A, B, C and D (in 0.1 M KP_i buffer pH 7). Average photocurrent density at B) 1.23 V vs. RHE and at D) 1.75 V vs. RHE of $CuWO_4$ films condition A, B, C and D. The average photocurrent was calculated from three samples per condition.

After multiple consecutive LSV runs, the condition C and D films were noticeably damaged (Figure 5.9A). The areas subjected to LSV testing became pale in color which could be a sign of a film dissolution. To gain more insight, the condition D film after LSV was examined using SEM (Figure 5.9B). Here, part of the film is still visible but the FTO substrate is now visible in some parts. The $CuWO_4$ fully covers an FTO substrate before the LSV run (Figure 5.6D). This confirms the film's dissolution during the LSV run. A clear difference in the film before and after the LSV run is also observed in Raman spectra for both condition C and D. After the LSV run, the peak at 904 cm^{-1} disappear in both conditions. These new Raman spectra match very well with the reference spectrum of WO_3. We believe that the poor stability of the film in both conditions arises from the over-reduction of both films leading to an excess of Cu atoms that have been reduced to Cu(0). These reduced Cu (0) atoms move out of the crystal lattice of $CuWO_4$, causing both a reduction in the crystallinity, as observed in XRD in Figure 5.7B, as well as agglomerate to form a crystalline Cu(0) particles. Note that the percentage of reduced Cu in condition B may not be high enough to cause agglomeration. Hence the preserved crystallinity is seen in the XRD spectrum. During the LSV run, the agglomerate Cu(0) particles are re-oxidized back to Cu(II), but since they are not part of the crystal lattice of $CuWO_4$, the oxidized Cu(II) atoms dissolve into the solution, leaving behind a non-crystalline WO_3.

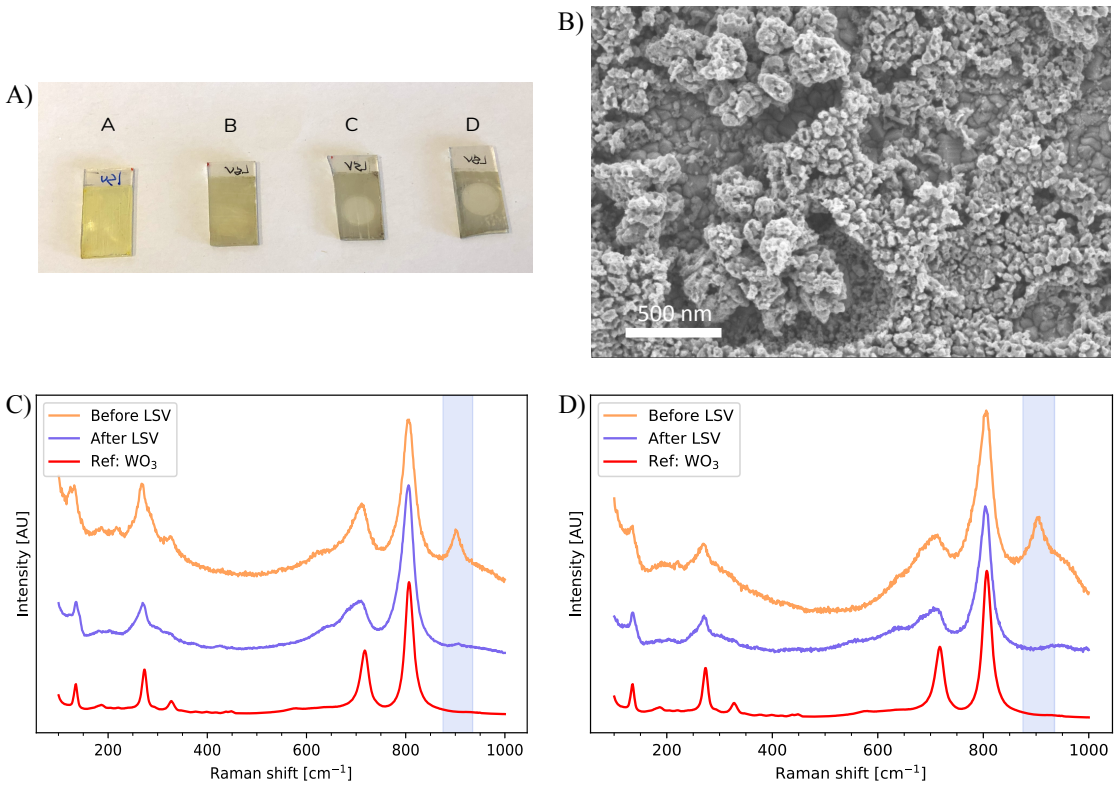

Figure 5.9: A) Photographs of $CuWO_4$ electrode conditions for A, B, C and D after undergoing LSV. B) A top-down SEM micrograph of the $CuWO_4$ film condition D after LSV. Raman spectra of the $CuWO_4$ film condition C) C and D) D before and after undergoing LSV.

Despite the films in conditions C and D exhibiting lower photocurrent and poorer stability under operating conditions compared to the films in conditions A and B, the UV-Vis absorption of the films in these two conditions in the sub-bandgap region is higher than that of conditions A and B. Based on the UV-Vis absorption, the condition C and D films have the potential to harvest more solar energy than the condition A and B films, assuming the absorption in the sub-band gap region results in the photocurrent. Therefore, the films of all conditions were subjected to incident photon-to-current efficiency (IPCE) measurements.

The IPCE measurements show that photons with a wavelength longer than approximately 500 nm do not contribute to the current generation at both 1.23 and 1.75 V vs. RHE in any of the conditions (Figure D.4). The increased absorption in the sub-band gap region (especially in conditions C and D) may come from the absorption of Cu(0) particles which do not result in the current generation. Upon a closer examination of the IPCE measurement, more insights can be drawn. The IPCE as a function of wavelength at 1.23 and 1.75 V vs. RHE of each condition are plotted in Figure 5.10. The IPCE behavior can be divided into two groups, conditions A and B and conditions C and D. In the former group, the onset of the IPCE at the two applied

potentials are different. At 1.23 V vs. RHE, the onset of IPCE starts at around 450 nm. The onset shifts to approximately 500 nm at 1.75 V vs. RHE. The difference in the onset of the IPCE can be confirmed by normalizing the IPCE. Indeed, the normalized IPCE (Figure D.5) confirms the difference in the onset of IPCE between the two applied potentials. The difference in the IPCE comes from the difference in the penetration depth of photons at a given wavelength. Lower wavelength photons can penetrate less into the bulk and tend to be absorbed closer to the surface. Hence, the photogenerated holes from the lower wavelength are generated near the surface. The longer wavelength, on the other hand, can penetrate deeper and generate photogenerated holes deep into the bulk of the material. There are two mechanisms that drive the transport of the free charge carrier to the surface of the photoelectrode; drift and diffusion. The diffusion of free charge carriers is simply the movement of charges through a concentration gradient. The average length that the photogenerated holes can travel before recombining (hole diffusion length) depends on many parameters. Material choice is one of the key parameters. For drifting, the movement of charges is governed by an electric field. For the photoanode under operating conditions, the band bending generates the built-in electric field which drives the drift of charges near the surface. The size of the band bending (the depletion width) is a function of an applied potential. The higher the applied potential, the larger the depletion width. In the material with low hole diffusion length, the photogenerated holes from the bulk tend to recombine before reaching the surface. The holes that participate in the current generation are mainly generated near the surface and are driven to the surface via the built-in electric field. The depletion width at 1.75 V vs. RHE is larger than that of 1.23 V vs. RHE. Therefore, the built-in electric field can drive the holes generated deeper in the bulk, which is generated by the longer wavelength photons, to the surface. This results in the onset of the IPCE at 1.75 V vs. RHE being at a longer wavelength compared to that of 1.23 V vs. RHE. This behavior of different onset for the IPCE at the different applied potentials has been documented in hematite which is known to have low hole diffusion lengths.[26]

The IPCE behavior of the films for conditions C and D shows no difference in the onset of IPCE at the difference applied potential. The onset of IPCE in both cases starts at around 450 nm. As discussed earlier, the films in conditions C and D have low photostability. The reduced copper atoms tend to be oxidized and dissolve away during the operation, leaving behind WO_3. Indeed, we believe that the film in conditions C and D dissolved during the IPCE measurement and form WO_3. Since WO_3 has been shown to have a large hole diffusion lengths (around 150 nm),[27] the holes generated in the bulk can diffuse to the surface before the recombination. This results in a much more subtle difference in the IPCE onset at the different applied potential. The onset of

IPCE of these conditions at around 450 nm is also very close to the reported band gap of WO_3 at 2.7-2.8 eV.[6,7]

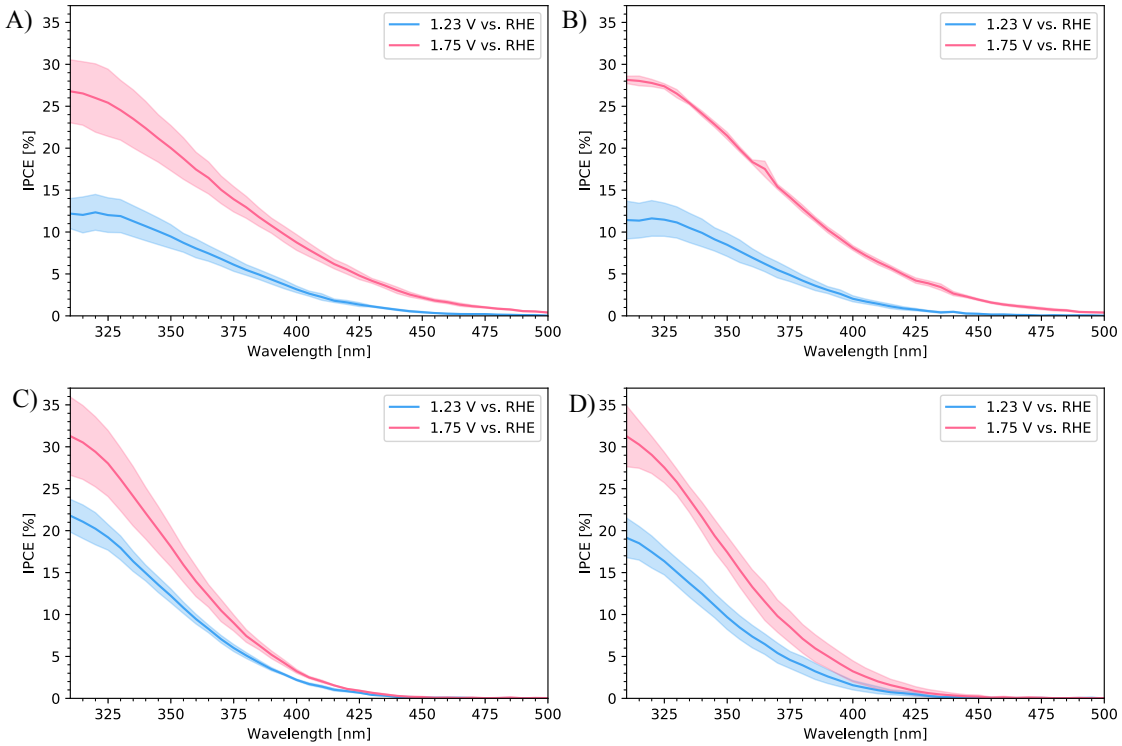

Figure 5.10: Average IPCE at 1.23 and 1.75 V vs. RHE of $CuWO_4$ condition A) A, B) B, C) C and D) D. The value shown here is the average value from three samples per condition. The solid line represents the average value. The shaded area represents the standard deviation of the measurement.

To deepen the understanding of the effect of OV on the photocurrent, we sought to determine η_{sep} and η_{inj} for each condition. Both η_{sep} and η_{inj} can be calculated using the photocurrent in water (with an adequate concentration of supporting electrolyte for a conductivity) and in sacrificial conditions (here, a solution of Na_2SO_3 will be used as a sacrificial agent). Under the sacrificial conditions, η_{inj} is assumed to be 1. With this assumption, the Equation 5.1 can be modified into the two following equations:

$$\eta_{sep} = \frac{J_{PEC,Na_2SO_3}}{J_{Abs}} \tag{5.2}$$

$$\eta_{inj} = \frac{J_{PEC,Water}}{J_{Na_2SO_3}} \tag{5.3}$$

Here, J_{PEC,Na_2SO_3} and $J_{PEC,Water}$ are the photocurrent in Na_2SO_3 solution and in water respectively. J_{Abs} is the theoretical maximum photocurrent. At 2.5 eV, J_{Abs} is shown to be 6.5 $mA.cm^{-2}$.[13] Since the films in conditions C and D are readily converted to WO_3 readily during

photoelectrochemical operations, the investigation into η_{sep} and η_{inj} will only be performed and discussed for the conditions of the films A and B. The chopped-light illumination linear sweep voltammogram of the condition of films A and B under sacrificial conditions is shown in Figure 5.11A. Due to the large dark current from the FTO substrate, the determination of η_{sep} and η_{inj} at 1.75 V vs. RHE cannot be accurately determined using this approach. In order to illustrate the effect of applied potential on both efficiencies, η_{sep} and η_{inj} at 0.8, 0.9, and 1.0 V vs. RHE are also determined. The η_{sep} and η_{inj} increases with an increase in applied potential in both cases (Figure 5.11B and Figure 5.11C, respectively). The η_{sep} of the condition B film is higher than that of the condition A film at all four potentials. The reverse is true for the η_{inj} where condition A film exhibits higher values at all four potentials.

The higher η_{sep} in the condition B film is likely due to the improved bulk conductivity since the increase in the number of OVs has been linked to the increase in bulk conductivity in the literature.[17–20] As for the inferior η_{inj}, Guo and co-workers have reported that an OV causes the formation of surface states which cause recombination that led to a decrease in photocurrent in $CuWO_4$.[16] We suspect that this also applies to our system. Since the photocurrent of the condition A film is higher than that of condition B at 1.23 V vs. RHE (Figure 5.8B), while the trend is reversed at the higher applied potential of 1.75 V vs. RHE (Figure 5.8A), we suspect that the multiplication product of the two parameters ($\eta_{sep} \times \eta_{inj}$) of the condition B is higher than that of condition A at the higher applied potential. To confirm this hypothesis, η_{sep} and η_{inj} at the higher applied potentials needs to be determined. Intensity-modulated photocurrent spectroscopy (IMPS) can probe these two values at higher potentials as this technique does not require the use of a sacrificial conditions. Furthermore, photoelectrochemical impedance spectroscopy (PEIS) can provide information on the density of surface states which may be the result in the inferior η_{inj} in the condition B film. Since this technique can only be applied to a photoelectrode with flat morphology. A set of new films with minimal nanostructuring are needed for this technique. These two techniques will be applied in the future to complete our understanding of the role of OVs in the photocurrent of $CuWO_4$.

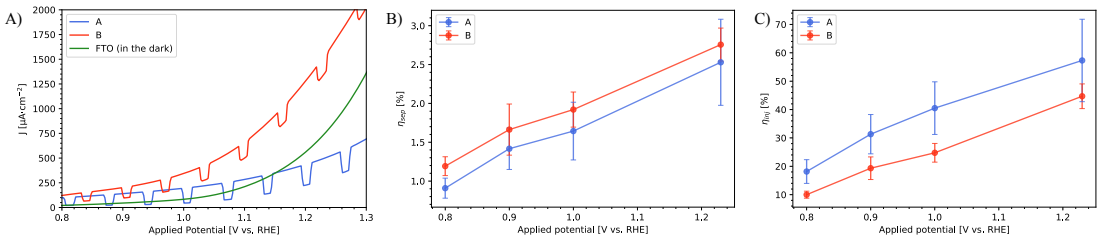

Figure 5.11: A) Chopped-light linear sweep voltammograms of $CuWO_4$ condition A and B and linear sweep voltammogram (in the dark) of an FTO substrate in a sacrificial conditions (1.5 Na_2SO_3 pH 7). Average B) charge separation efficiency (η_{sep}) and C) charge injection efficiency (η_{inj}) of $CuWO_4$ condition A and B at 0.8, 0.9, 1.0 and 1.23 V vs. RHE. The average value comes from three samples.

5.3 Conclusions

In this chapter, the effect of the number of OVs on the physical and photoelectrochemical properties of $CuWO_4$ was investigated. The $CuWO_4$ films were fabricated using sol-gel synthesis. Different numbers of OVs were introduced by subjecting the films to the secondary annealing under H_2/Ar gas mixture for a different duration. The films with a higher number of OVs became darker in color. The absorption in the sub-band gap region ($\lambda > 496$ nm) increased with an increasing number of OVs, but the band gap of the produced films was not affected by the number of OVs and remained constant at 2.5 eV. Films with a higher number of OVs showed a reduction to Cu where Cu(II) atoms were reduced to either Cu(I) or Cu(0), but the oxidation state of W remains constant at +6. The film morphology was not affected by the number of OVs, but crystalline Cu particles with the size ranging from 200-700 nm were formed in the films with a high number of OVs white the percentage of Cu(I)/Cu(0) to the total copper exceeding 50%. The chemical identity of the films as probed by Raman spectroscopy was not affected by the number of OVs, but a reduction in crystallinity was observed with an increasing number of OVs. A moderate number of OVs helped improve the photocurrent at the higher applied potential (1.75 V vs. RHE), but the films with too many OVs had a detrimental effect on the photocurrent. The film with a moderate number of OVs showed improved η_{sep} which could be the result of improved electron conductivity in the bulk. The high number of OVs inflicted detrimental effects on both the photocurrent and the stability. In such films, the reduced copper was easily re-oxidized and leached away from the film, leaving behind WO_3. This work highlights the balance between the benefits and the drawbacks of an OV to $CuWO_4$ photoanode which can provide insight for designing more efficient materials for solar energy conversion.

References

[1] Pyper, K. J.; Evans, T. C.; Bartlett, B. M. Synthesis of α-SnWO4 thin-film electrodes by hydrothermal conversion from crystalline WO3. *Chinese Chemical Letters* **2015**, *26*, 474–478.

[2] Cho, I.-S.; Kwak, C. H.; Kim, D. W.; Lee, S.; Hong, K. S. Photophysical, photoelectrochemical, and photocatalytic properties of novel SnWO4 oxide semiconductors with narrow band gaps. *The Journal of Physical Chemistry C* **2009**, *113*, 10647–10653.

[3] Zhu, Z.; Sarker, P.; Zhao, C.; Zhou, L.; Grimm, R. L.; Huda, M. N.; Rao, P. M. Photoelectrochemical properties and behavior of α-SnWO4 photoanodes synthesized by hydrothermal conversion of WO3 films. *ACS Applied Materials & Interfaces* **2017**, *9*, 1459–1470.

[4] Khader, M. M.; Saleh, M. M.; El-Naggar, E. M. Photoelectrochemical characteristics of ferric tungstate. *Journal of Solid State Electrochemistry* **1998**, *2*, 170–175.

[5] Abdi, F. F.; Chemseddine, A.; Berglund, S. P.; van de Krol, R. Assessing the suitability of iron tungstate (Fe2WO6) as a photoelectrode material for water oxidation. *The Journal of Physical Chemistry C* **2017**, *121*, 153–160.

[6] Kang, D.; Kim, T. W.; Kubota, S. R.; Cardiel, A. C.; Cha, H. G.; Choi, K.-S. Electrochemical synthesis of photoelectrodes and catalysts for use in solar water splitting. *Chemical reviews* **2015**, *115*, 12839–12887.

[7] González-Borrero, P.; Sato, F.; Medina, A.; Baesso, M. L.; Bento, A. C.; Baldissera, G.; Persson, C.; Niklasson, G. A.; Granqvist, C. G.; Ferreira da Silva, A. Optical band-gap determination of nanostructured WO 3 film. *Applied Physics Letters* **2010**, *96*, 061909.

[8] Yourey, J. E.; Bartlett, B. M. Electrochemical deposition and photoelectrochemistry of CuWO4, a promising photoanode for water oxidation. *Journal of materials chemistry* **2011**, *21*, 7651–7660.

[9] Pourbaix, M. Atlas of electrochemical equilibria in aqueous solution. *NACE* **1974**, *307*.

[10] Gaillard, N.; Chang, Y.; DeAngelis, A.; Higgins, S.; Braun, A. A nanocomposite photoelectrode made of 2.2 eV band gap copper tungstate (CuWO4) and multi-wall carbon nanotubes for solar-assisted water splitting. *International journal of hydrogen energy* **2013**, *38*, 3166–3176.

[11] Augustynski, J.; Solarska, R.; Hagemann, H.; Santato, C. Nanostructured thin-film tungsten trioxide photoanodes for solar water and sea-water splitting. Solar Hydrogen and Nanotechnology. 2006; pp 136–144.

[12] Lhermitte, C. R.; Bartlett, B. M. Advancing the chemistry of CuWO4 for photoelectrochemical water oxidation. *Accounts of chemical research* **2016**, *49*, 1121–1129.

[13] Lee, D. K.; Lee, D.; Lumley, M. A.; Choi, K.-S. Progress on ternary oxide-based photoanodes for use in photoelectrochemical cells for solar water splitting. *Chemical Society Reviews* **2019**, *48*, 2126–2157.

[14] Corby, S.; Rao, R. R.; Steier, L.; Durrant, J. R. The kinetics of metal oxide photoanodes from charge generation to catalysis. *Nature Reviews Materials* **2021**, *6*, 1136–1155.

[15] Govindaraju, G. V.; Wheeler, G. P.; Lee, D.; Choi, K.-S. Methods for electrochemical synthesis and photoelectrochemical characterization for photoelectrodes. *Chemistry of Materials* **2017**, *29*, 355–370.

[16] Guo, W.; Wang, Y.; Lian, X.; Nie, Y.; Tian, S.; Wang, S.; Zhou, Y.; Henkelman, G. Insights into the multiple effects of oxygen vacancies on CuWO 4 for photoelectrochemical water oxidation. *Catalysis Science & Technology* **2020**, *10*, 7344–7351.

[17] Tang, Y.; Rong, N.; Liu, F.; Chu, M.; Dong, H.; Zhang, Y.; Xiao, P. Enhancement of the photoelectrochemical performance of CuWO4 films for water splitting by hydrogen treatment. *Applied Surface Science* **2016**, *361*, 133–140.

[18] Guo, W.; Duan, Z.; Mabayoje, O.; Chemelewski, W. D.; Xiao, P.; Henkelman, G.; Zhang, Y.; Mullins, C. B. Improved Charge Carrier Transport of Hydrogen-Treated Copper Tungstate: Photoelectrochemical and Computational Study. *Journal of The Electrochemical Society* **2016**, *163*, H970.

[19] Hu, D.; Diao, P.; Xu, D.; Xia, M.; Gu, Y.; Wu, Q.; Li, C.; Yang, S. Copper (II) tungstate nanoflake array films: sacrificial template synthesis, hydrogen treatment, and their application as photoanodes in solar water splitting. *Nanoscale* **2016**, *8*, 5892–5901.

[20] Ma, Z.; Linnenberg, O.; Rokicinska, A.; Kustrowski, P.; Slabon, A. Augmenting the photocurrent of CuWO4 photoanodes by heat treatment in the nitrogen atmosphere. *The Journal of Physical Chemistry C* **2018**, *122*, 19281–19288.

[21] Corby, S.; Francàs, L.; Kafizas, A.; Durrant, J. R. Determining the role of oxygen vacancies in the photoelectrocatalytic performance of WO 3 for water oxidation. *Chemical science* **2020**, *11*, 2907–2914.

[22] Biesinger, M. C. Advanced analysis of copper X-ray photoelectron spectra. *Surface and Interface Analysis* **2017**, *49*, 1325–1334.

[23] Pauly, N.; Tougaard, S.; Yubero, F. Determination of the Cu 2p primary excitation spectra for Cu, Cu2O and CuO. *Surface science* **2014**, *620*, 17–22.

[24] Wu, C.-K.; Yin, M.; O'Brien, S.; Koberstein, J. T. Quantitative analysis of copper oxide nanoparticle composition and structure by X-ray photoelectron spectroscopy. *Chemistry of materials* **2006**, *18*, 6054–6058.

[25] Lima, A.; Costa, M.; Santos, R.; Batista, N.; Cavalcante, L.; Longo, E.; Luz Jr, G. Facile preparation of CuWO4 porous films and their photoelectrochemical properties. *Electrochimica Acta* **2017**, *256*, 139–145.

[26] Kay, A.; Cesar, I.; Grätzel, M. New benchmark for water photooxidation by nanostructured α-Fe2O3 films. *Journal of the American Chemical Society* **2006**, *128*, 15714–15721.

[27] Zheng, G.; Wang, J.; Liu, H.; Murugadoss, V.; Zu, G.; Che, H.; Lai, C.; Li, H.; Ding, T.; Gao, Q., et al. Tungsten oxide nanostructures and nanocomposites for photoelectrochemical water splitting. *Nanoscale* **2019**, *11*, 18968–18994.

Chapter 6

Conclusions and Outlook

6.1 Biomass valorization using WO_3 photoanode

In chapter 2-4, we demonstrated the capability of WO_3 photoanode to perform an alternative oxidation reaction to the OER and proposed a facile technique to predict the selectivity of the competing reaction in photoelectrochemical cells using only the information from linear sweep voltammogram. In chapter 2, we demonstrated the direct oxidation of HMF to DFF and subsequently, FDCA using a WO_3 photoanode. The transformation can be achieved directly without any need for a catalyst or a redox mediator. The transformation results in the maximum yield of DFF and FDCA of 4% and 0.5% respectively. A kinetics model was used to understand the cause of the observed low yield. The model suggested the presence of competing degradation reactions in each step of the transformation which resulted in a low final FDCA yield. To deepen the understanding and to control the selectivity of multiple competing reactions in photoelectrochemical cells, we developed a $\partial J/\partial E$ analysis, a facile technique capable of predicting the selectivity of the competing reactions using the information readily obtained from LSV. In chapter 3, we employed this analysis and demonstrated the dependency of the applied potential to the selectivity of HMF oxidation over the OER on WO_3 as predicted by the $\partial J/\partial E$ analysis. We believe that this analysis can be applied to other systems employing photoelectrochemical cells to perform alternative oxidation or reduction reactions. In chapter 4, we discussed the decoration of electrocatalyst onto the surface of WO_3 to improve the FDCA yield. The introduction of MnO_x, a proven-effective electrocatalyst for HMF oxidation, onto the WO_3 surface led to a reduction in the photocurrent without improving the FDCA yield. We believe that MnO_x acts as a recombination center and hence is not compatible with WO_3. We showed that TEMPO, a redox mediator used in HMF oxidation, can also be easily

anchored onto the electrode surface via a non-covalent modification with the help of Nafion®. Nevertheless, the TEMPO/Nafion® modified Nafion suffers low stability from TEMPO leaching. Another promising organic electrocatalyst for alcohol and aldehyde oxidation, NHPI, was also tested for the catalytic activity for HMF oxidation. However, we found that this molecule shows no catalytic activity toward the oxidation of HMF.

The works demonstrated in these chapters have laid down the road for the possibility of turning a weak point of WO_3 in having poor selectivity for the OER into an advantage point in performing alternative oxidation reactions, in particular HMF oxidation. Moving forward, it is clear that the use of an electrocatalyst is required to improve the FDCA yield. The ideal electrocatalyst for this task not only has to process good catalytic activity toward HMF oxidation but also must be stable under acidic conditions and not act as a recombination center when decorated onto the surface of WO_3. A deeper understanding of the mechanism of HMF oxidation at the surface of WO_3 may shed some light on why the degradation reaction is preferred over the oxidation to FDCA. A study employing operando techniques such as surface-enhanced Raman spectroscopy may provide some insight into the interaction between the HMF molecule and the surface of WO_3. A theoretical study employing DFT calculation can reveal possible pathways which lead to FDCA and to the degradation reactions. Understanding these pathways could guide us to the strategy to promote oxidation to FDCA and reduce the undesired degradation reactions. In addition to this, many of the products from the HMF oxidation (discussed in chapter 2) remains unidentifiable. One of these products might be a useful compound. Further characterization may help identify these products.

6.2 Effects of oxygen vacancies to the photoelectrochemical properties of copper tungstate photoanode

At the end of this thesis, we expanded our study from WO_3 to $CuWO_4$, a metal tungstate-based ternary oxide that retains multiple advantages of WO_3, such as the acid stability, but with a lower band gap. In chapter 5, the effect of oxygen vacancies on the photocurrent of $CuWO_4$ was investigated. A set of four $CuWO_4$ electrodes with different numbers of OV were fabricated. We demonstrated that the increase in the number of OVs can improve the photocurrent of the $CuWO_4$ electrode by improving η_{sep}. However, an excessive number of OV post detrimental effects on the photocurrent. We found that if more than 50% of Cu is reduced, the reduced Cu will agglomerate to form Cu(0) at the surface of the electrode with a size ranging from 200-700 nm. The over-reduced $CuWO_4$ has poor stability during the photoelectrochemical measurement due to the dissolution of

Cu which leaves behind WO_3. Our finding shed the light on the upper limit of the use of OV as a dopant to improve the photocurrent in $CuWO_4$ photoanodes.

Moving forward, η_{inj} and η_{sep} are crucial to understanding the effect of OV on the photocurrent. As discussed earlier, the determination of these two values under sacrificial conditions is limited at the low applied potential region due to the large dark current from the FTO substrate. Another technique to determine these two values is IMPS. Since this technique can be performed directly in a non-sacrificial condition, it has the potential to determine η_{inj} and η_{sep} at the higher applied bias (especially at 1.75 V vs. RHE). This added information will complete our understanding of the effect of OV on the charge separation in the bulk and charge injection at the surface. Another technique that can give more insight into our system is EIS. This technique can help probe the doping concentration, which affects the electron conductivity in the bulk. The difference in bulk conductivity can further explain the reason for the improved η_{sep} of the film in condition B. Lastly, the information on the free charge carrier lifetime and the hole diffusion length can complement our understanding of how OV affects η_{inj} and η_{sep}. Transient absorption spectroscopy (TAS) can help probe these values. Since OV is a common dopant in many metal oxide materials, we believe that this study can provide a foundation to the study on the effects of OV in other materials.

Appendix A

Supporting Information to Chapter 2

A.1 Experimental details

A.1.1 Synthesis of WO_3 electrodes on FTO coated glass

WO_3 electrodes were synthesized using a previously reported sol-gel deposition method.[1,2] To prepare the electrodes, 10 mmol (3.29 g) of sodium tungstate dihydrate was dissolved in 20 mL deionized water and run through a Dowex ion exchange column that had been acidified previously with 6 M HCl and rinsed back to pH 7 with Milli-Q water. A yellow solution was eluted into in a round-bottom flask containing 20 mL absolute ethanol while stirring. The resulting transparent yellow solution (tungstic acid) was concentrated on a rotary evaporator until the final volume was approximately 20 mL, at which time 6.6 g PEG-300 (TCI, lot. UP2XKAA, d 1.13) was added as a stabilizer. At this point, the solution was significantly more viscous and had a cloudy yellowish colour. The suspension was kept stirring constantly at 1200 rpm on a stir plate and used for up to 3 days. Over time the solution's colour turned dark green. However, this colour change did not appear to affect the consistency or quality of the resulting electrodes. WO_3 electrodes were synthesized by dropping 190 μL of the suspension onto clean 2.5 $\times$ 2.5 cm^2 FTO glass substrate (Solaronix) and spinning at 2500 rpm using a Laurel spin coater (Model WS-650MZ-23NPPB) for 30 seconds, followed by annealing the electrodes in a muffle furnace preheated to 500 °C for 30 minutes in air. A small section at the bottom of the electrode was masked with electrical tape to allow for an electrical contact. The spinning and annealing process was repeated ten times to

obtain electrodes of sufficient thickness (ca. 2 μm).

A.1.2 Synthesis of $BiVO_4$ electrodes on FTO glass

$BiVO_4$ electrodes were prepared using our previously reported spin coating technique.[3] Thin films of $BiVO_4$ were prepared by annealing a spin-coated solution of EDTA–metal complexes. To prepare the precursor solution, EDTA (36.53 g, 2 eq.) was added to 18.2 MΩ resistance water (100 mL, Millipore). A small amount of NH_4OH (12.5 mL) was added to partially deprotonate the EDTA, and ensure its dissolution. After the EDTA had dissolved, $Bi(NO_3)_3{\cdot}5H_2O$ (30.316 g, 1 eq.) was added. Upon contact with the solution, the solid formed a white cake, which slowly dissolved over time. Once the solid had completely dissolved, VO(AcAc) (16.57 g, 1 eq.) was added. To aid the dissolution of the blue powder, additional water was added, and the solution was heated to 60 °C and left to stir for 1 h. After the solid had completely dissolved, the solution was left to cool. Once at room temperature, the pH was measured and adjusted to 5, if necessary, by using dilute HNO_3 or NH_4OH. The final volume was adjusted to 250 mL by adding more water. The final concentrations of Bi, V, and EDTA were 0.25 m, 0.25 m, and 0.5 m, respectively. $BiVO_4$ thin films were synthesized by spin coating the previously precursor solution. The spin coating was accomplished using a Laurell model WS-650MZ-23NPPB spin coater. For this, the substrate was first spun at 4500 RPMs, then 0.75 mL of the solution was dispensed on top. The electrode was kept spinning for 45 s after the solution was dispensed. Following the spin coating, the electrodes were calcined at 400 °C in an air atmosphere to burn off all the organic material. After repeating the spin-coating/calcining cycles enough times to obtain electrodes of the desired thickness, the electrodes were annealed at 550 °C for 1 h.

A.1.3 Synthesis of Fe_2O_3

Hematite thin films were prepared using a previously reported hydrothermal/annealing technique.[4] Fluorine doped tin oxide (FTO)coated glass substrates (Solaronix TCO10-10, 8 Ω/sq.) were vertically positioned in a sealed glass bottle containing 1 M sodium nitrate ($NaNO_3$, 99+ %, Acros) and 0.15 M iron chloride hexahydrate ($FeCl_3{\cdot}6H_2O$, 99+ %, Acros) aqueous solution. The glass bottle was placed in an oven (Memmert UF 30 plus) for 3 h at 100°C. During the heating process, β-FeOOH nanorods formed on the FTO surface. After the heating the β-FeOOHfilms were rinsed with high purity water (18.2 MΩ cm, Synergy), and finally they were annealed in a preheated tube furnace (MTI OTF-1200X-S) at 800 °C for 15 min to convert the β-FeOOH to Fe_2O_3.

A.1.4 Preparation of Electrolyte solutions

0.1 M NaP_i solutions were prepared by weighing 9.8 g of H_3PO_4 in a 2 L beaker. The acid was then diluted to a volume of 1,000 mL by slowly adding Millipore water (18 MΩ cm). The solution pH was then adjusted to 4 using a pH meter and adding in a concentrated solution of NaOH.

A.1.5 Standard Electrochemical Measurements

All electrochemical measurements were collected using a BioLogic SP-200 potentiostat in a three-electrode configuration. Unless noted otherwise, the working, counter, and reference electrodes were WO_3, a Pt wire, and Ag/AgCl in saturated KCl. A buffered aqueous solution of 0.1 M NaP_i at pH 4 was used as the electrolyte. All LSV experiments were performed at a scan rate of 20 mV/s. Unless noted otherwise, the illumination intensity was equivalent to 1 sun. The illumination direction for all experiments was from the back (glass) side.

A.1.6 Extended-duration photo-oxidation experiments

Bulk-electrolysis experiments were performed in a custom-built two-sided cell (3D printed from Polyethylene terephthalate). The cell was composed of two compartments, which were separated by a Nafion membrane (N-115 membrane, 0.125 mm thick). The membrane was required to prevent the diffusion of oxidised products to the counter electrode, where they could be reduced. The WO_3 photoelectrode, and Ag/AgCl reference electrode were contained in the working electrode compartment. The Pt wire was kept in the counter electrode compartment. The electrolyte solution used was 100 mL of 5 mM HMF in 0.1 M NaP_i buffer, for the working electrode compartment, and 0.1 M NaP_i buffer for the counter electrode compartment (also 100 mL). To eliminate potential diffusion limitations, the solution was kept stirring throughout the experiment using a magnetic stir bar. For the bulk electrolysis experiment, the current produced by the WO_3 photoelectrode was measured over 64 hours at an applied potential of 0.683 V vs. RHE. The illumination intensity used was equivalent to 3 suns, and the electrodes were illuminated from the back (glass) side. The active area of the WO_3 photoelectrode was ca. 2.5 cm^2. Three runs of 64 h were completed and the data averaged.

A.1.7 Oxidation products quantification

Product quantification during the bulk electrolysis experiment was performed using an HPLC coupled to a UV-Vis spectrometer (Shimadzu Prominence LC-20AP HPLC, equipped with dual

UV-Vis detector set at 255 and 285 nm). 600 μL aliquots were taken before, during and after the photo-oxidation experiment. Sulfuric acid (5 mM) was used as the mobile phase in the isocratic mode. An equilibration time of 30 minutes was required before the first injection. The flow rate was 0.5 mL min^{-1} at 40 °C . The samples were injected through polytetrafluoroethylene hydrophilic filter (0.22 μM pore size) into a Coregel 87H3 7.8 $\times$ 300 mm column (part number CON-ICE-99-9861) that was purchased from BGB Analytik AG in Switzerland. The product identification and quantification were determined from calibration curves from the known standards. The retention times for HMF, DFF, HMFCA, FFCA and FDCA were 42.2, 53.2, 27.7, 29.6 and 21.1 minutes respectively.

A.1.8 Microscopy, XRD and Raman Spectroscopy

SEM data was collected using a Zeiss Gemini 300 scanning electron microscope in HV mode. XRD data was collected using a Panalytical Empyrean system (Theta-Theta, 240 mm) equipped with a PIXcel-1D detector, Bragg-Brentano beam optics (including hybrid monochromator) and parallel beam optics. Raman spectra were obtained with a LabRam spectrometer (Jobin Yvon Horiba). The excitation line was provided by an Ar laser (532.19 nm).

A.1.9 Materials

The following chemicals were used as received without further purification. HMF (99%), DFF (97%), and ammonium meta tungstate were purchased from Sigma-Aldrich. $NaWO_4$ (99%) and Dowex™ 50WX2, 100-200 mesh were purchased from Acros Organics. HMFCA was obtained from Apollo Scientific. Nafion™ membrane was obtained from Alfa Aesar. FFCA (95%) was purchased from ABCR. FDCA (97%) was purchased from fluorochem.

A.2 Characterization of WO_3

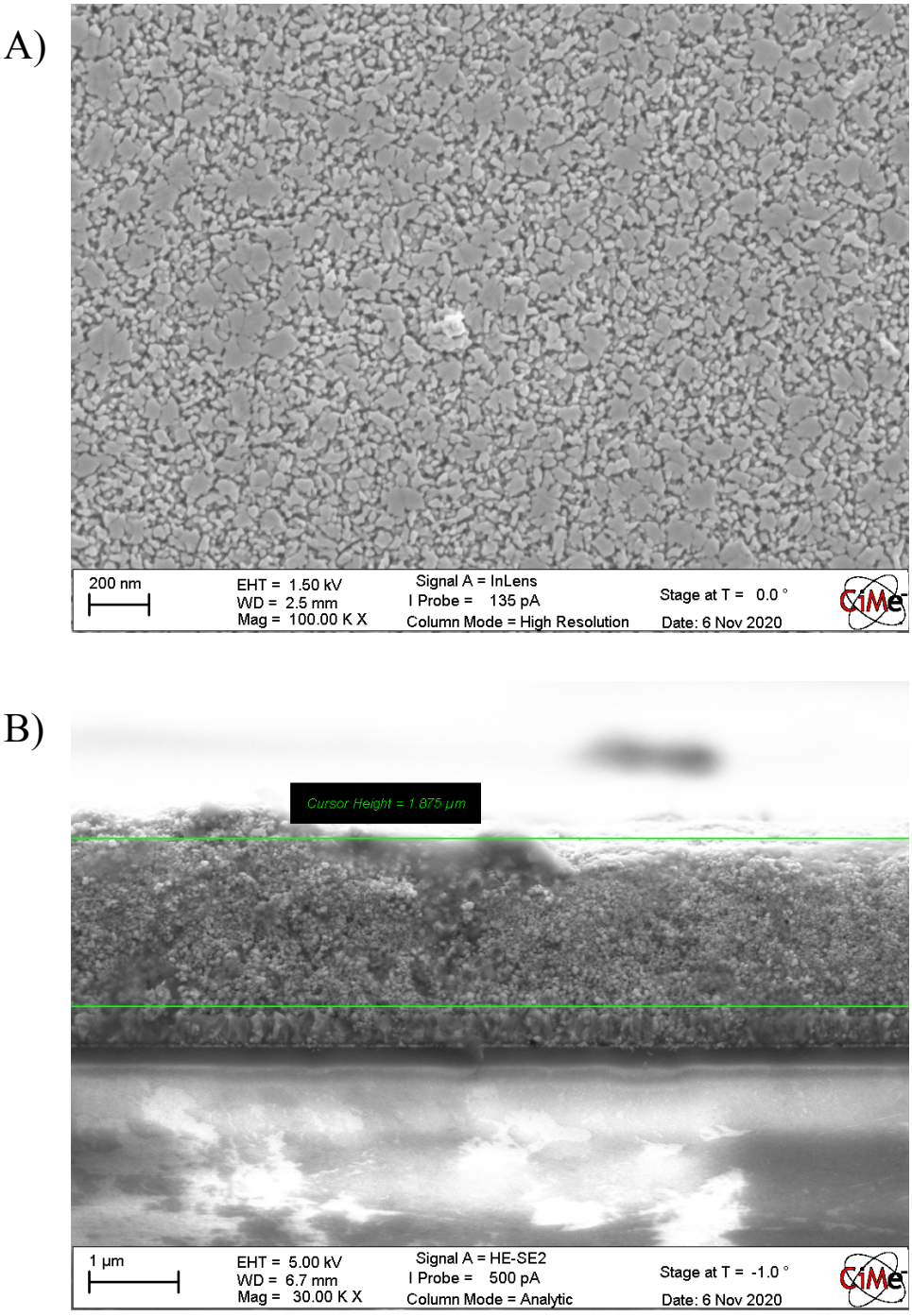

Figure A.1: SEM images of WO_3 on FTO in A) top view and B) cross-section view illustrating the film thickness of 1.875 μm

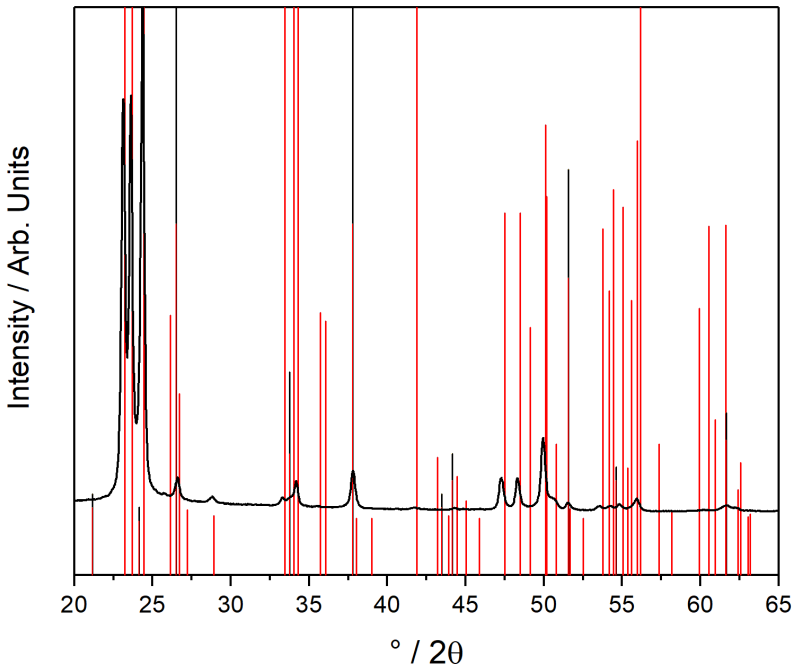

Figure A.2: XRD spectrum of WO_3 film (black trace) with the reference spectrum (red line)

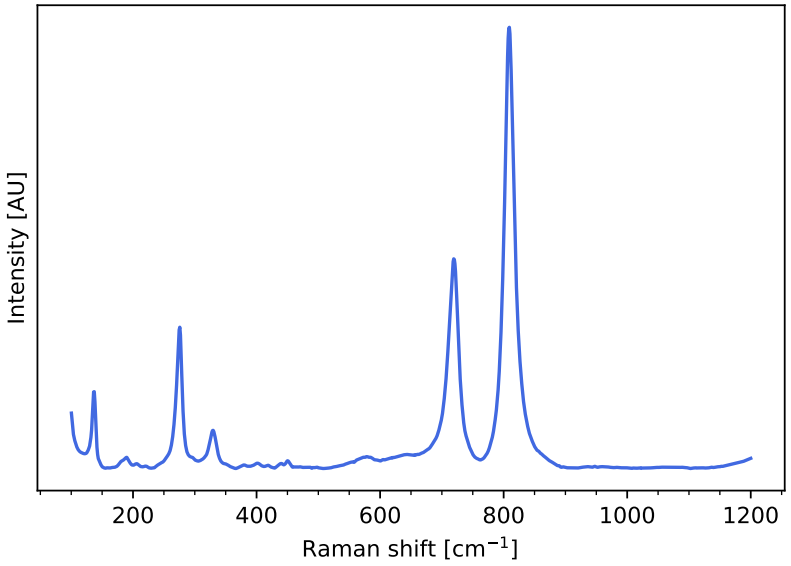

Figure A.3: Raman spectrum of WO_3 film

A.3 Chemical kinetics model and rate constant fit

The kinetic modelling and fitting were performed using a custom Python script. The source code is hosted on Github: https://github.com/flboudoire/chemical-kinetics and its documentation can be found here: https://chemical-kinetics.readthedocs.io/en/latest. Firstly, it was necessary to

make a few approximations. We suppose that all the reactions presented are pseudo first order. Davis and co-workers have demonstrated that this is a reasonable assumption.[2] In their work, they studied the mechanism of HMF oxidation and demonstrated that it proceeds through oxidations at the alcohol and aldehyde moieties, which are first order reactions. Additionally, we assumed that the reductive reverse reactions are negligible since we are operating at a high forward bias. Due to the presence of a significant electric field at the electrode surface, the WO_3 surface will be depleted of electrons, and thus little to no reductive currents due to the reverse reaction will be possible under these conditions. According to the law of mass action the rates of concentration change for the reaction of a species A at the photoelectrode surface with two holes at the WO_3 / electrolyte interface to give a product B can be written, in general, as follows:

$$\frac{d[A]_{\text{surf}}}{dt} = -k[h]^2[A]_{\text{surf}} \tag{A.1}$$

$$\frac{d[B]_{\text{surf}}}{dt} = k[h]^2[A]_{\text{surf}} \tag{A.2}$$

Where $[A]_{\text{surf}}$ and $[B]_{\text{surf}}$ are the concentrations of A and B in the electrolyte at the surface of WO_3, [h] is the concentration (activity) of holes available at the surface, and k is the (true) reaction rate constant. To simplify these equations, we consider that the reactions are under kinetic control and the hole concentration at the surface is in excess and therefore can be considered constant. This is justified by the fact that we operate at a potential where the photocurrent for HMF oxidation is close to saturation (see Figure A.6). We also measured a significant drop in photocurrent if the solution was not stirred (see Figure A.7), further proving that the reactions not limited by [h] but rather the concentration of the molecular reactant at the surface.

We also consider that the species concentrations measured in the bulk of the solution change in the same proportion as the species concentration at the surface of the electrode. This hypothesis is supported by their similar molecular size, hence reasonably similar and constant mass transfer coefficients, k_m. Considering these hypotheses, equations A.1 and A.2 can be rewritten with $k' \approx k[h]^2$, and $[A]_{\text{surf}} \approx (k_m/(1+k_m))\ [A]_{\text{solution}}$ as follows:

$$\frac{d[A]_{\text{solution}}}{dt} = -k'[A]_{\text{solution}} \tag{A.3}$$

$$\frac{d[B]_{\text{solution}}}{dt} = k'[A]_{\text{solution}} \tag{A.4}$$

In this case, considering the reactions proposed in Figure 2.2c, the system of differential equations that model the concentrations measured in solution (Figure 2.2B) are written as follows:

$$\frac{d[HMF]}{dt} = -(k_{11} + k_{12} + k_{B1})[HMF] \tag{A.5}$$

$$\frac{d[DFF]}{dt} = k_{11}[HMF] - (k_{21} + k_{B21})[DFF] \tag{A.6}$$

$$\frac{d[HMFCA]}{dt} = k_{12}[HMF] - (k_{22} + k_{B22})[HMFCA] \tag{A.7}$$

$$\frac{[FFCA]}{dt} = k_{21}[DFF] + k_{22}[HMFCA] - (k_3 + k_{B3})[FFCA] \tag{A.8}$$

$$\frac{[FDCA]}{dt} = k_3[FFCA] - k_{B4}[FDCA] \tag{A.9}$$

$$\frac{d[B]}{dt} = k_{B1}[HMF] + k_{B21}[DFF] + k_{B22}[HMFCA] + k_{B3}[FFCA] + k_{B4}[FDCA] - k_b[B] \tag{A.10}$$

$$\frac{d[B^*]}{dt} = k_b[B] \tag{A.11}$$

With this model, we can extract quantitative reaction rate constants for all the intermediate reactions leading to the formation of FDCA. We can also characterize the speculated formation of oxidized by-products (B) and their further oxidation to B^*. We also simultaneously model the amount of charge passed during the course of the reaction (Figure 2.2A). This current data represents a sum of contributions from all species formed during the photoelectrochemical oxidation of HMF. The following equation is used to model the evolution of passed charge over time:

$$Q = qN_AV\sum_i n_iC_i \tag{A.12}$$

With Q being the total amount of charge passed, q the electron charge (1.6×10^{-19} C), N_A Avogadro's number (6.02×10^{23}), V the volume of solution (100 mL in our case), n_i the amount of charge passed to make one molecule of species i, and C_i is the concentration of species i. Numerically solving the set of differential equations (Equations A.5 - A.12) and using a least-square fit algorithm

with the experimental data, the numerical solution, and Equation A.12 we can extract a set of eleven rate constants that fit the behaviour observed in Figure 2.2A and Figure 2.2B. The main discrepancy is in the predicted DFF concentration over time for our model, which underestimates the experimental value. This suggests that our model slightly underestimates the value of k_{11}.

A.4 Supplementary figures and tables

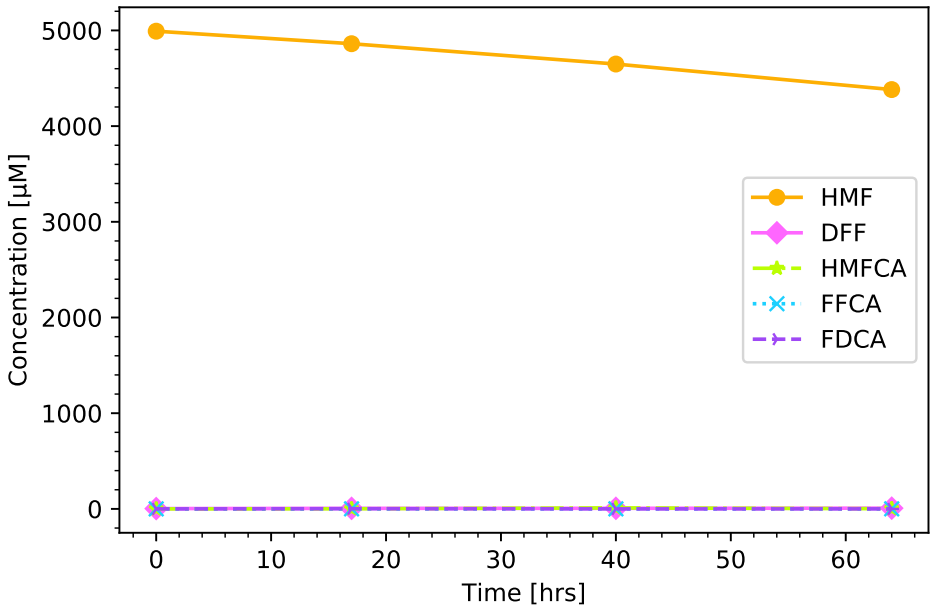

Figure A.4: Concentration of HMF, DFF, FFCA, HMFCA, and FDCA over time. For this experiment a 5 mM solution of HMF in 0.1 M pH 4 NaP_i was irradiated with simulated 3 Suns.

	Concentration [μM]			
Compound	**0 h**	**17 h**	**40 h**	**64 h**
HMF	4992	4861	4649	4382
DFF	3	6	6	8
HMFCA	0	1	0	2
FFCA	0	1	0	1
FDCA	0	0	0	0

Table A.1: Concentration of HMF, DFF, FFCA, HMFCA, and FDCA over time of the control experiment (Figure A.4)

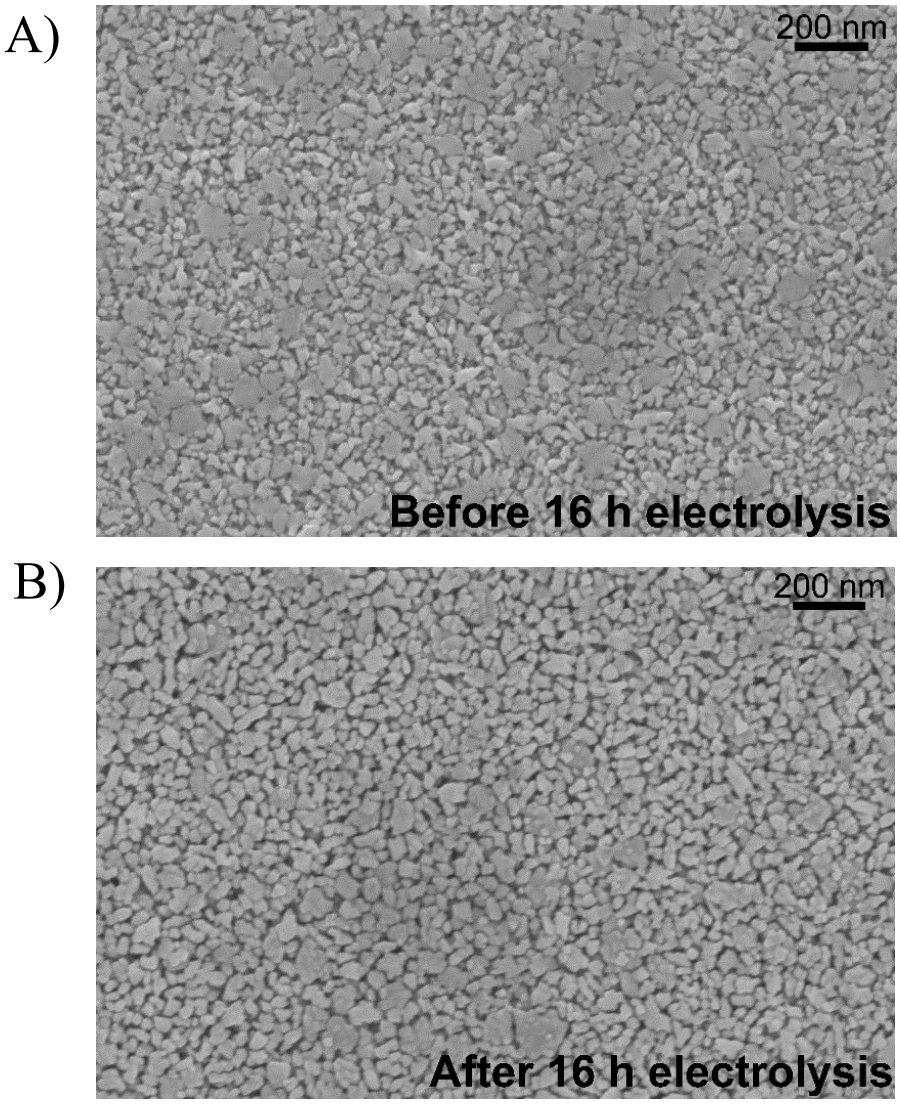

Figure A.5: SEM images of a WO_3 electrode (A) before, and (B) after a 16 hrs bulk electrolysis experiment. This time frame was selected since it was after the largest observed photocurrent decrease. The bulk electrolysis experiment was performed at 0.683 V vs. RHE under simulated 3 suns illumination in a pH 4 0.1 M NaP_i solution which contained 5 mM HMF.

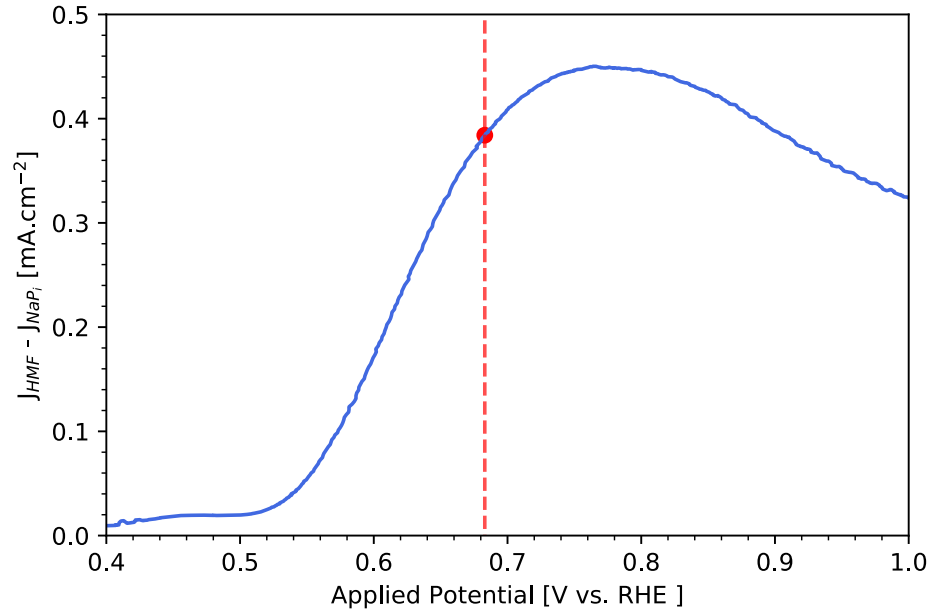

Figure A.6: Difference between the LSV with and without HMF under 3 suns in pH 4 NaP_i solution. The vertical line depicts the photocurrent density at the applied bias used in the bulk electrolysis experiments.

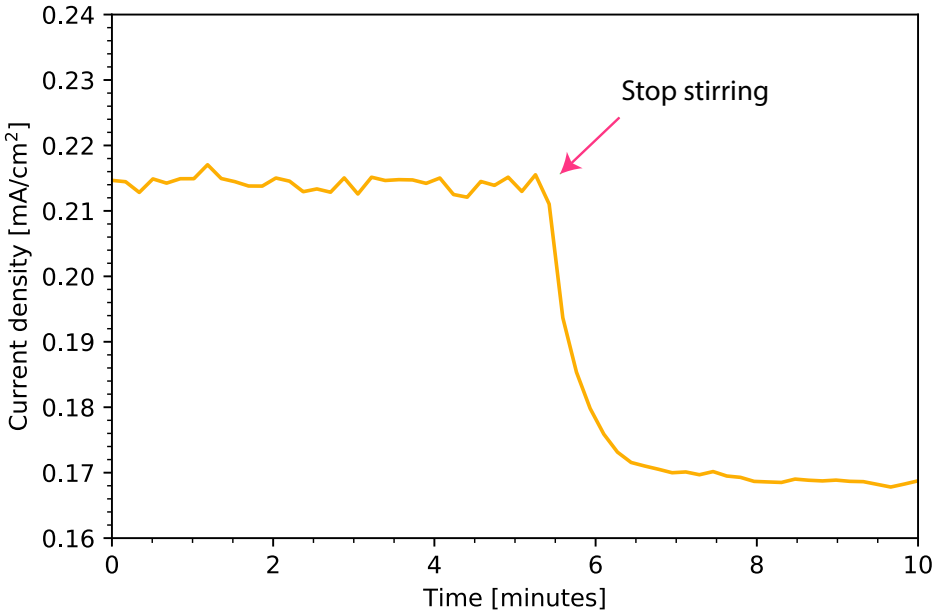

Figure A.7: Chronoamperometry of HMF oxidation on WO_3 under simulated 3 suns in pH 4 NaP_i solution showing the impact of stirring the solution on the photocurrent.

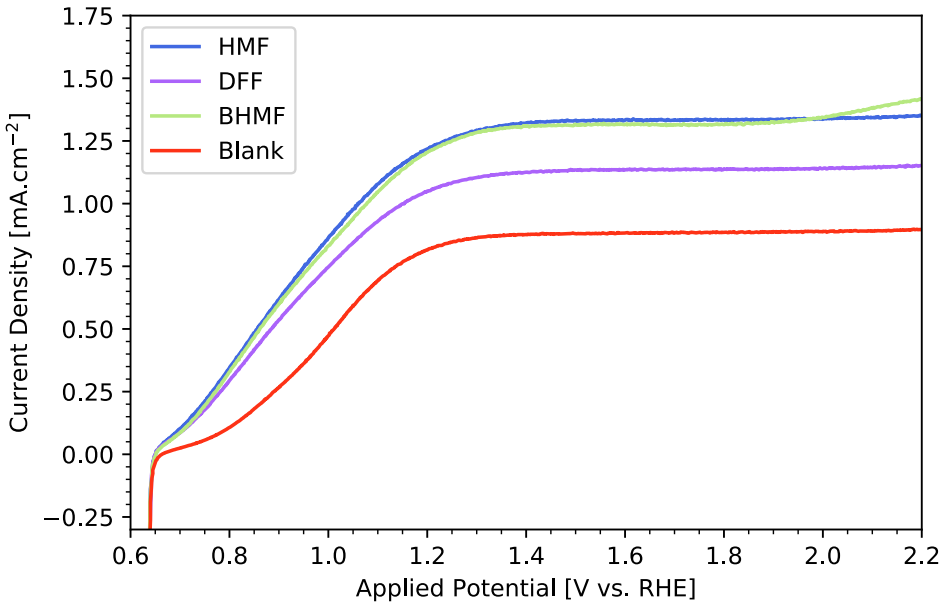

Figure A.8: LSVs of WO_3 electrodes under simulated 1 sun illumination in solutions containing 5 mM HMF, 5 mM DFF, 5 mM BHMF, and a blank control solution. All solutions were prepared using 0.1 M NaP_i buffered to pH 4.

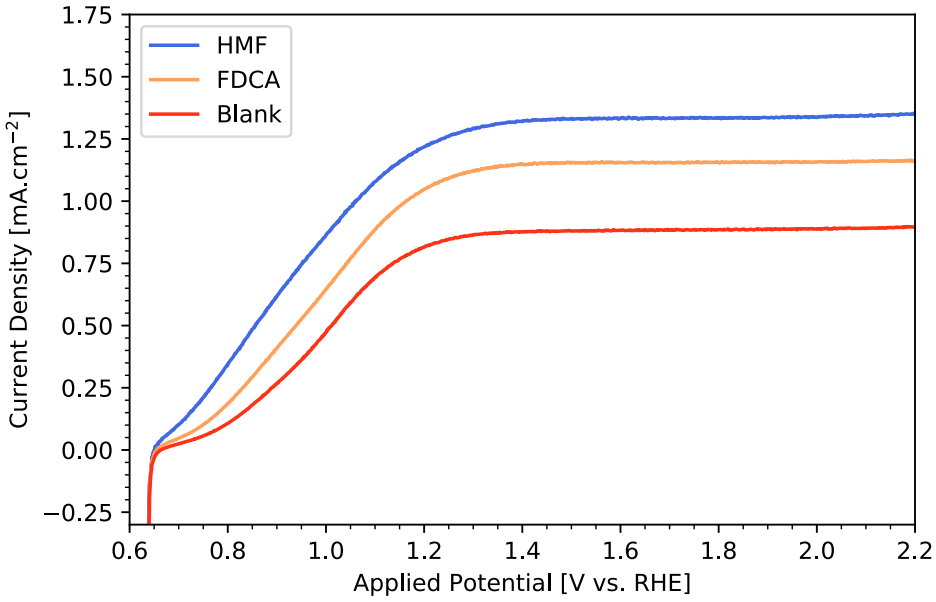

Figure A.9: LSVs of WO_3 electrodes under simulated 1 sun illumination in solutions containing 5 mM HMF, 5 mM FDCA, and a blank control solution. All solutions were prepared using 0.1 M NaP_i buffered to pH 4.

References

[1] Santato, C.; Odziemkowski, M.; Ulmann, M.; Augustynski, J. Crystallographically Oriented Mesoporous WO3 Films: Synthesis, Characterization, and Applications. *Journal of the American Chemical Society* **2001**, *123*, 10639–10649.

[2] Lhermitte, C. R.; Verwer, J. G.; Bartlett, B. M. Improving the stability and selectivity for the oxygen-evolution reaction on semiconducting WO_3 photoelectrodes with a solid-state FeOOH catalyst. *Journal of Materials Chemistry A* **2016**, *4*, 2960–2968.

[3] Lhermitte, C. R.; Polo, A.; Yao, L.; Boudoire, F. A.; Guijarro, N.; Sivula, K. Generalized Synthesis to Produce Transparent Thin Films of Ternary Metal Oxide Photoelectrodes. *ChemSusChem* **2020**, *n/a*, Publisher: John Wiley & Sons, Ltd.

[4] Liu, Y.; Le Formal, F.; Boudoire, F.; Guijarro, N. Hematite Photoanodes for Solar Water Splitting: A Detailed Spectroelectrochemical Analysis on the pH-Dependent Performance. *ACS Appl. Energy Mater.* **2019**, *2*, 6825–6833.

Appendix B

Supporting Information to Chapter 3

B.1 Experimental details

The detail for the fabrication, characterization of the WO_3 electrode, the standard electrochemical measurement and the product quantification procedure were discussed in the experimental section in Chapter 2.

B.2 Mathematical foundation of the fit $\partial J/\partial E$

The mathematical expression used to create our fitting functions are modified from the published work by Z. Wang et al.[1] and R. Memming et al.[2].

Consider Gericher's model for electron transfer in semiconductor[2]

$$Rate\,of\,electron\,transfer\, = \int \kappa.f(E).DOS(E).D_{red}(E)dE \tag{B.1}$$

where:

κ = electron transfer coefficient

$f(E)$ = Fermi-Dirac distribution function

$D_{red}(E)$ = Density of state of the reduced species in the solution.

E = Applied potential

In our condition, the following assumptions can be assumed:

1. $f(E)$ can be assumed to be constant as we constantly move the $E_{f,p}$ by sweeping the applied potential
2. $D_{red}(E)$ can be assumed to be constant. $D_{red}(E)$ in our experiment is the concentration of HMF at the surface of the electrode. We demonstrate in Figure B.2 that our system is not mass transport limited. Hence, we can assumed that the concentration of HMF at the surface is in excess in comparison to the available holes at the surface. Hence, $D_{red}(E) \gg DOS(E)$, and $D_{red}(E)$ can be assumed to be constant.
3. The rate of electron transfer = photocurrent (J)

Applying the three assumptions to **Equation B.1** gives:

$$J = \kappa.f.D_{red} \int DOS(E)dE$$

Differentiate both sides of the equation with respective to E gives:

$$\frac{\partial J}{\partial E} = \kappa.f.D_{red} \times DOS(E)$$

As κ, f and D_{red} are all constant, we combine them into one constant, k_a.

$$\frac{\partial J}{\partial E} = k_a.DOS(E) \tag{B.2}$$

We assume $DOS(E)$ to have Gaussian distribution. Nevertheless, the simulated photocurrent obtained by integrating **Equation B.2** does not represent the observed experimental photocurrent well in the saturated photocurrent region. The simulated photocurrent gives a constant value in the saturated photocurrent region. In the experimental photocurrent, the saturated photocurrent does not have a constant value but gradually increasing. We suspected that the built-in electric field from the band bending forces more holes to come to the surface, hence increasing the photocurrent. To improve our fitting, we add the second term to account for increasing hole flux due to the built-in electric field (drifting effect) from the band bending:

$$\frac{\partial J}{\partial E} = k_a.DOS(E) + k_b(E - E_{fb})^{-1/2} \int DOS(E)dE \tag{B.3}$$

where:

k_b = Drifting constant

$(E - E_{fb})^{-1/2}$ = Magnitude of the space charge region. E_{fb} is the flat band potential. The value of $E_{fb} = 0.45$ V vs. RHE is used in all of our fitting

$\int DOS(E)dE$ = Number of the available states that the new arriving holes can participate in.

As mentioned earlier, we assume $DOS(E)$ to have Gaussian distribution. The expression can be written as:

$$DOS(E) = \frac{a}{\sigma\sqrt{(2\pi)}} exp(-\frac{(E-\mu)^2}{2\sigma^2}) \tag{B.4}$$

where:

a = Magnitude of the peak

σ = Width of the peak

μ = Position of the peak

Our fitting function is obtained by substituting **Equation B.4** into **Equation B.3**. The constant k_a in **Equation B.2** is combined with a in **Equation B.4** to give the magnitude parameter, A. Our fitting function is described in **Equation B.5**

$$\frac{\partial J}{\partial E} = \frac{A}{\sigma\sqrt{(2\pi)}} exp(-\frac{(E-\mu)^2}{2\sigma^2}) + k_b(E - E_{fb})^{-1/2} \int \frac{A}{\sigma\sqrt{(2\pi)}} exp(-\frac{(E-\mu)^2}{2\sigma^2})dE \tag{B.5}$$

Parameter	Solution	
	NaP_i	HMF/NaP_i
A1	n/a	0.323
$\sigma 1$	n/a	0.100
$\mu 1$	n/a	0.661
A2	1.080	1.040
$\sigma 2$	0.163	0.188
$\mu 2$	0.939	0.938
k_b	0.240	0.240

Table B.1: Fitted parameters from the fit $\partial J/\partial E$ of NaP_i and HMF/NaP_i solution

B.3 Supplementary Figures and Tables

B.3.1 Fitted parameters

B.3.2 Fitting $\partial J/\partial E$ of HMF/NaP$_i$ with only one fitting curve

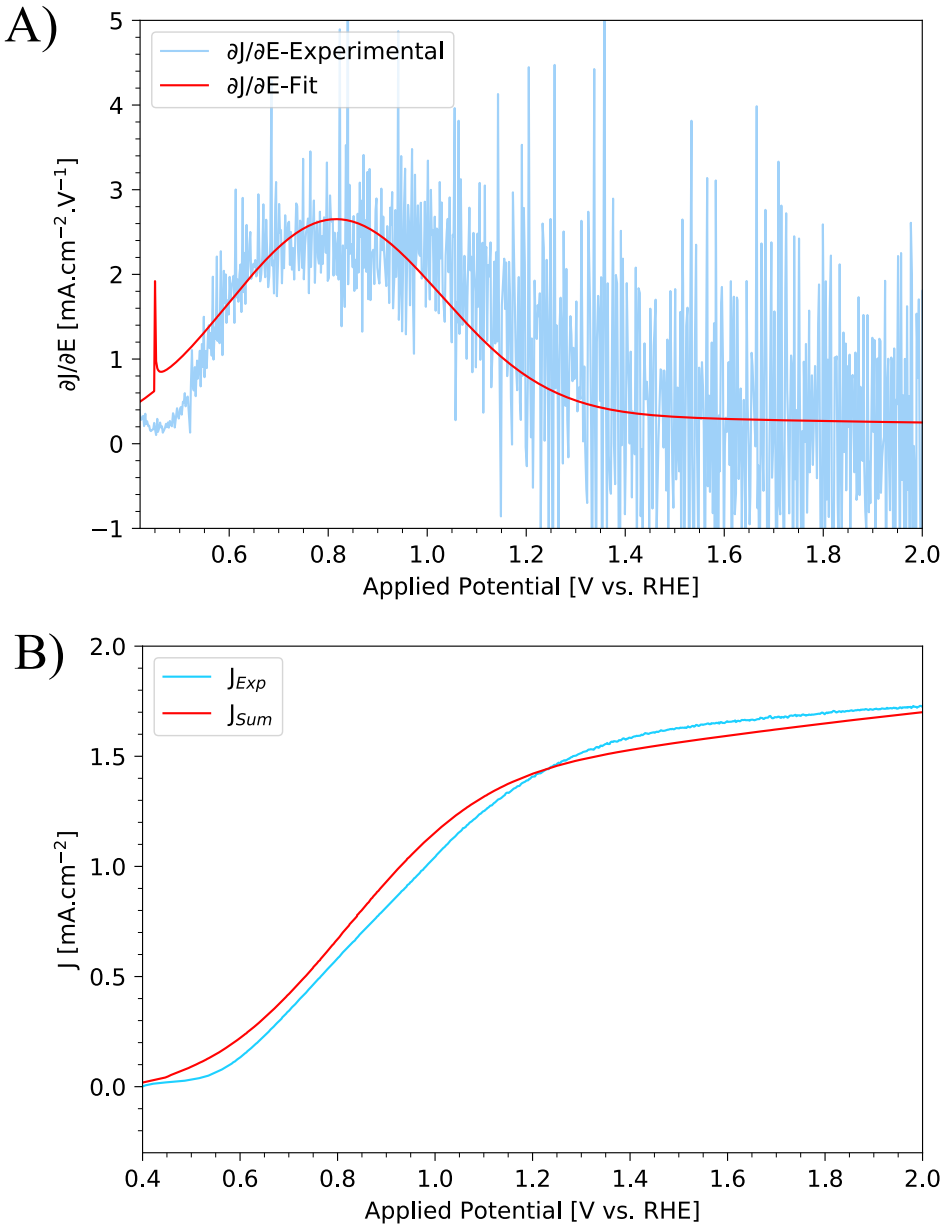

Figure B.1: A) $\partial J/\partial E$ analysis and B) Simulated photocurrent of HMF/NaP$_i$ solution with only 1 fitting curve

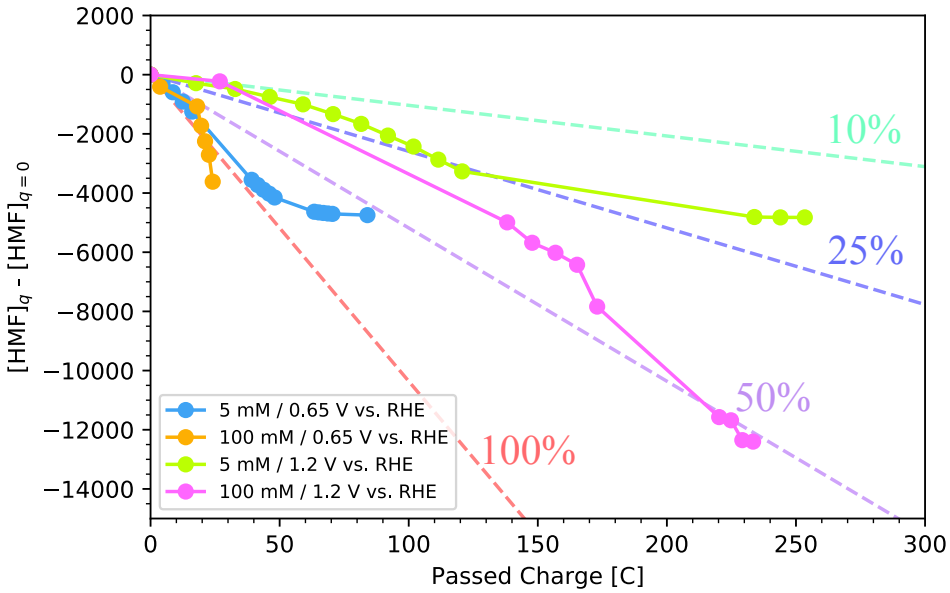

Figure B.2: HMF consumption as the function of passed charge at 0.65 V and 1.20 V vs. RHE and at the initial HMF concentration of 5 mM and 100 mM. The dotted line represent the Faradaic efficiency of 10%, 25%, 50% and 100% as calculated from two-electron oxidation of HMF

B.3.3 EIS fitting

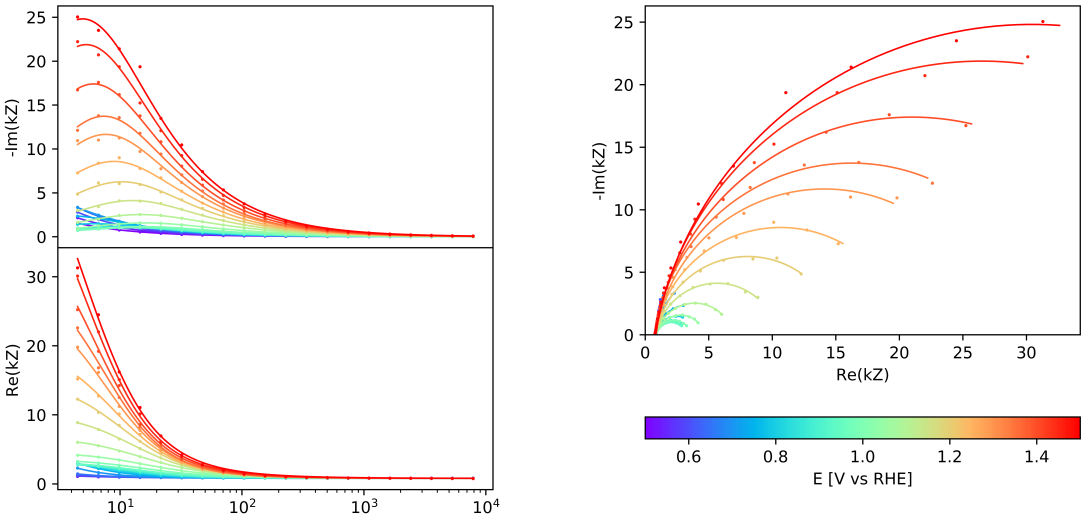

Figure B.3: Bode plot (left) and Nyquist plot (right) in NaP_i electrolyte.

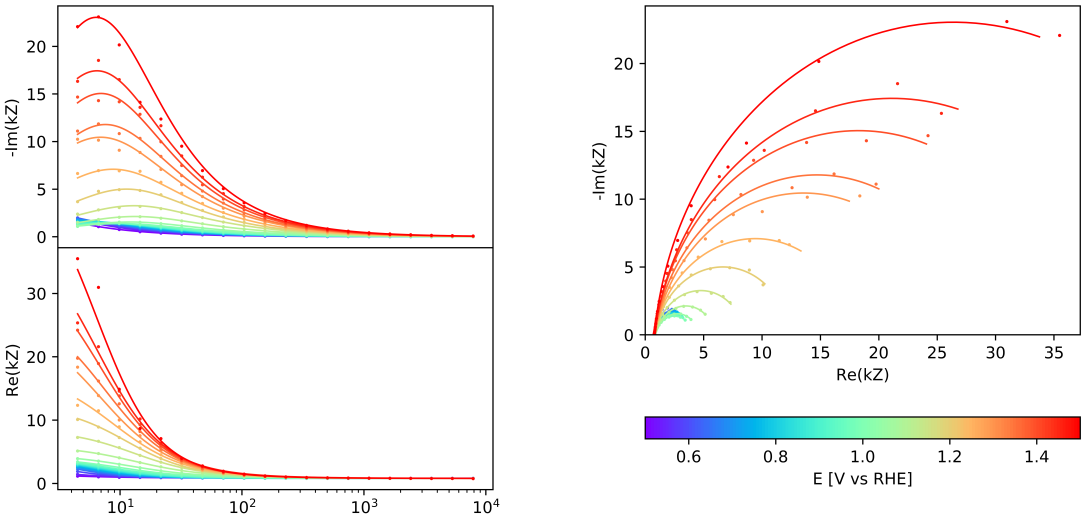

Figure B.4: Bode plot (left) and Nyquist plot (right) in HMF/NaP_i solution

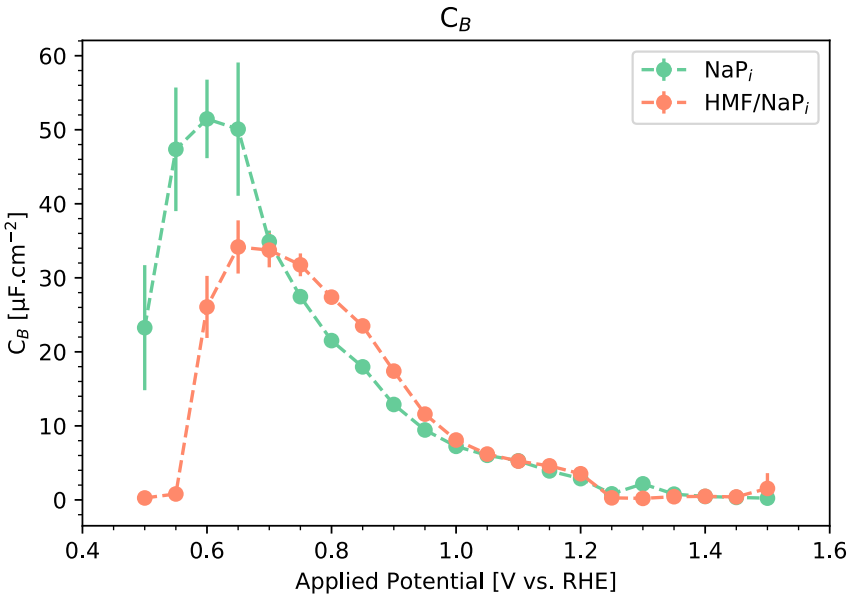

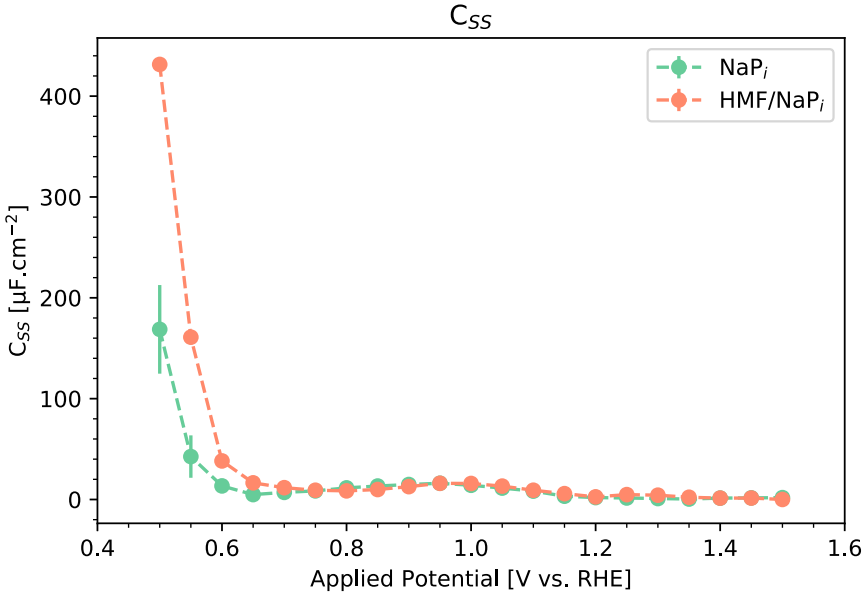
C_{SS}
NaP$_i$
HMF/NaP$_i$
C_{SS} [µF.cm^{-2}]
400
300
200
100
0
0.4
0.6
0.8
1.0
1.2
1.4
1.6
Applied Potential [V vs. RHE]

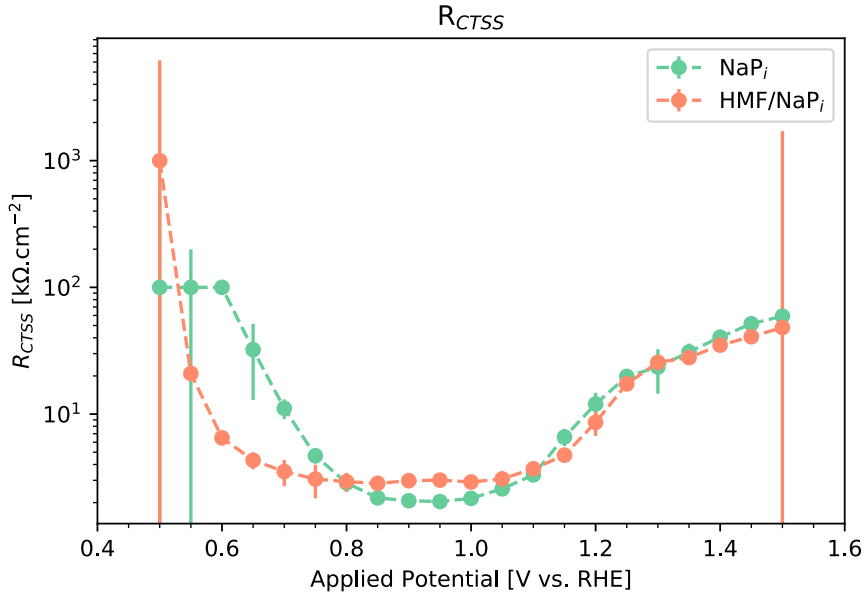
R_{CTSS}
NaP$_i$
HMF/NaP$_i$
R_{CTSS} [kΩ.cm^{-2}]
10^3
10^2
10^1
0.4
0.6
0.8
1.0
1.2
1.4
1.6
Applied Potential [V vs. RHE]

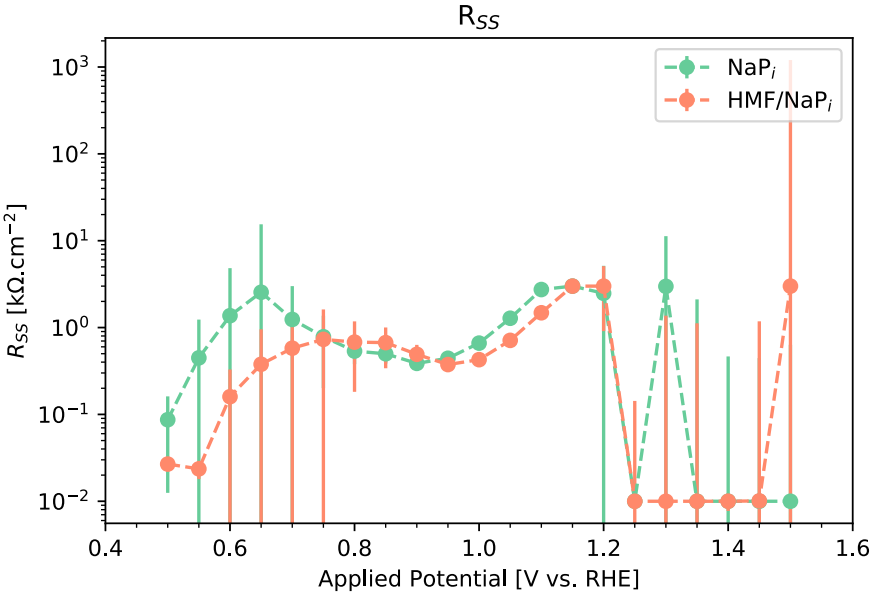

Figure B.5: The fitted value (C_B, C_{SS}, R_{CTSS} and R_{SS}) in NaP_i and HMF/NaP_i solution. The R_B value was kept constant at 0.79 kΩ.cm^{-2} for both solutions.

B.3.4 The fitted $\partial J/\partial E$ and the DOS(E) as probed from EIS

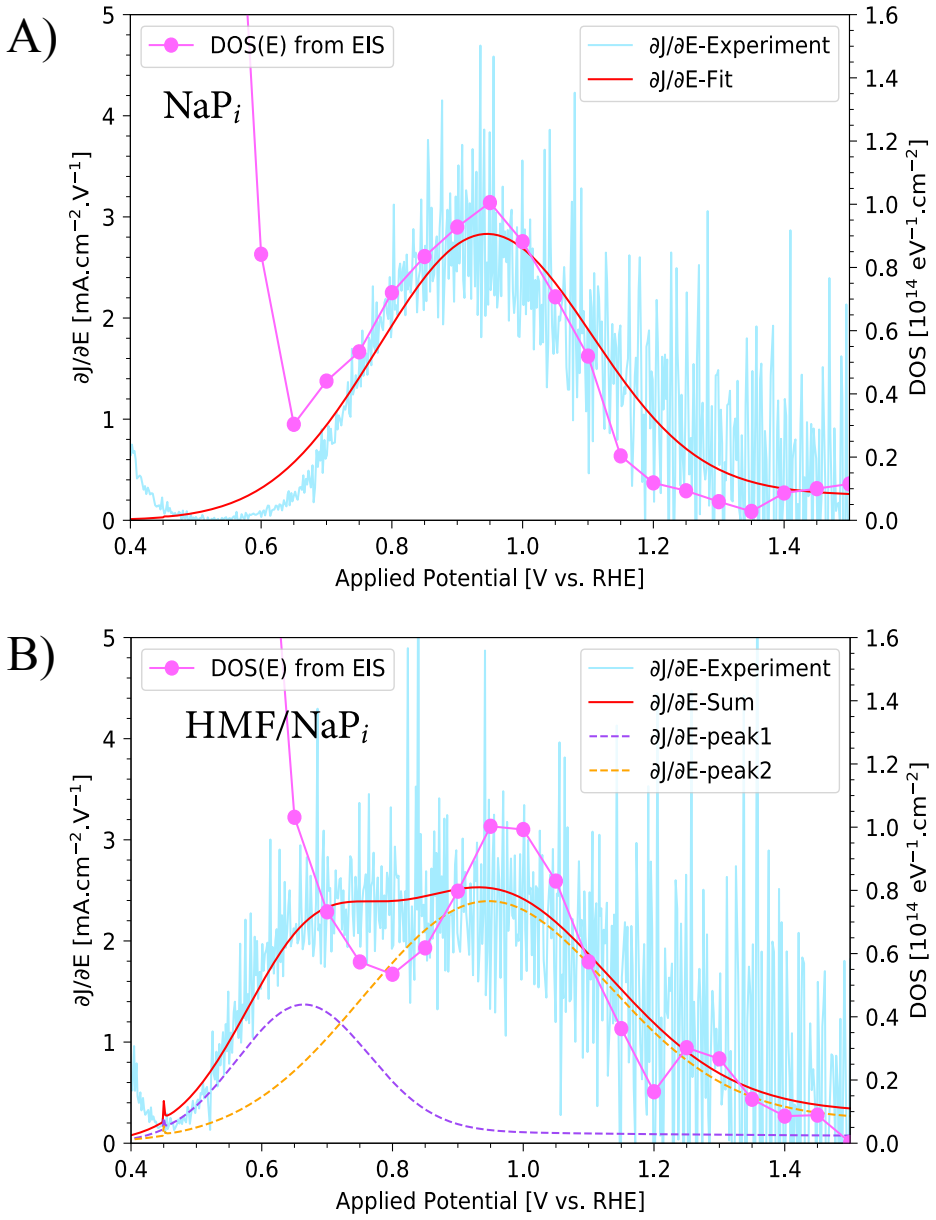

Figure B.6: Overlaid graph of the experimental derivative voltammogram, the fit $\partial J/\partial E$ and the DOS(E) as found from EIS in A) NaP$_i$ electrolyte and B) 5 mM HMF in NaP$_i$ solution

References

[1] Wang, Z.; Fan, F.; Wang, S.; Ding, C.; Zhao, Y.; Li, C. Bridging surface states and current–potential response over hematite-based photoelectrochemical water oxidation. *RSC Advances* **2016**, *6*, 85582–85586.

[2] Memming, R. *Semiconductor Electrochemistry*; Wiley-Blackwell, 2015; pp 89–125.

Appendix C

Supporting Information to Chapter 4

C.1 Calculation for HMF consumption from photoelectrolysis of HMF using TemBen/Nafion® modified electrode

There are many possible oxidation route to HMF oxidation which requires different amount of electron per mole of HMF. For the sake of the simplicity for the calculation, we will assume that HMF undergoes 2 electrons oxidation to DFF or HMFCA.

Different in HMF concentration $= 50 \times 10^{-3}\, C \times \frac{1\, mol\, e^-}{96485\, C} \times \frac{1\, mol\, HMF}{2\, mol\, e^-} \times \frac{1}{0.050\, L} = 5.2\, \mu M$

C.2 Experimental details

C.2.1 Electrode fabrication

Fabrication of MnO_x/WO_3 photoelectrode

The MnO_x/WO_3 photoelectrode was prepared by photoelectrodeopistion of MnO_x onto the WO_3 photoelectrode in a custom-made photoelectrolysis cell with a quartz window containing 50 mM $MnSO_4$ with 0.1 M H_2SO_4 (pH=1) as a supporting electrolyte. The photoelectrodeposition was performed by applying a constant potential of 0.9 V vs. RHE under chopped illumination of 1 sun (2 seconds on and 1 second off). A three-electrode configuration was adopted. The working electrode, reference electrode and counter electrode were WO_3 photoanode, Ag/AgCl reference electrode and Pt wire respectively. The photoelectrodeposition was performed until a total charge of 5.0 mC/cm^2 was passed.

The successful deposition of MnO_x films onto WO_3 electrode was confirmed by Raman spectroscopy (Figure C.1). The Raman spectra of the MnO_x/WO_3film is very similar to that of MnO_x with no characteristic peak of WO_3.

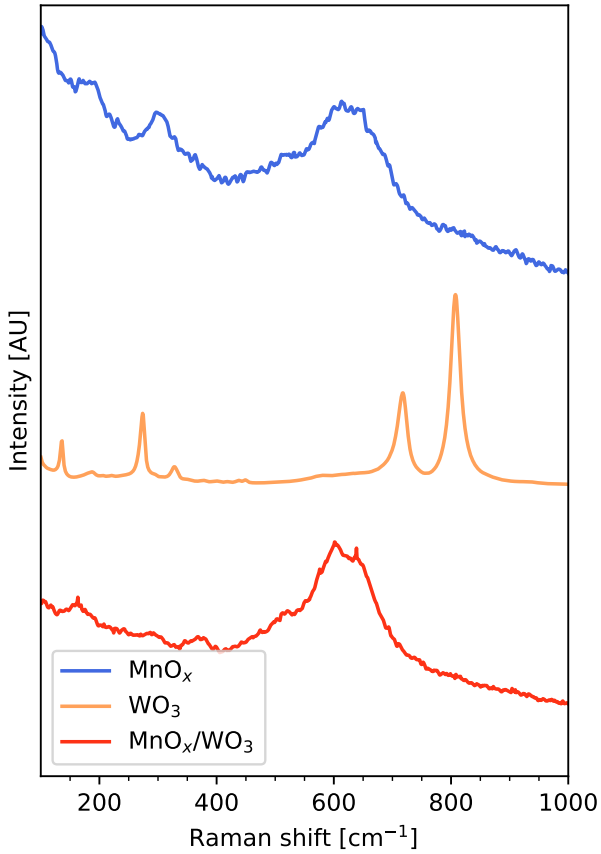

Figure C.1: Raman spectra of MnO_x, WO_3 and MnO_x/WO_3 films on FTO

Fabrication of TEMPO/Nafion® modified electrode

The TEMPO/Nafion® modified electrodes were prepared from a precursor solution containing 25 or 500 mg of TEMPO in 1 mL of a commercial 5 wt % Nafion® in the mixture of lower aliphatic alcohols and water (Sigma-Aldrich). The precursor solution was used in various fabrication methods (describe below) to prepare TEMPO/Nafion® modified electrode. The substrate used in the film fabrication was 2.5 × 2.5 cm^2 FTO coated glass. Kapton tape was used to mark the electrical contact area during the film fabrication process. After the fabrication, the fabricated electrode was rinsed with miliQ water to remove any excess TEMPO from the film.

Drop casting: The TEMPO in Nafion® precursor solution (200 μL) were dropped onto a FTO substrate and allowed dry naturally at room temperature.

Doctor blading: The TEMPO in Nafion® precursor solution was rolled onto a FTO substrate and allowed dry naturally at room temperature.

Spray coating: A FTO substrate was first heated on a hot plate at 80 °C for 2 minutes. Then, the TEMPO in Nafion® precursor solution (5 mL) was sprayed slowly onto the heated FTO substrate. Only the 25 mg/mL TEMPO in Nafion® precursor solution was used.

Spin coating: The TEMPO in Nafion® precursor solution (200 μL) was dropped onto a FTO substrate and spun at 2000 rpm for 30 seconds.

Fabrication of TemBen/Nafion® modified electrode

The TemBen/Nafion® precursor solution was made by dissolving TemBen (50 mg, Fluorochem) into 1 mL of a commercial 5 wt % Nafion® in the mixture of lower aliphatic alcohols and water. The TemBen/Nafion® precursor solution (100 μL) was then dropped onto a spinning FTO substrate (500 rpm). The FTO substrate is 2.5 $\times$ 2.5 cm^2 in dimension and the electrical contact area was marked by Kapton tape. To remove the excess liquid, the substrate was spun at the desired spin speed for 45 seconds to give a film with different thickness. The desired spin speed are 500, 1000, 2000 and 3000 rpm. The fabricated films were rinsed with miliQ water to remove any excess TemBen from the film.

C.2.2 Standard electrochemical measurements

All electrochemical measurements were collected using a BioLogic SP-200 potentiostat in a three-electrode configuration. Unless noted otherwise, the counter, and reference electrodes were a graphite rod, and Ag/AgCl in saturated KCl respectively. The measurements were performed in a custom-made cappuccino cell. All CVs and LSVs experiments were performed at a scan rate of 20 mV/s. All the measurements for the TEMPO/Nafion® and TemBen/Nafion® modified electrodes were performed in 0.1 M sodium borate electrolyte at pH 9. All the measurements for NHPI and NHPI/Nafion® modified electrodes were performed in 0.1 M sodium phosphates electrolyte at pH 4.

C.2.3 Standard photoelectrolysis and electrolysis

Unless otherwise noted, photoelectrolysis and photoelectrolysis were performed in a custom-made cell with a quartz window for the illumination for the photoelectrolsysis. The electrolysis and photoelectrolysis were performed in a three electrode configuration. The counter, and reference electrodes were a graphite rod, and Ag/AgCl in saturated KCl respectively. The solution was agitated by continuous stirring.

C.3 Supplementary figures and tables

C.3.1 Cyclic voltammograms of the stability test of TEMPO/Nafion® with various fabrication methods

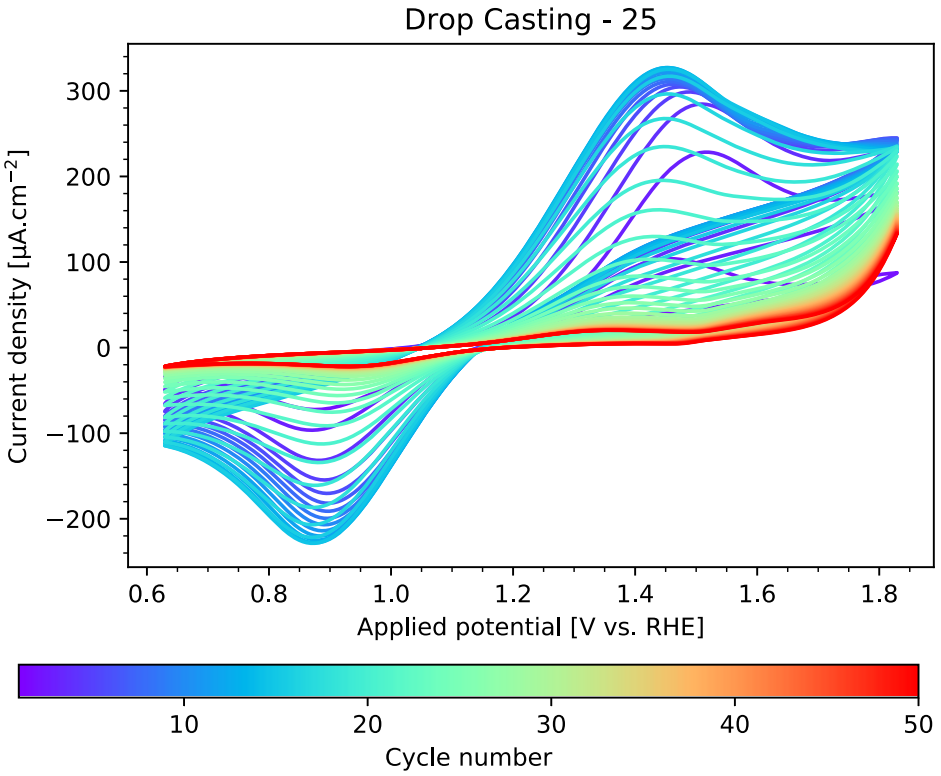

Figure C.2: Cyclic voltammograms of the drop casting-25 electrode

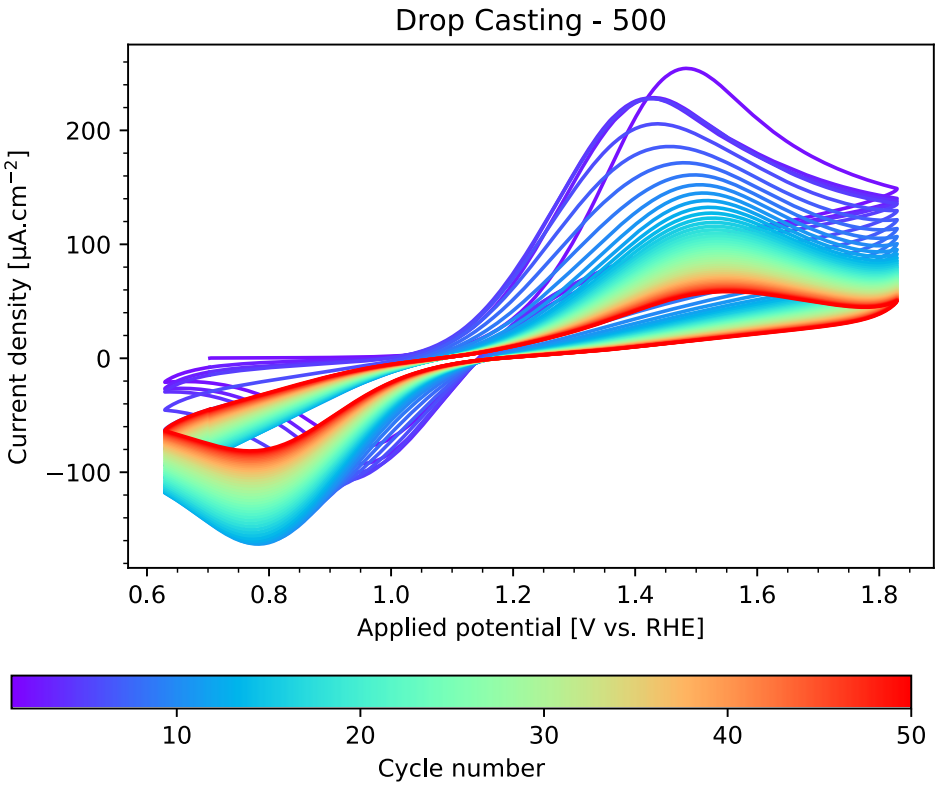

Figure C.3: Cyclic voltammograms of the drop casting-500 electrode

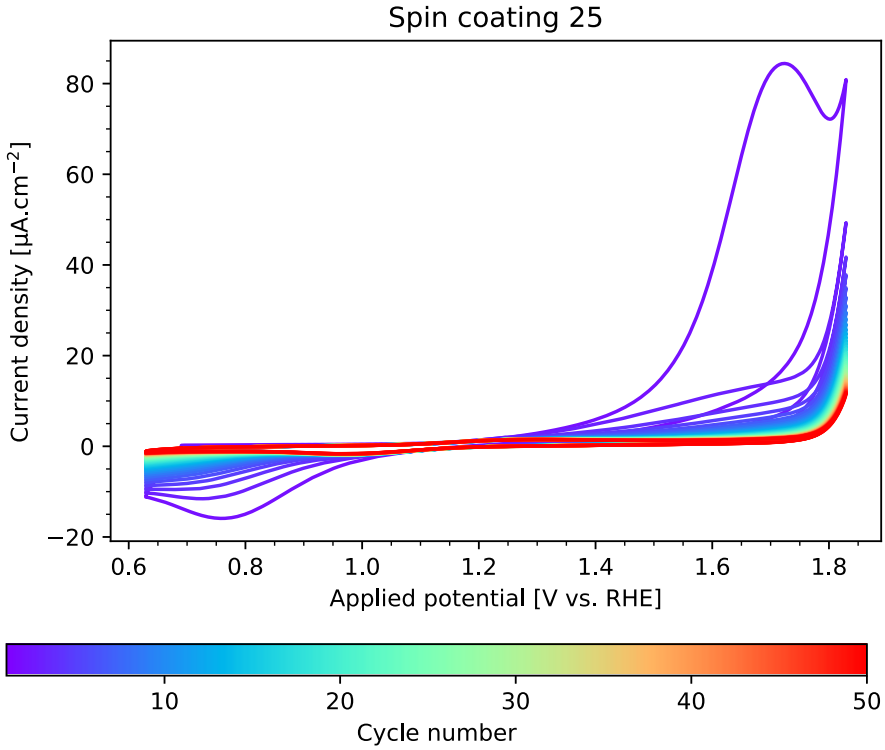

Figure C.4: Cyclic voltammograms of the spray coating-25 electrode

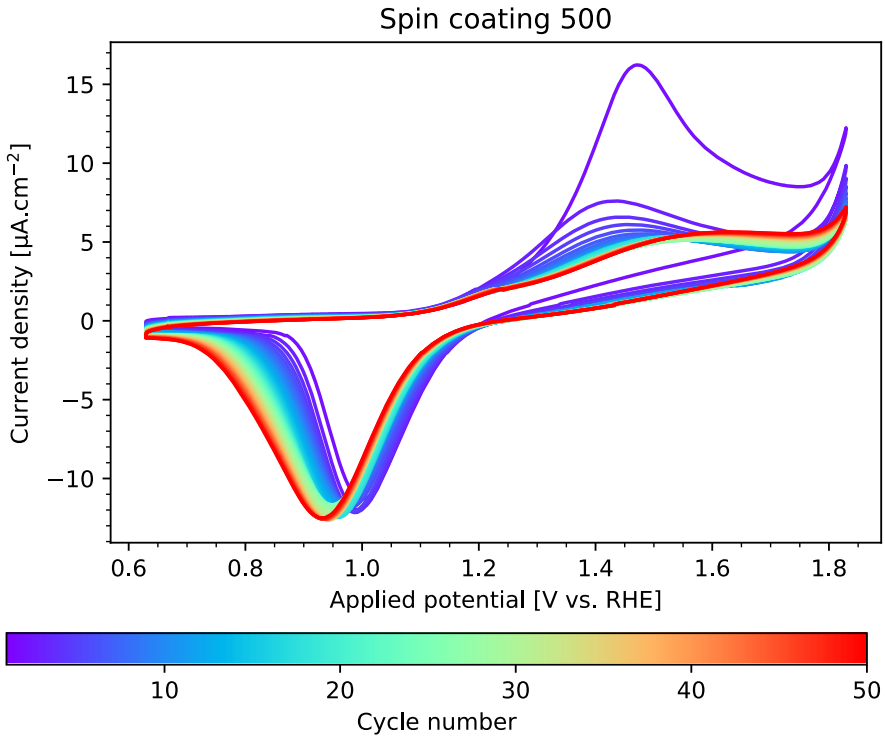

Figure C.5: Cyclic voltammograms of the spray coating-500 electrode

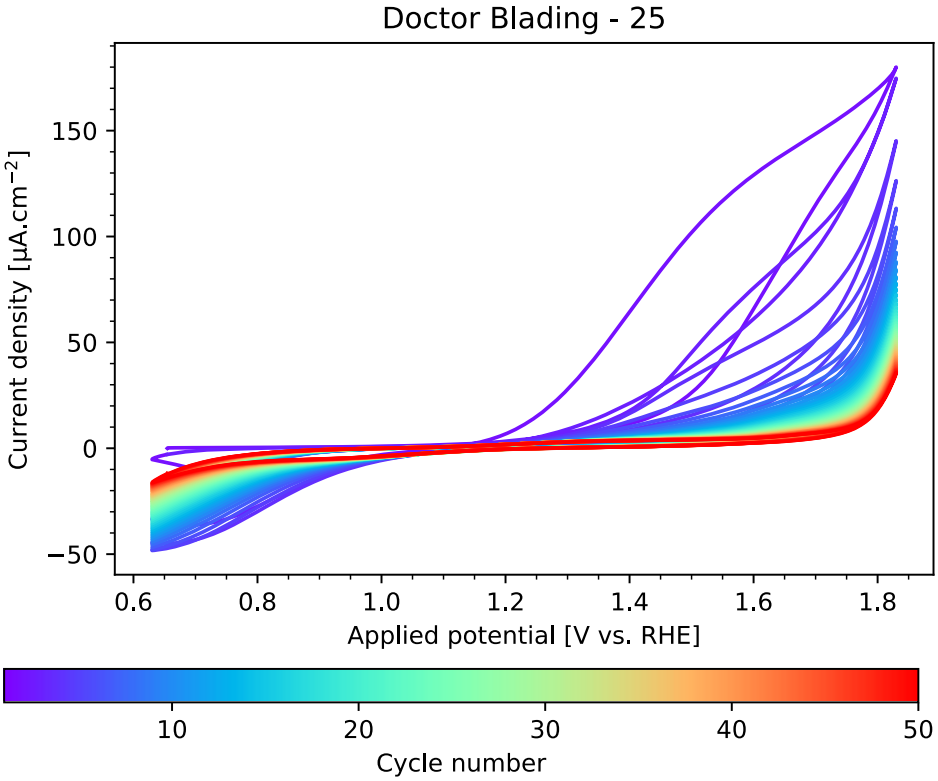

Figure C.6: Cyclic voltammograms of the doctor blading-25 electrode

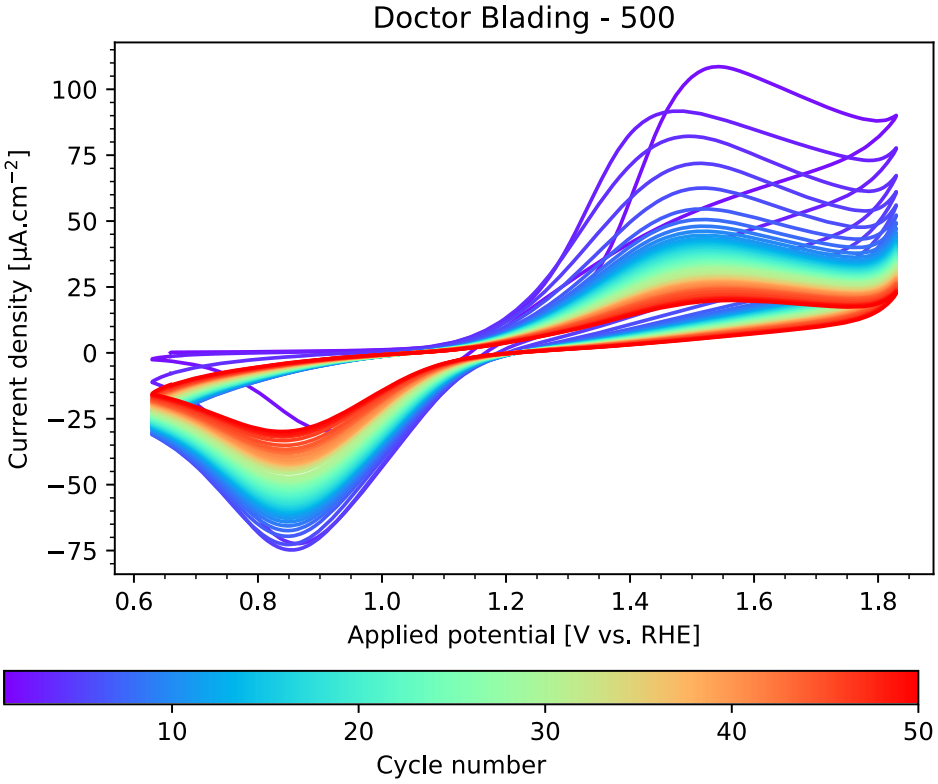

Figure C.7: Cyclic voltammograms of the doctor blading-500 electrode

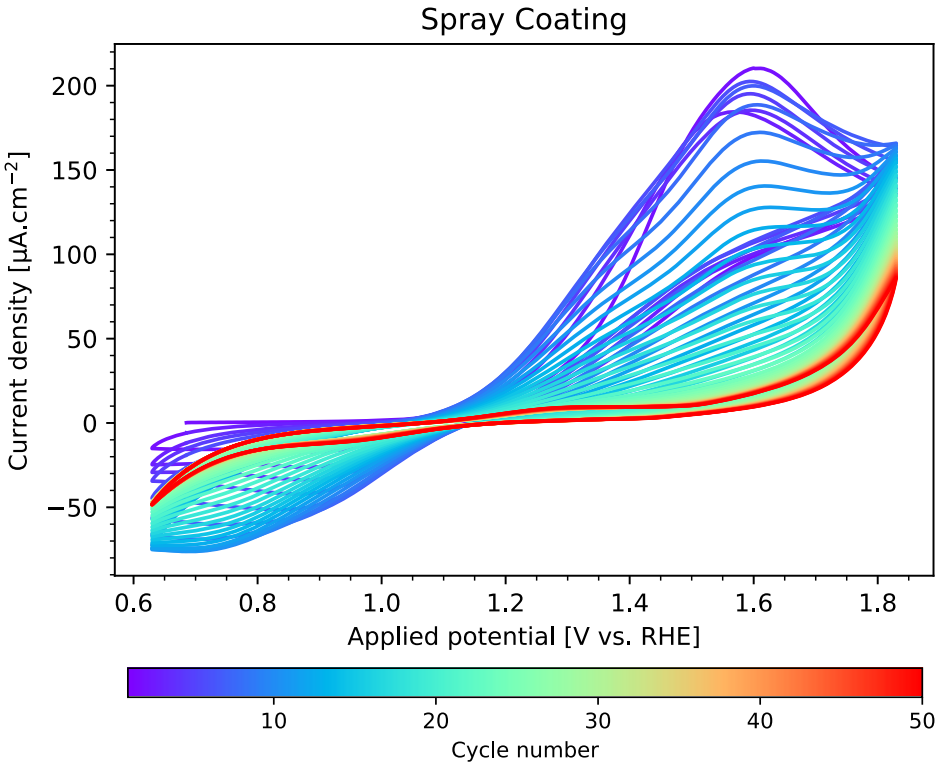

Figure C.8: Cyclic voltammograms of the spray coating electrode

C.3.2 Cyclic voltammograms of various TEMPO/Nafion® modified electrodes right after the stability test and with the fresh electrolyte

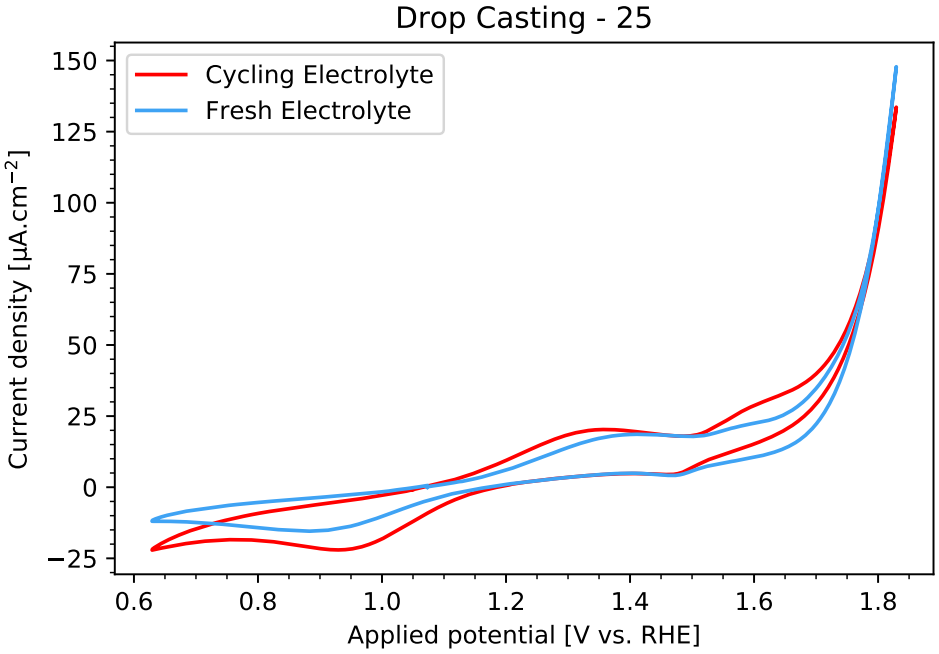

Figure C.9: Cyclic voltammograms of the cycling electrolyte and the fresh electrolyte of the drop casting -25 electrode

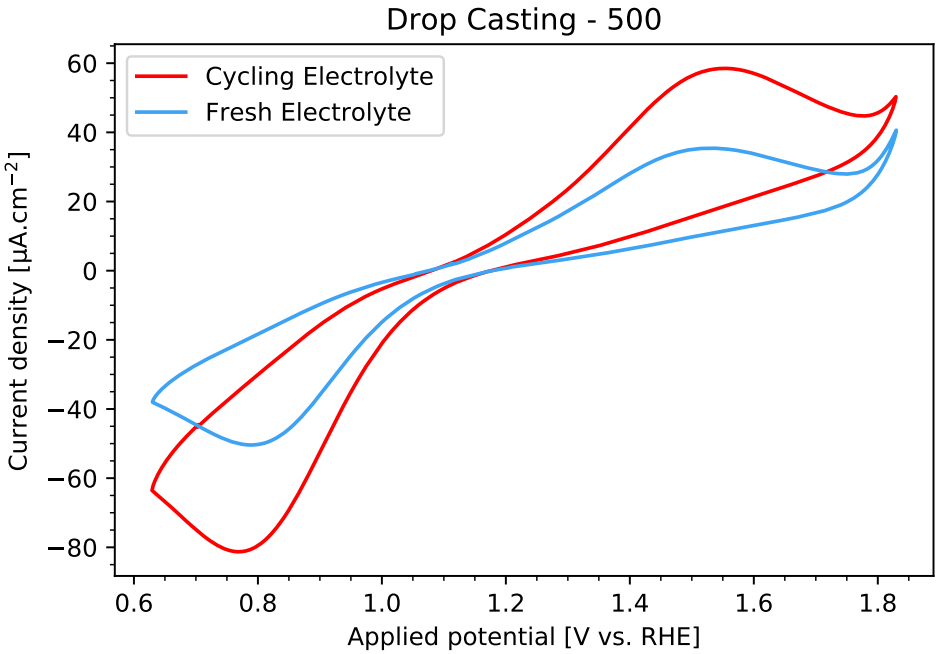

Figure C.10: Cyclic voltammograms of the cycling electrolyte and the fresh electrolyte of the drop casting -500 electrode

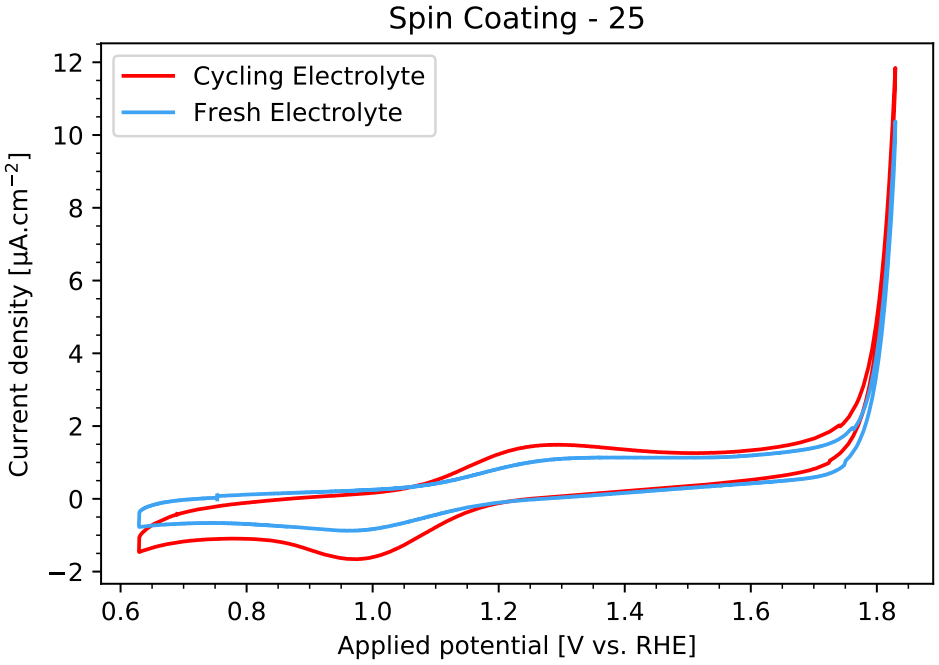

Figure C.11: Cyclic voltammograms of the cycling electrolyte and the fresh electrolyte of the spin coating -25 electrode

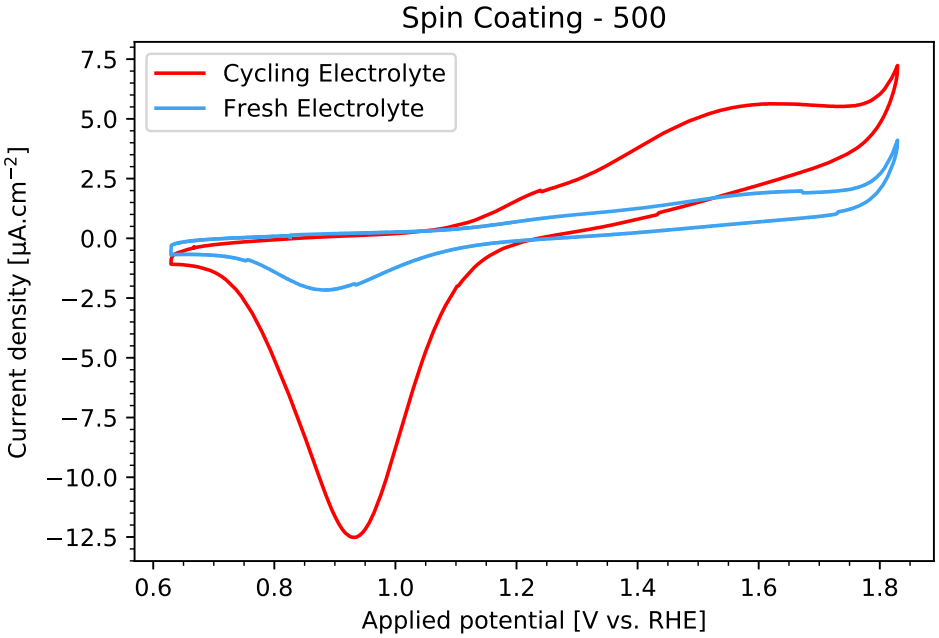

Figure C.12: Cyclic voltammograms of the cycling electrolyte and the fresh electrolyte of the spin coating -500 electrode

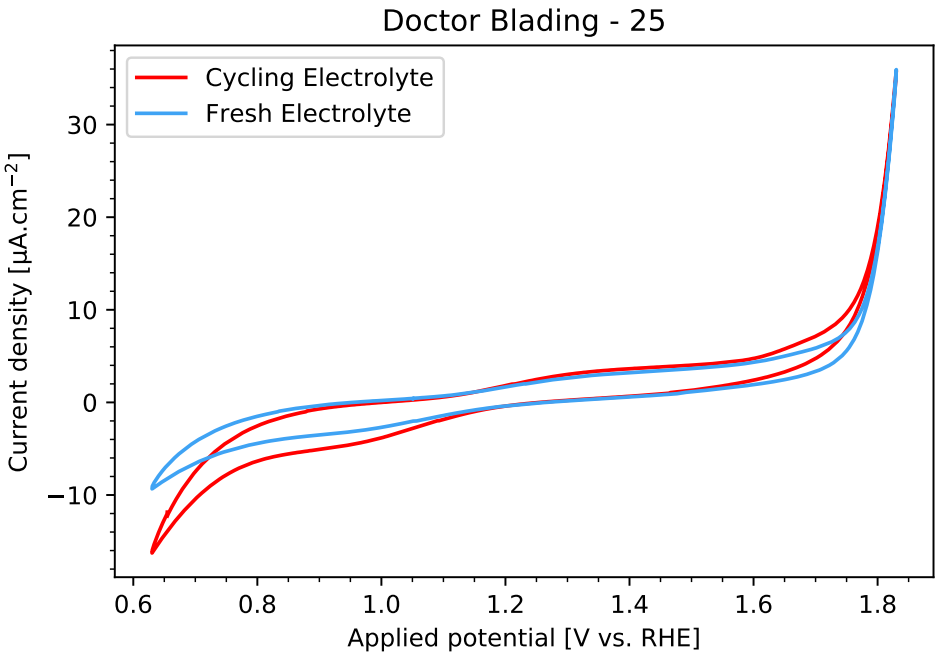

Figure C.13: Cyclic voltammograms of the cycling electrolyte and the fresh electrolyte of the doctor blading -25 electrode

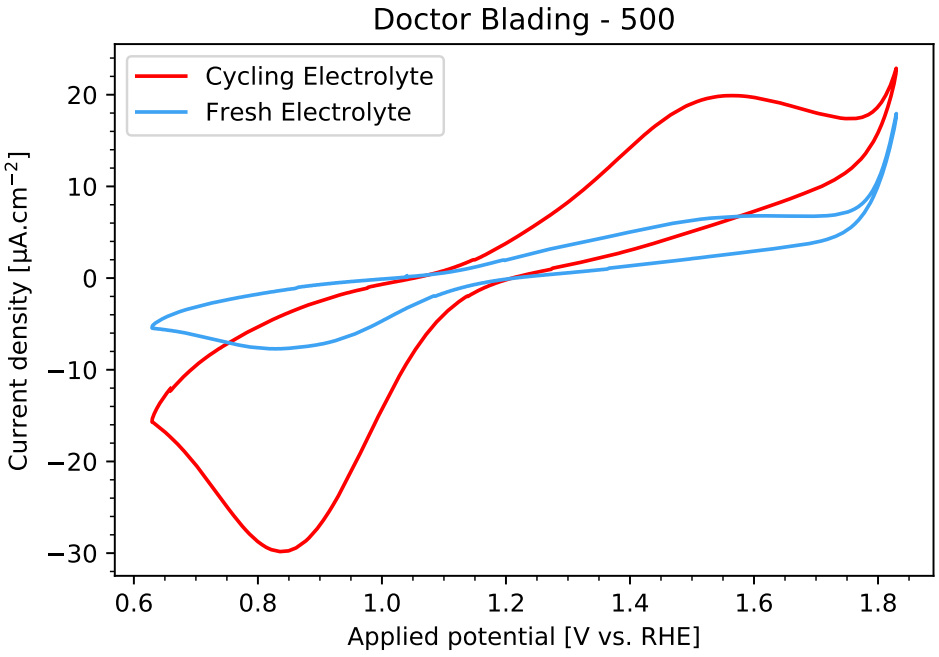

Figure C.14: Cyclic voltammograms of the cycling electrolyte and the fresh electrolyte of the doctor blading -500 electrode

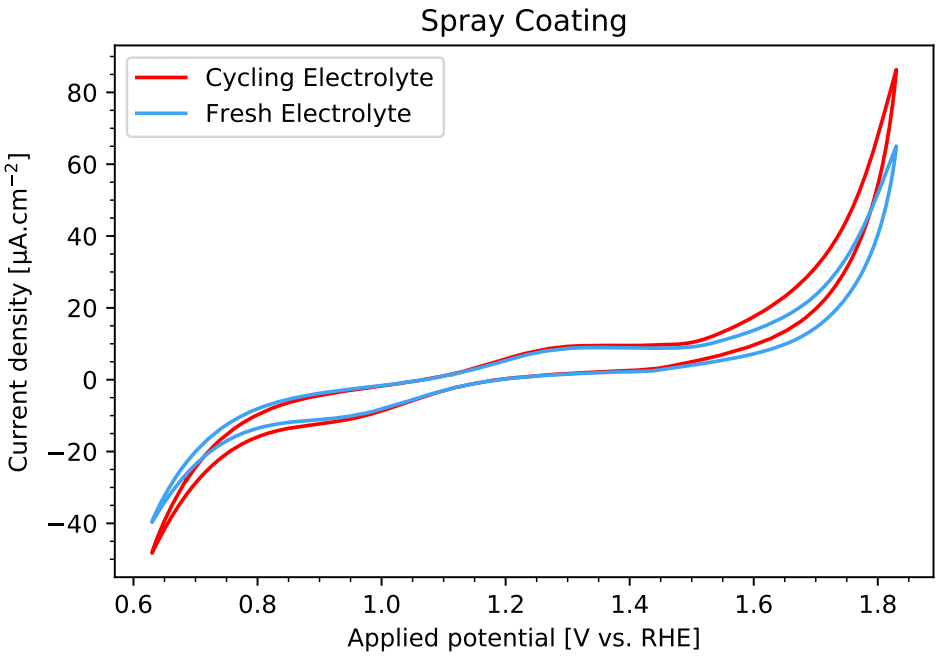

Figure C.15: Cyclic voltammograms of the cycling electrolyte and the fresh electrolyte of the spray coating electrode

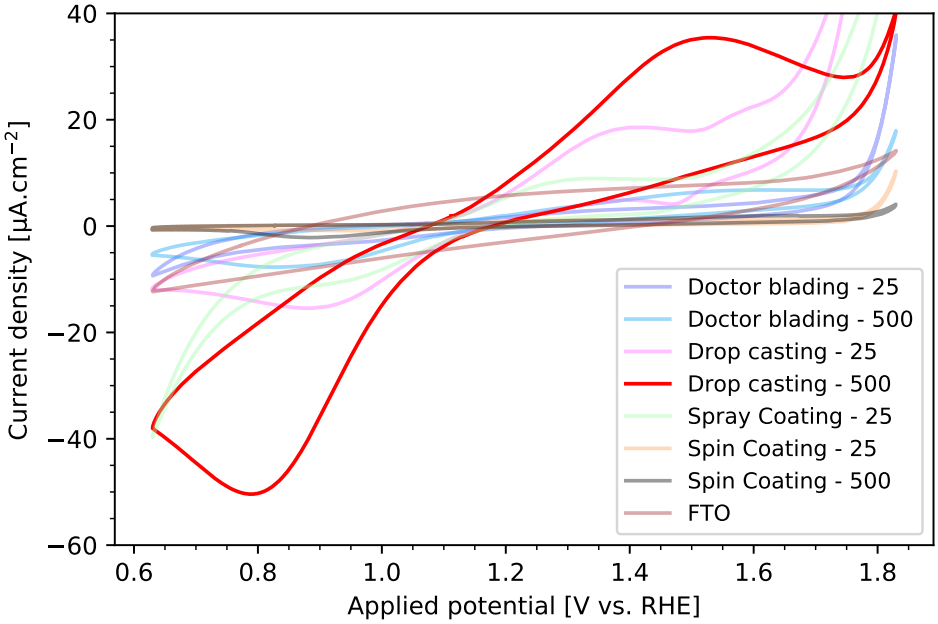

Figure C.16: Combined cyclic voltammograms of TEMPO/Nafion® modified electrodes in the fresh electrolyte after the stability tests

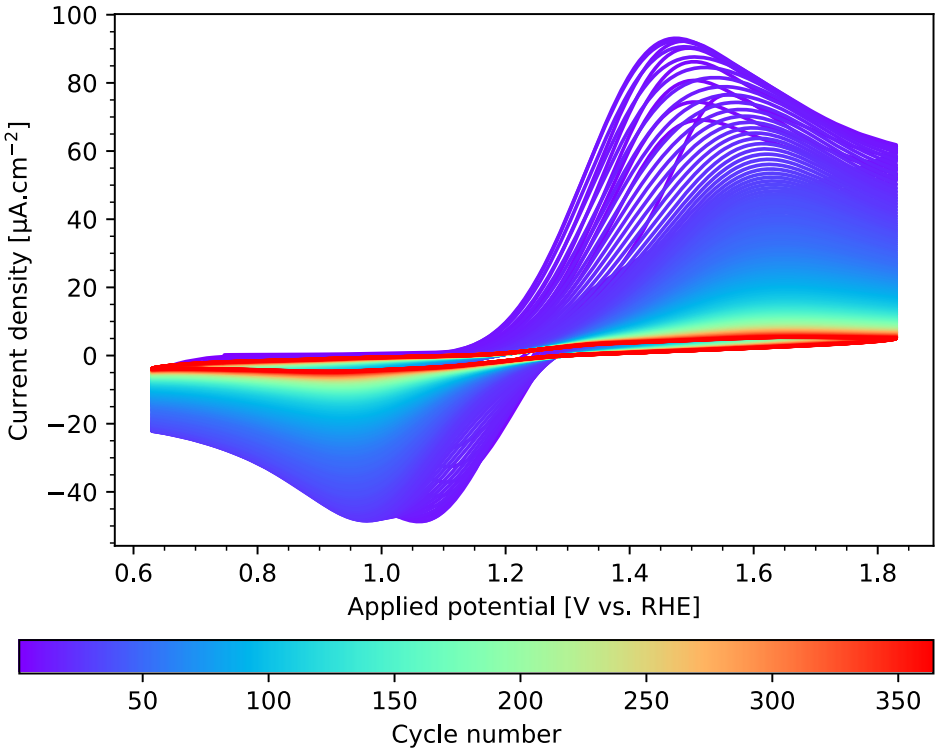

Figure C.17: Cyclic voltammograms from the extended stability test of the drop casting-500 electrode

C.3.3 Cyclic voltammograms of the stability test of TemBen/Nafion® modified electrode

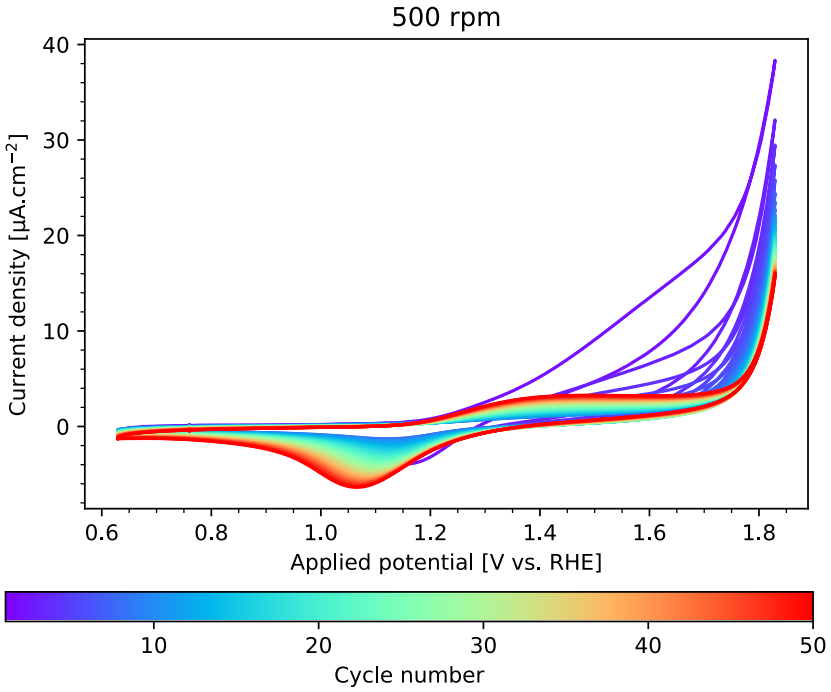

Figure C.18: Cyclic voltammograms of the stability test of the 500 rpm electrode

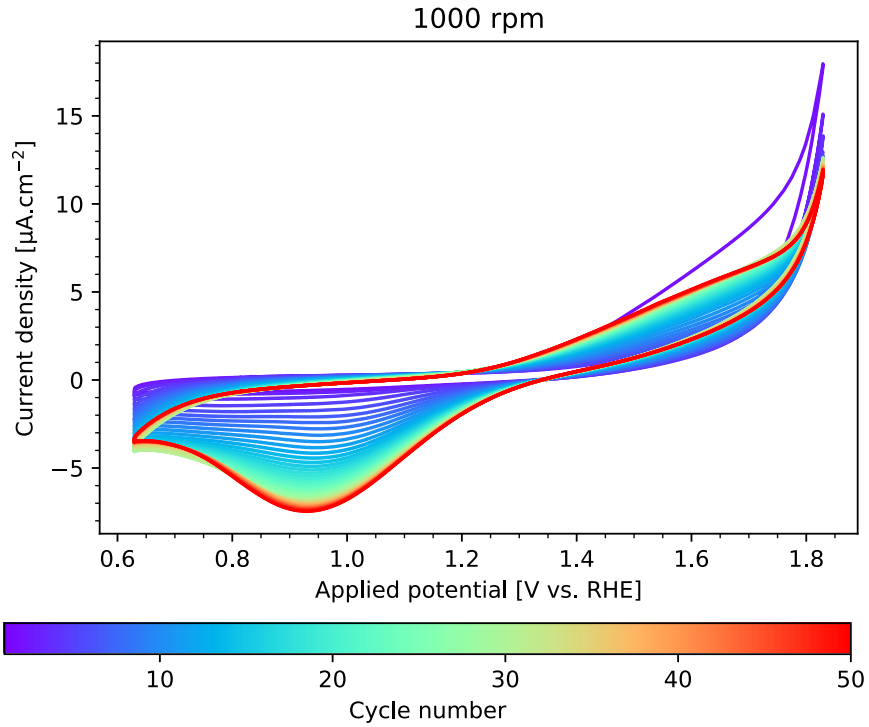

Figure C.19: Cyclic voltammograms of the stability test of the 1000 rpm electrode

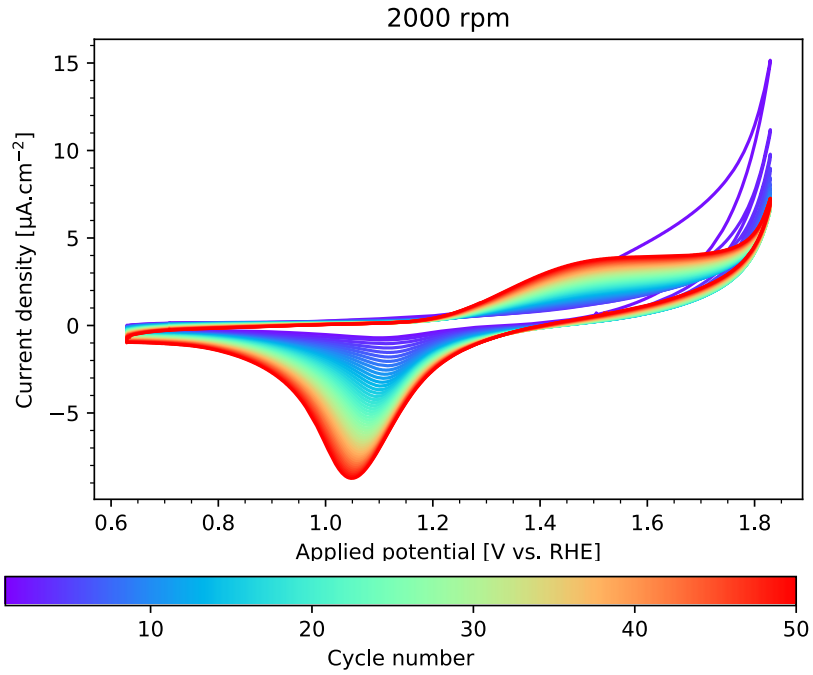

Figure C.20: Cyclic voltammograms of the stability test of the 2000 rpm electrode

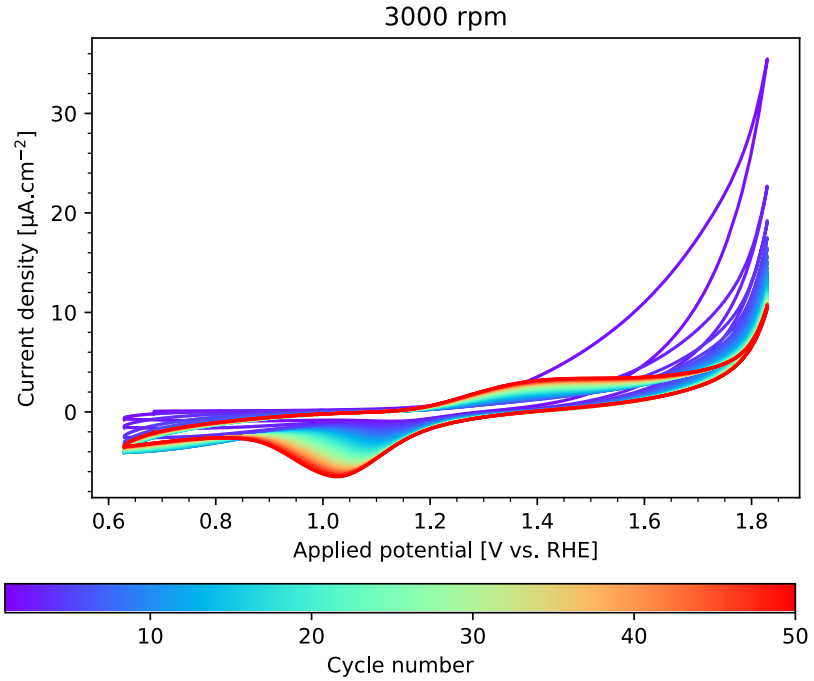

Figure C.21: Cyclic voltammograms of the stability test of the 3000 rpm electrode

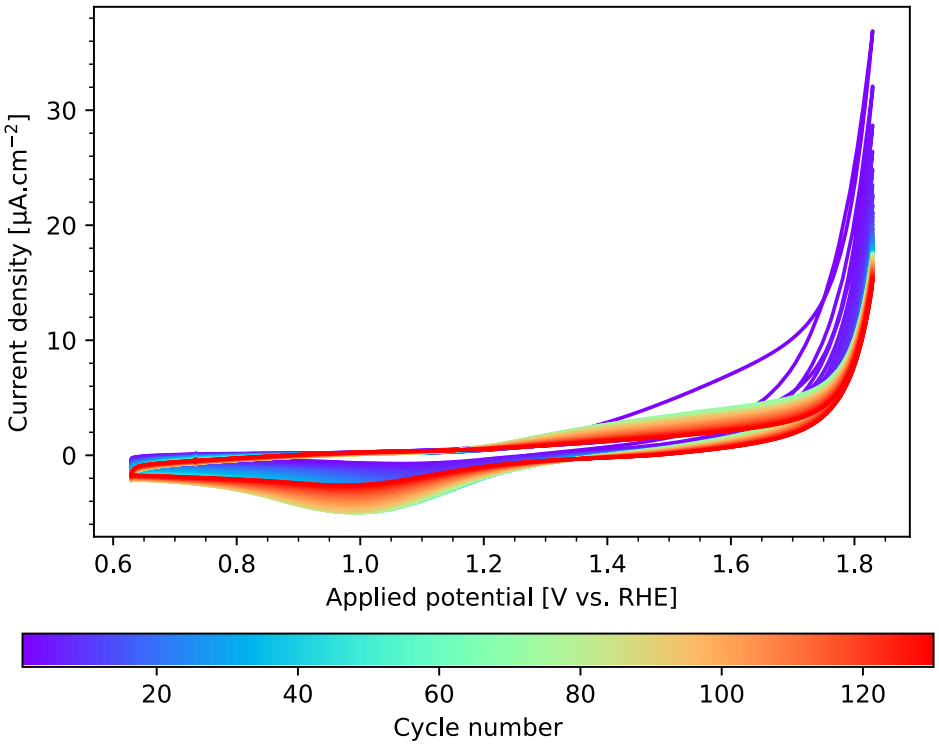

Figure C.22: Cyclic voltammograms of the extended stability test of the 500 rpm electrode

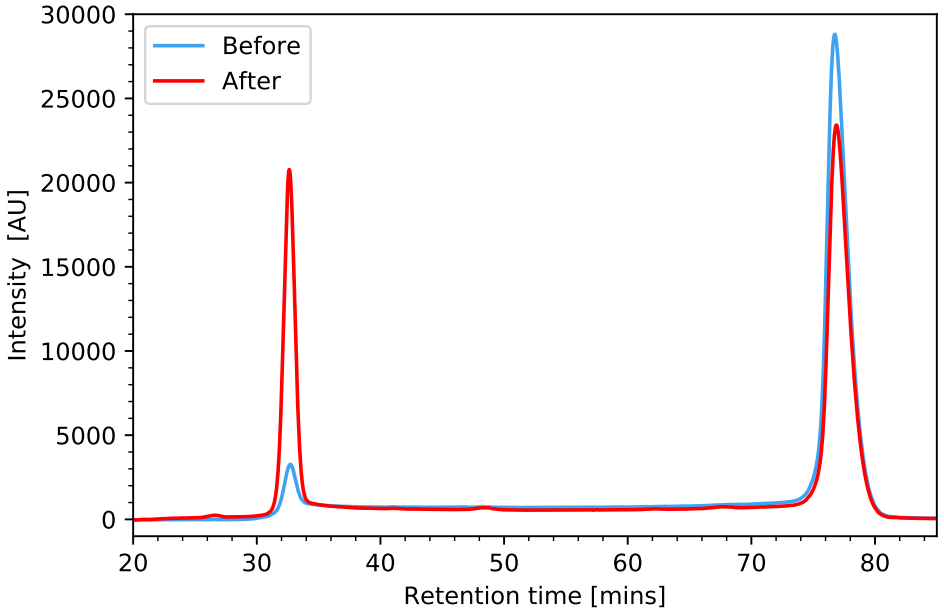

Figure C.23: Chromatogram before and after the electrolysis of NHPI using FTO as a working electrode

Appendix D

Supporting Information to Chapter 5

D.1 Experimental details

D.1.1 $CuWO_4$ electrode fabrication (condition A)

$CuWO_4$ electrode was synthesized by a sol-gel deposition method. The precursor solution was prepared by dissolving 6.82 g $CuCl_2.2H_2O$ and 9.85 g ammonium metatungstate $(NH_4)_6H_2W_{12}O_{40}$ in Mili Q water. The final volume of the solution was adjusted to 25 mL before 8.25 g of polyethylene glycol - 300 (PEG-300) was added to give a bright-green solution. The solution was filtered through a 0.22 µm hydrophilic syringe filter to remove any non-dissolving impurity. $CuWO_4$ electrode was fabricated by dropping 200 µL of the precursor solution onto a clean 2.5 × 2.5 cm^2 FTO glass (Solaronix) and spinning at 2000 rpm using a Laurel spin coater (Model WS-650MZ-23NPPB) for 30 seconds. The prepared films were then annealed under a constant flow of air at 550 °C for 1 hour in a muffed furnace. We found that if the constant air was not supplied during the annealing, the black soot layer (likely from the incomplete combustion of PEG-300 would stick to the surface of the electrode). Hence, the requirement for a constant flow of air in the furnace. A small section at the top of the electrode was masked with Kapton tape to allow for electrical contact.

D.1.2 Modifying number of oxygen vacancies in $CuWO_4$ electrode

The number of OVs in the $CuWO_4$ electrode was altered by subjecting the $CuWO_4$ electrode (condition A) to secondary annealing under a reductive atmosphere to increase the number of OVs. The condition for the secondary annealing used in the fabrication of conditions B, C, and D are shown in Table D.1. For conditions B, C, and D, the secondary annealing was performed in a tube furnace. The electrodes were placed at the center of the furnace before a constant flow of Ar (400 mL/minutes) flowed in the furnace. The temperature inside the furnace was kept at room temperature for 30 minutes to ensure the complete removal of oxygen. The temperature was then ramped up at the rate of 10 °C/minutes to 300 °C. A hydrogen flow at 60 L/minutes (the gas mixture became 13 % hydrogen in Ar) was then introduced into the furnace and the temperature was held constant for a specific time for each condition (see Table D.1). The hydrogen flow was then stopped and the samples were allowed to cool down naturally in the furnace under an Ar flow to room temperature.

Condition	Secondary annealing condition		
	Atmotsphere	**Annealing time**	**Temperature**
B	13 % H_2 in Ar	20 minutes	300 °C
C	13 % H_2 in Ar	60 minutes	300 °C
D	13 % H_2 in Ar	80 minutes	300 °C

Table D.1: Conditions for the secondary annealing for producing the condition B, C, and D $CuWO_4$ electrodes.

D.1.3 Electrochemical measurements

All electrochemical measurements were collected using a BioLogic SP-200 potentiostat in a three-electrode configuration. The counter and the reference electrode were a Pt wire, and Ag/AgCl in saturated KCl respectively. Unless otherwise noted, a buffered aqueous solution of 0.1 M KP_i at pH 7 was used as the electrolyte. For the experiment in a sacrificial condition, the electrolyte was 1.5 M Na_2SO_3 in KP_i at pH 7. All LSV experiments were performed at a scan rate of 20 mV/s. Unless noted otherwise, the illumination intensity was equivalent to 1 Sun. A 450 W Xe arc lamp was used as a light source. The illumination direction for all experiments was from the front (sample) side. The IPCE experiments were carried out using a custom-made setup, using a LabView script to semi-automatically execute the measurements. To ensure no convolution from a contaminant at the surface of the electrode, all electrodes were held at the potential of 1.75 V vs. RHE under 1 sun illumination for 2 minutes before the IPCE measurement. The light source, a 450 W Xe lamp, was connected to a monochromator (MSH-300). The wavelength range for the experiment was 300-800 nm, with a 5 nm increment. The light intensity at each of the measurement points was first measured using a power meter (PM 100 USB from Thorlabs). Then a sample cell, arranged in a three-electrode configuration in a cappuccino cell, was brought to exactly at the position of the power meter. The set constant potential (1.23 and 1.75 V vs. RHE) was then applied. The IPCE at each measurement point was calculated using the following equation:

$$IPCE(\%) = \frac{1240 \times J_\lambda}{\lambda(nm) \times P_\lambda} \tag{D.1}$$

where J_λ and P_λ are the photocurrent and power at wavelength λ.

D.1.4 Microscopy, XRD, Raman Spectroscopy, UV-Vis spectroscopy and XPS

SEM micrographs were collected using a Zeiss Gemini 300 scanning electron microscope in HV mode. XRD data were collected using a Panalytical Empyrean system (Theta-Theta, 240 mm) equipped with a PIXcel-1D detector, Bragg-Brentano beam optics (including hybrid monochromator), and parallel beam optics. Raman spectra were obtained with a LabRam spectrometer (Jobin Yvon Horiba). The excitation line was provided by an Ar laser (532.19 nm). UV-Vis spectroscopy was measured using a Shimadzu UV 3600 spectrometer. XPS measurements were performed using Axis Supra (Kratos Analytical) using the monochromated Ka X-ray line of an Aluminium anode. The pass energy and step size were 40 eV and 0.15 eV respectively. The samples were electrically grounded to minimize charging effects. Data processing was performed using CasaXPS program.

D.1.5 Materials

The following chemicals were used as received without further purification. $CuCl_2.2H_2O$ was purchased from Acros organics and $(NH_4)_6H_2W_{12}O_{40} \cdot xH_2O$ was obtained from Sigma Aldrich. PEG-300 was obtained from TCI, lot. UP2XKAA, d 1.13.

D.2 Supplementary figures and tables

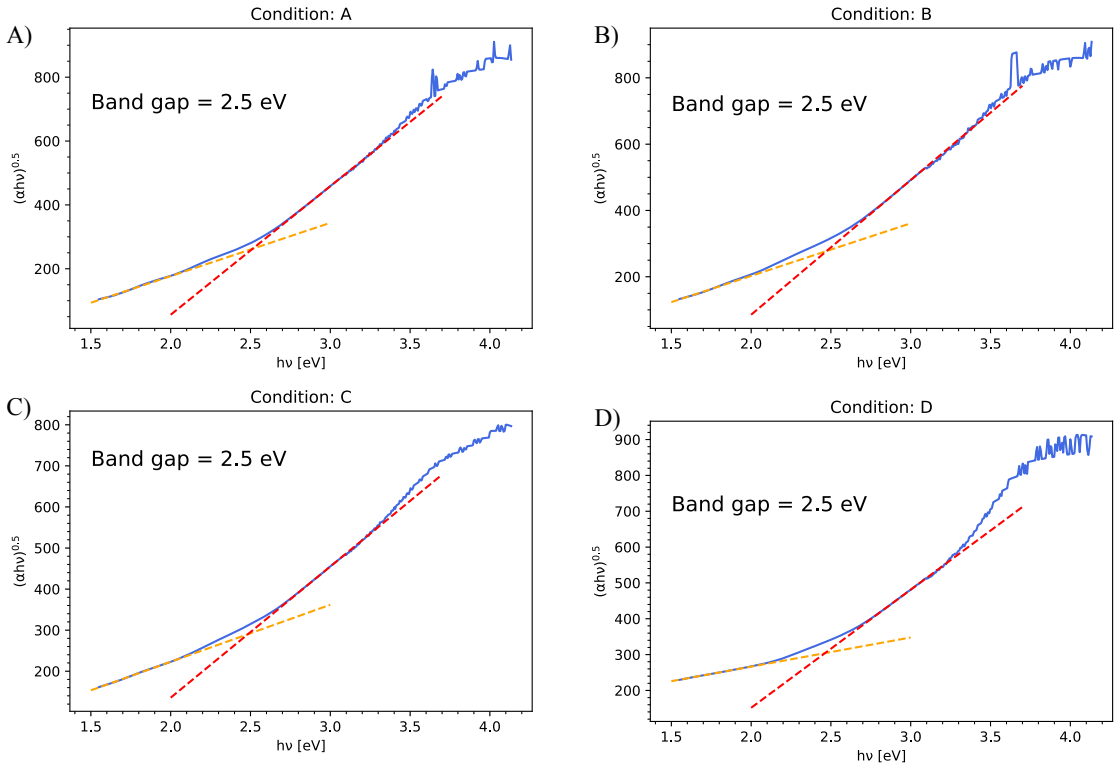

Figure D.1: Tauc plot of the $CuWO_4$ films condition A, B, C and D

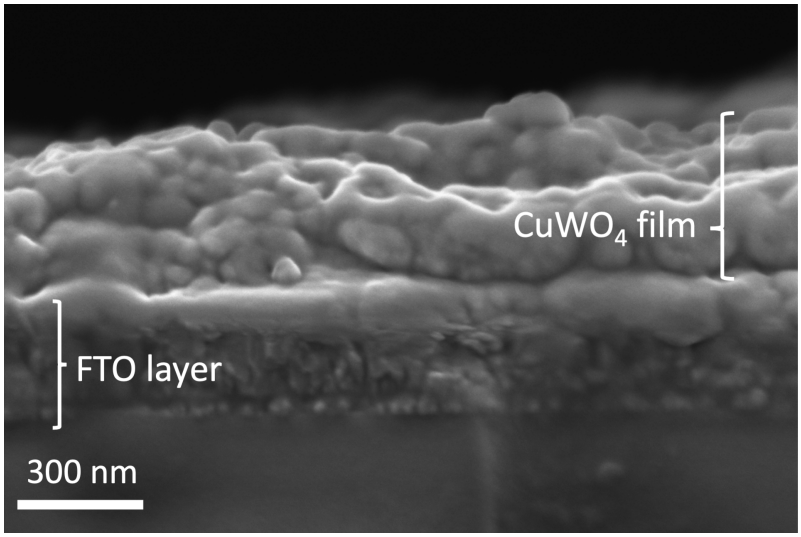

Figure D.2: Cross section SEM micrograph of $CuWO_4$ film condition A. The film thickness is found to be approximately 400 nm.

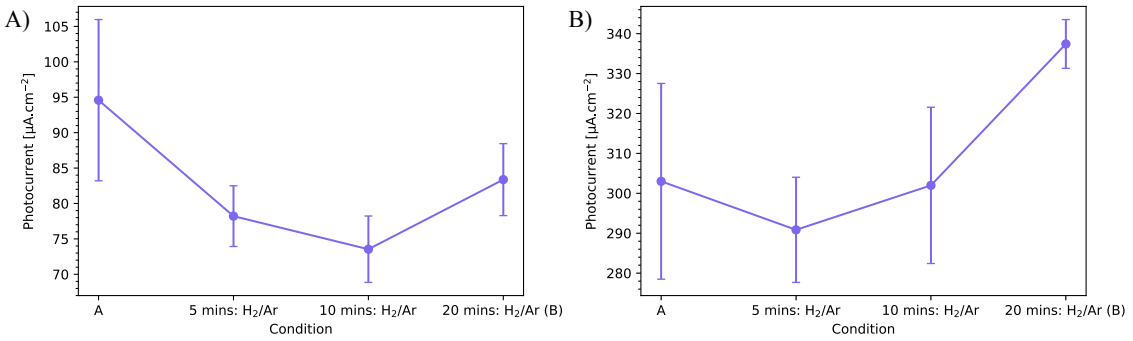

Figure D.3: Average photocurrent at A) 1.23 V vs. RHE and B) 1.75 V vs. RHE of the $CuWO_4$ film condition A and the $CuWO_4$ films which have been subjected to the secondary annealing under 13 % H_2/Ar flow at 300 °C for 5, 10 and 20 minutes (condition B). The average photocurrent was obtained by performing chopped-light illumination LSV.

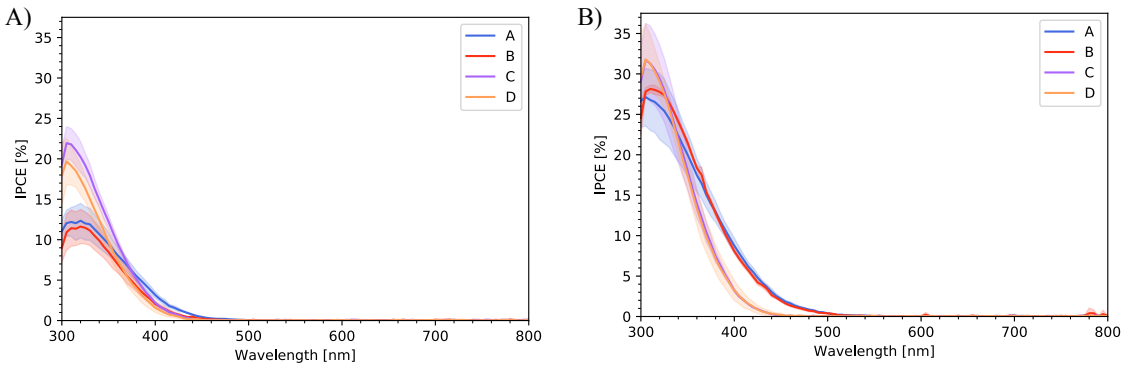

Figure D.4: Average IPCE of the $CuWO_4$ condition A, B, C and D from 300 - 800 nm at A) 1.23 V vs. RHE and B) 1.75 V vs. RHE.

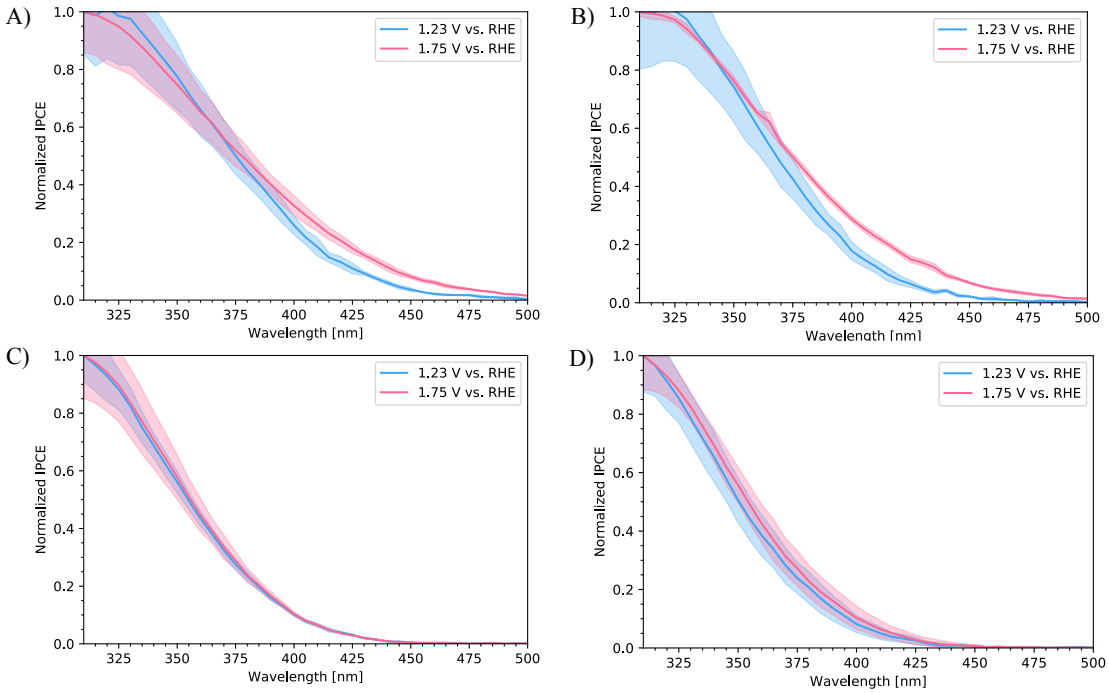

Figure D.5: Normalized average IPCE at 1.23 V vs. RHE and at 1.75 V vs. RHE of the $CuWO_4$ condition A) A, B) B, C) C and D).

Curriculum vitae

Nukorn Plainpan

Nationality: Thai
Email: nukorn.p27@gmail.com

Education

PhD in Chemistry and Chemical Engineering 2018 - Present
École Polytechnique Fédérale de Lausanne (EPFL) Lausanne, Switzerland Expected Graduation: February 2023

MRes Green Chemistry, Energy and the Environment 2016-2017
Imperial College London London, UK
Graduated with Merit

BSc in Chemistry 2012-2016
Chulalongkorn University
Bangkok, Thailand
Graduated with 1st Class honor, GPAX: 3.86

Programing Language Skill

Python

- Enrolled in the course: Python for Data Science by EPFL
- Use in all data analysis during PhD

Award and Scholarship

Royal Thai Government Scholarships 2013-2023

Research Experience

École Polytechnique Fédérale de Lausanne (EPFL): Lausanne, Switzerland 2018 - Present
PhD Student; Advisor: Prof. Kevin Sivula
Development of metal oxide photoanode for biomass valorization in aqueous solution
Key Skills:

- Fabrication and characterization of metal oxide thin film photoanode
- Electrochemistry

Imperial College London: London, UK 2016-2017
Master's project; Advisor: Prof. Patricia Hunt, Dr Andrew Ashley
Mechanism of CO_2 activation by Frustrated Lewis Pairs (FLPs)
Key Skills:

- DFT calculation

Osaka University: Osaka, Japan Summer, 2015
Three-month exchange student; Advisor: Prof. Takashi Hayashi
Synthesis of porphycene
Key Skills:

- Organic synthesis

Chulalongkorn University: Bangkok, Thailand 2015-2016
Bachelor project; Advisor: Dr Pannee Leeladee
Preparation and Characterization of Porphycene-Graphene Oxide Composite for Photocatalytic Application
Key Skills:

- Prepare and characterization of graphene oxide
- Characterization techniques for dye adsorption on graphene oxide

Teaching Experience

Teaching assistant to the master's degree course 2018 - Present

- Chemical Engineering Practical Work
- Chemical Product Design

Supervising master thesis

- Nicolas Fluckiger: MnO_x/WO_3 Photoanode for Hydroxymethylfurfural Oxidation 2020
- Pamela Canjura: Photoelectrochemical Oxidation of Hydroxymethylfurfural on Tungsten Trioxide Photoanodes 2019

Selected Publications

1. **Plainpan, N.** ; Boudoire, F. ; Sivula , K.
   Derivative Voltammetry: a Simple Tool to Probe Reaction Selectivity in Photoelectrochemical Cell
   Sustainable Energy & Fuels, **2022**, 6 (17), 3926-3930

2. Polo, A. ; Dozzi, M.V. ; Grigioni, I. ; Lhermitte, C. ; **Plainpan, N.** ; Moretti, L. ; Cerullo, G. ; Sivula, K. ; Selli, E.
   Multiple Effects Induced by Mo^{6+} Doping in $BiVO_4$ Photoanodes
   Solar RRL, **2022**,6, 2200349

3. Lhermitte, C. R. ; **Plainpan, N.** ; Canjura, P. ; Boudoire, F. ;Sivula, K.
   Direct Photoelectrochemical Oxidation of Hydroxymethylfurfural on Tungsten Trioxide Photoanodes
   RSC Advances*,* **2021**, *11*, 198–202
   co-first authors*

4. Phuangburee, T. ; Dmytro Solonenko, D. ; **Plainpan, N.** ; Thamyongkit, P. ; Zahn, D. RT. ; Unarunotai, S. ; Tuntulani, T. ; Leeladee, P.
   Surface Modification of Graphene Oxide via Noncovalent Functionalization with Porphyrins for Selective Photocatalytic Oxidation of Alcohols.
   New Journal of Chemistry, **2020**, *44, 20,* 8264-8272